Coherent Processes in Rare-Earth-Ion-Doped Solids

Walther, Andreas

2009

Coherent processes in rare-earth-ion-doped solids

Andreas Walther

Department of Physics
Faculty of Engineering
Lund University

Coherent Processes in Rare-Earth-Ion-Doped Solids

Andreas Walther

Doctoral Thesis
2009

Lund University

Coherent Processes in Rare-Earth-Ion-Doped Solids

Printed in Sweden by Media-Tryck, Lund, 2009

Division of Atomic Physics
Department of Physics
Faculty of Engineering, LTH
Lund University
P.O. Box 118
SE–221 00 Lund
Sweden

http://www.atom.fysik.lth.se

ISSN 0281-2762
Lund Reports on Atomic Physics, LRAP-404

ISBN 13: 978-91-628-7718-7

Abstract

This thesis describes a number of coherent processes, such as quantum information processing, superradiance and electromagnetically induced transparency, which have been experimentally implemented using rare-earth-ion-doped crystals.

The rare-earths are a class of elements that have in common, an atomic structure that allows for very long lifetimes as well as coherence times, both on optical transitions and on spin transitions. These ions can be naturally trapped inside host crystals, and with the phonon vibrations removed by cooling down to cryogenic temperatures ($\lesssim$ 4 K), they can be used for a number of different quantum information processes. Most experiments were carried out using Pr^{3+}:Y_2SiO_5 , but also other crystal types were investigated, such as Nd^{3+}:YVO_4, and $La_2(WO_4)_3$. The characterization of the ions were done with a variety of methods, including among others, photon echo techniques and electromagnetically induced transparency.

Quantum computing is a rapidly growing field and there are still many potential candidates for its implementation. In our work we have utilized the spin states of the Pr^{3+} rare-earth ion as a qubit, and demonstrated arbitrary single qubit gates, which are important pieces towards a quantum computing realization in these systems. Most of the experimental work done for the thesis was carried out using an ensemble approach, that has the advantage of giving a strong readout signal, but for future scaling to multiple qubits, single instances are more promising, which is discussed.

Quantum memories are crucial components in applications such as quantum networks and long distance quantum communication. In this thesis, work has been done to investigate how quantum memories can be implemented in rare-earth crystals. In particular, there are two protocols, CRIB and AFC, which were suggested with rare-earth crystals directly in mind, and both of these require high optical depth, αL , for maximum recall efficiency. In this thesis, implications of being in the high αL regime, with phenomena such as superradiance, a collective effect that could cause the stored light to be immediately reemitted, and slow light effects

that come from performing the storage inside spectral structured materials, were investigated.

In order to carry out the phase-sensitive experiments, a laser system with a very narrow linewidth of $\sim$ 1 kHz at 606 nm was constructed, by locking the laser to a semi-persistent spectral hole. In addition, many experiments required advanced pulse shapes, such as complex sechyp pulses or pulses obtained from optimal control theory. In order to be able to accurately create such shapes, an elaborate system using an arbitrary waveform generator and two well calibrated AOMs, controlled from a computer, was also built.

Populärvetenskaplig sammanfattning

Målet avhandlingen har varit att undersöka möjligheten att bygga en kvantdator i kristaller dopade med joner av sällsynta jordartsmetaller. Det har visat sig att sådana joner har en väldigt lång livstid, vilket är en förutsättning för de typer av experiment som har utförts i den här avhandlingen. För att ytterliggare förhindra att de känsliga tillstånden i jonerna störs, så har kristallerna kylts ner till ungefär -271 °C (bara 2 grader över absoluta nollpunkten), med hjälp av en kryostat som använder flytande helium. Innan experimenten kunde påbörjas, var det även nödvändigt att bygga en laser med en väldigt stabil frekvens (färg på ljuset). Man kan säga att, för att kvantdatorexperimenten skulle lyckas var det tvunget att hålla frekensen hos lasern stabil ner till 12:e decimalen, vilket kräver en väldigt hög grad av kontroll på lasersystemet.

En kvantdator är en slags dator som är begränsad endast av de kvantmekaniska spelreglerna, vilket betyder att den löser uppgifter på ett helt annat sätt än en klassisk dator, och därför har potential att bli mycket kraftfullare. Den minsta informationsenheten i en klassisk dator är en bit, vilken kan vara antingen 1 eller 0. En motsvarande *kvantbit* kan också vara 1 eller 0, men med den skillnaden att den kan, med en viss sannolikhet, också vara i båda tillstånden samtidigt! Detta är ett så kallat superpositionstillstånd, och med hjälp av dessa kan man få en kvantdator att lösa vissa typer av uppgifter på flera olika sätt samtidigt. Detta är en av de egenskaper som gör den potentiellt kraftfullare än en vanlig klassisk dator.

Kvantdatorfältet är fortfarande ungt. Ingen har lyckats få mer än några få kvantbitar att samverka, och det finns en mängd olösta frågor angående hur man kan skala upp det till att innehålla så många kvantbitar att den kan börja lösa stora problem. Det är därför fortfarande viktigt att ständigt söka efter nya möjligheter, och nya sätt att bygga kvantbitarna på, så att något sätt i framtiden lyckas bli skalbart. I våra experiment har vi ly-

ckats visa att joner från de sällsynta jordartsmetallerna kan erbjuda sådana intressanta möjligheter. Vi visade detta genom att fullständigt karatärisera en kvantbit i en sådan jon, där enskilda elektrontillstånd används som 1 eller 0. Vi visade även att man med hjälp av noggrant kalibrerade ljuspulser från den stabiliserade lasern, kan utföra grindoperationer på kvantbiten, som t. ex. NOT-grinden, men vi utförde även mer avancerade grindar som endast finns i en kvantdator.

På vägen mot realiserandet av en kvantdator har även ett antal andra koherenta processer, som också bygger på de kvantmekaniska reglerna, stötts på. Dessa innefattar bland annat så kallad *superradians*, vilket är en process där många atomer samverkar kvantmekaniskt på ett sådant sätt att när atomerna skickar ut ljus (deexciteras) så gör de det mycket snabbare än atomerna skulle ha gjort om de hade varit ensamma. Andra intressanta fenomen som påträffades var *långsamt* och *snabbt* ljus. Genom att manipulera atomer med olika frekvens på olika sätt kan man nämligen skapa förhållanden där en ljuspuls som skickas genom materialet går mycket långsammare eller mycket snabbare än den vanliga ljushastigheten. Under tillräckligt extrema förhållanden kan man till och med få toppen på en ljuspuls att komma ut ur materialet innan den ens har kommit in! Detta innebär inte ett brott mot relativitetsteorin eller mot kausaliteten, utan betyder istället att man måste vara noggrann med hur man definierar informationsinnehållet i en puls.

List of Publications

This thesis is based on the following papers, which will be referred to by their roman numerals in the text.

I **Understanding laser stabilization using spectral hole burning**
B. Julsgaard, L. Rippe, A. Walther and S. Kröll.
Optics Express **15**, 11444 (2007).

II **Experimental quantum state tomography of a solid state qubit**
L. Rippe, B. Julsgaard, A. Walther, Yan Ying and S. Kröll.
Phys. Rev. A **77**, 022307 (2008).

III **Spectral hole-burning spectroscopy in Nd^{3+}:YVO_4**
S. R. Hastings-Simon, M. Afzelius, J. Minář, M. U. Staudt, B. Lauritzen, H. de Riedmatten, N. Gisin, A. Amari, A. Walther, S. Köll, E. Cavalli and M. Bettinelli.
Phys. Rev. B **77**, 125111 (2008).

IV **Hyperfine structure and hyperfine coherent properties of Praseodymium in single-crystalline $La_2(WO_4)_3$ by hole-burning and photon-echo techniques**
O. Guillot-Noël, Ph. Goldner, F. Beaudoux, Y. Le Du, J. Lejay, A. Amari, A. Walther, L. Rippe and S. Kröll.
Submitted to Phys. Rev. B, (2009).

V **Long coherence lifetime and electromagnetically induced transparency in a highly spin concentrated solid**
Ph. Goldner, O. Guillot-Noël, F. Beaudoux, Y. Le Du, J. Lejay, T. Chanalière, J.-L. Gouët, A. Amari, A. Walther, L. Rippe and S. Kröll.
Accepted for publication in Phys. Rev. A, (2009).

VI **Experimental superradiance and slow light effects for quantum memories**
A. Walther, A. Amari, S. Kröll and A. Kalachev.
Submitted to Phys. Rev. A , (2009).

Contents

Papers

Chapter 1

Introduction

The primary objective of the work done for this thesis has been to investigate the possibilities of quantum computing in crystals doped with rare-earth ions. On the road towards this objective, several types of coherent processes were encountered and, as the title suggests, this thesis will contain a description of these processes. This is a very broad topic, and naturally I have had to impose some limitations on what to include. In this introduction I will present the sub-topics that are included and how they relate to each other. I will also make an effort here to introduce some of the basic physical concepts in a more popular-science way, in the hope to make the introduction accessible to a broader audience. So in that spirit, let us first take a moment to define what the term *coherent* in the title means.

1.1 Superposition states and Coherence

Typical macroscopic objects (containing many atoms) that we have personal experience of, such as a TV set, or a classical bit in a computer, has an either-or behavior in its states. A TV for example, is either in the state *on*, or it is *off*, and similarly, classical bits can either be in the 1-state or they are in the 0-state. However, quantum objects (in general containing only a few atoms) can be in several states at the same time. A quantum mechanical TV, if it existed, could be in both state *on* and state *off* at the same time, and similarly, quantum mechanical bits, *qubits*, can be in both state $|1\rangle$ and state $|0\rangle$ at the same time, with some respective probabilities. This type of situation, in which a particle is in two states at the same time, is called a superposition. Even for a particle with only two possible states, there is an infinite number of different combinations to form a superposition. There could, for example, be a 50% chance of finding an atom in each of two

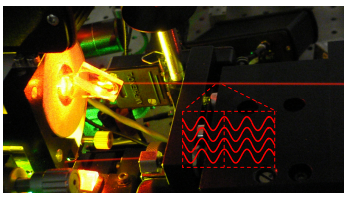

Figure 1.1. *A picture of a part of the dye laser used in the experiments in Lund. The dashed box illustrates a magnified part of the beam were the coherence of the aligned phases of the light is schematically drawn.*

states, but another situation would be that there is a 90% chance of finding it in the first state and only 10% chance to find it in the second state, and so on.

As an additional complexity, each probability comes with an associated sign. The 10% chance mentioned above, might, for example, be said to be either +10% or -10%. This bears no significance at all when looking only at the single particle, the chance to detect it in the second state is still the same 10%. This sign however, called the phase of the superposition, is of great importance when the particle is interacting with another particle that is also in a superposition. Depending on the relative signs, the states can then either cancel each other out, or add together constructively, and this can then be used to perform what is called quantum computation. This behavior, while it seems very strange when looking at it with our classical eyes, has been demonstrated and verified in countless experiments during the past hundred years. There are several reasons why everyday things do not display this phase, and one of them is averaging. A macroscopic object consists of millions of billions of atoms, each with possibly different superposition states, and our senses will detect only the average value of all of these when interacting with it.

Another important reason is the scales on which we live. On the time scale for example, the human resolution is in the order of a hundredth of a second, whereas many atomic states survive for less than a millionth of a second, and often, even less than that. And on a temperature scale, room temperature is around 20°C, also known as 293 K, which is very far from the absolute zero point where the atoms are in their most stable condition. Heat may basically be regarded as motion of atoms, whether it is in the form of rotations or vibrations or something else. This movement has a tendency to affect the phase in a randomizing way, for example during collisions of two atoms in a gas, and will also have the effect that the phase becomes lost to us.

Nevertheless, there are macroscopic effects we can see, that can be explained only by using quantum mechanics. Such an example is superconductivity, but perhaps the best-known example is the laser. Comparing the light from a normal source, such as a light bulb, to that of a laser, one notices how "well organized" the light from the laser is. Contrary to a light bulb, all of the light from the laser travels in the same direction, has the same wavelength (color), and, if looked at with the proper tools, it has all of its waves traveling in phase with each other. This behavior is illustrated in Figure 1.1 and is also the definition of *coherent* that we were looking for. When single or multiple quantum systems, such as photons in the case of the laser, or the atomic states as we discussed before, all exist with well-defined values of their phase, we say that they are coherent, and this property is a common denominator to the different experiments that were done as a base for this thesis.

1.2 The power of quantum computing

With the additional complexity of quantum systems also comes (possibly) greater power. In 1982 Richard Feynman [1] showed that a computer that had access to the full power of the quantum world could efficiently simulate certain quantum systems, that classical computers could not do. Further, in 1994 Peter Shor found an algorithm, designed to run on a quantum computer, that performed prime number factorization in exponentially fewer steps than any known classical algorithm [2]. Shortly thereafter, Lov K. Grover found another quantum algorithm that would offer a quadratic improvement over the best known classical algorithm when searching an unstructured data base [3]. Even though a quadratic improvement is nowhere near as powerful as an exponential one, this search routine can be very useful as the following example will show.

Example

Imagine that you have a phone book with 10 000 persons listed, sorted according name in the usual way. If someone then gives you a phone number and asks you to find the person who has that number, there would be no easy way of performing that task. With the phone book being completely unstructured when searching by numbers, you would have no choice but to check all persons, one by one, until you found the one with the correct number. On average, you would have to search through half of the listed persons before finding the one you were looking for. A classical computer, although making each check faster, would not have a better method than you, and would thus also have to go through 5 000 checks on average. Now imagine that you had the possibility to use a quantum computer with Grover's search algorithm, which performs the task with a quadratic speed-up. Instead of searching half the list, you could now successfully complete the task using only $\sqrt{10000} = 100$ checks on average. Even though this is not the most powerful algorithm, and even though this example only uses a small database, we already see an improvement by a factor of 50. When we then add to this, that the improvement gained from using quantum algorithms becomes larger the larger the problem is, it is easy to imagine the potential that a quantum computer could bring.

Although it has not yet been rigorously proven that quantum computing really offers a fundamental speed-up, the potential of the computational power demonstrated by this example and the other methods, has intrigued and motivated many scientists to investigate it further.

1.3 Comments on the outline of the thesis

Before the actual experiments could be initiated, a laser operating at the right wavelength and fulfilling the rigorous requirements on frequency stability had to be built. Although this construction took a long time, nearly half the time taken for the work for this thesis, the work itself was scientifically interesting, and led to a comprehensive investigation of the coherent processes involved when locking to spectral holes, presented in Paper **I**. In addition to the laser itself, there were also several other technical solutions that have had a key role in the experiments, and the most important of these are discussed in Chapter 4. Following the completion of the laser, one of the milestones for the thesis work could be carried out in the form of the realization of a single full qubit, verified by quantum state tomography as described in Paper **II**. The main goal of this thesis has been the work towards quantum computing in rare-earth solids, and the results and conclusions obtained regarding this goal are discussed in Chapter 5. To give a background to the experimental quantum information, in Chapter 2, the basic theory of coherent light matter interaction is outlined.

In the course of the work, there has also been a strong aspect of international collaboration. In the ever ongoing search for better quantum computing materials, the suitability of Zeeman levels for quantum information investigated in Paper **III**, was done together with a group from Geneva. Similarly, together with a group from Paris, a material of high magnetic moment density was characterized in Paper **IV**, and its viability for further coherent experiments was demonstrated in Paper **V**, by the observation of electromagnetically induced transparency. This phenomenon, and others that are also derived from manipulating the dispersion profile, are described in Chapter 7. Other considerations regarding material properties, and a description of rare-earth-ion-doped crystals in general, are given in Chapter 3. Finally, together with expertise from Kazan in Russia, the impact of high optical depth for quantum memories was reported in Paper **VI**. Quantum memories are discussed further in Chapter 6, and an important mechanism in materials of high optical depth, superradiance, is explained in some detail in Chapter 8.

Chapter 2

Light-matter interaction

In this chapter I will introduce the basic ideas and equations for dealing with coherent light-matter interaction. I will start with Maxwell's equations describing the interaction focused on the electric field, followed by the Bloch equations describing it with the atomic state in focus, and finally combine these pictures in the Maxwell-Bloch equations. As we shall see, the Bloch picture is also very useful for visualizing the state of a two-level system. There will also be an introduction to the general ways of describing quantum states and entanglement.

2.1 Maxwell's equations

The starting point for the description of light as an electromagnetic wave is the set of equations known as Maxwell's equations. They were put together in 1884 by Oliver Heaviside, after Maxwell's addition of the *displacement current* term, $\partial\mathbf{D}/\partial t$, in 1861. The four equations are [4]:

$$\nabla \cdot \mathbf{D} = \rho_f, \tag{2.1}$$

$$\nabla \cdot \mathbf{B} = 0, \tag{2.2}$$

$$\nabla \times \mathbf{E} = -\frac{\partial \mathbf{B}}{\partial t}, \tag{2.3}$$

$$\nabla \times \mathbf{H} = \mathbf{J_f} + \frac{\partial \mathbf{D}}{\partial t}. \tag{2.4}$$

Here, J_f is the free current density and D is called the *electric displacement field*. This field is a way of expressing how matter with susceptibility χ reacts to an electric field according to $D = \epsilon_0 E + P$, where $P = \epsilon_0 \chi E$ is the induced polarization in the material. This can be intuitively understood by regarding the atom as a positive nucleus surrounded by a negatively charged electron cloud. In the

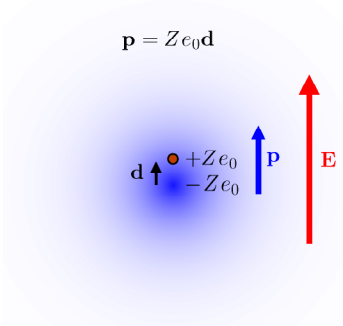

Figure 2.1. *The positive nucleus and the center of the negative electron cloud are separated by an external electric field, E. This polarization of charges is known as the electric dipole moment, p.*

presence of the electric field from the light, charges will be separated and thus the equilibrium positions of the nucleus and the electrons will be displaced relative to each other. This charge separation is the material polarization, and will give rise to a dipole moment $p = qd$, where q is the value of the charges and d the distance between them. This mechanism is illustrated in Figure 2.1.

The crystals that we are using will be discussed in more detail in Chapter 3 but in general we can assume that their conductivity is low, and that they are not magnetized. We can then combine Maxwell's equations (see e.g. [4]), to get the electromagnetic wave equation:

$$-\nabla^2\mathbf{E} + \frac{1}{c^2}\frac{\partial^2\mathbf{E}}{\partial t^2} = -\mu\frac{\partial^2\mathbf{P}}{\partial t^2}, \tag{2.5}$$

where $\mathbf{E}$ is the total electric field including the light frequency, i.e.

$$\mathbf{E}(z,t) = \frac{1}{2}\mathcal{E}(z,t)e^{i(kz-\omega t)}\mathbf{e_x} + \text{complex conj.}, \tag{2.6}$$

if the light propagates in the z-direction, and is polarized in the x-direction. $\mathcal{E}$ is the complex amplitude of the envelope of a pulse, and k is the wave number, $k = \omega/c$. In the wave equation, c is the speed of light in the material and can be expressed in terms of the permittivity, ϵ, and permeability, μ, according to $c = 1/\sqrt{\mu\epsilon}$.

2.1.1 Slowly varying envelope approximation (SVEA)

In most cases, the envelope of a light pulse varies much more slowly than the field itself. For example, with a wavelength of 606 nm, the frequency of the electromagnetic oscillation is 495 THz, while the envelope changes in our schemes occur typically at MHz frequencies, i.e. ~ 8 orders of magnitude slower. In this regime the wave equation, Equation (2.5), can be written

$$\frac{\partial\mathcal{E}}{\partial z} + \frac{1}{c}\frac{\partial\mathcal{E}}{\partial t} = i\frac{\omega}{2\epsilon c}\mathcal{P}, \tag{2.7}$$

where the second order derivatives have been assumed to be very small due to the slow changes, and where the fields only come in as the pulse envelopes, $\mathcal{E}$ and $\mathcal{P}$.

2.2 Bloch sphere

So far we have only looked at the interaction from the point of view of the light, how it changes when it passes through a medium. A clear and intuitive picture of what happens to the atoms, can be gained from the Bloch equations. Let us for simplicity first assume that we are working only with two-level systems. This is not a

serious restriction as the equations can be extended to include more levels when needed, as is done for instance in Paper I.

An arbitrary superposition state of a system with two levels, a ground state $|g\rangle$ and an excited state $|e\rangle$, can be written in Dirac notation as

$$|\psi\rangle = \alpha\,|g\rangle + e^{i\omega t}\beta\,|e\rangle\,, \tag{2.8}$$

where α and β are the complex probability amplitudes for finding the system in each level. Here, the phase factor that follows the electron cloud oscillations is explicitly stated, with ω as the angular frequency corresponding to the energy difference between the two levels, $\omega = E_{ge}/\hbar$. If we for simplicity assume that we are in a reference frame following this optical rotation, we can write the arbitrary state as stationary, $|\psi\rangle = \alpha\,|0\rangle + \beta\,|1\rangle$. Also, since the system must exist somewhere, there is a conservation of population, which can be expressed as $|\alpha|^2 + |\beta|^2 = 1$.

In order to visualize this two-level state, we can rewrite the expression slightly, replacing the probability amplitudes, α and β, by two mathematical parameters, θ and ϕ:

$$|\psi\rangle = \cos\frac{\theta}{2}\,|g\rangle + e^{i\phi}\sin\frac{\theta}{2}\,|e\rangle\,. \tag{2.9}$$

This expression is equivalent to Equation (2.8), and it can be noted, for example, that the conservation requirement is still fulfilled, since $\cos^2\frac{\theta}{2} + \sin^2\frac{\theta}{2} = 1$. The advantage of this is that the two parameters, θ and ϕ, can be visualized in a very useful way as the angles of an arbitrary vector on the unit sphere. This is known as the Bloch sphere representation and is demonstrated in Figure 2.2. Even though the equations in this chapter can be extended to more levels, there is no known extension of the sphere picture to include more than two levels.

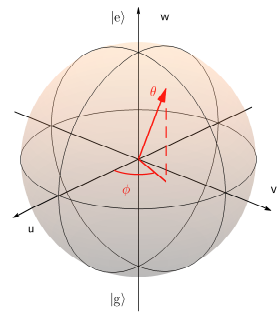

Figure 2.2. *The Bloch sphere with a vector inscribed that demonstrates the two characterizing angles, θ, and ϕ.*

2.2.1 Density matrices

For calculations, it is usually convenient to express the equations using density matrix formalism, so I will give a brief introduction to that here. For a very good and extensive walk through of this formalism, see Nielsen and Chuang [5]. First, let us describe the two states, $|g\rangle$ and $|e\rangle$, with corresponding vectors that span a 2×2 qubit space:

$$|e\rangle = |0\rangle = \begin{bmatrix} 1 \\ 0 \end{bmatrix};\ |g\rangle = |1\rangle = \begin{bmatrix} 0 \\ 1 \end{bmatrix}. \tag{2.10}$$

Note here in particular, that $|0\rangle$ is chosen to be the excited state and $|1\rangle$ the ground state, despite what one might intuitively expect. This choice is made so that for matrix operators, the first column will act on $|0\rangle$ and the second will act on $|1\rangle$, which is the normal

convention in linear algebra. The definition of the density matrix, ρ, is what is called the outer product of the wave function

$$\rho = |\psi\rangle \langle\psi| , \tag{2.11}$$

where $|\psi\rangle = \langle\psi|^\dagger$ is the Hermitian conjugate, which is the combined operation of a complex conjugate and a transpose. With the definition of the base vectors above, the density matrix of an arbitrary state in this reference frame now becomes

$$\rho = \begin{bmatrix} \alpha \\ \beta \end{bmatrix} \begin{bmatrix} \alpha^* & \beta^* \end{bmatrix} = \begin{bmatrix} |\alpha|^2 & \alpha\beta^* \\ \beta\alpha^* & |\beta|^2 \end{bmatrix} = \begin{bmatrix} \rho_{11} & \rho_{12} \\ \rho_{21} & \rho_{22} \end{bmatrix}. \tag{2.12}$$

In this 2×2 matrix the diagonal elements represent the population distribution between the two states and the off-diagonal elements represent the coherent phase if the state is in a superposition. We can now define three new variables which have a very clear connection to the Bloch sphere introduced in the previous section.

$$\begin{cases} u = \rho_{12} + \rho_{21}^*, \\ v = i(\rho_{12} - \rho_{21}^*) \\ w = \rho_{11} - \rho_{22}. \end{cases} \tag{2.13}$$

The interpretation of these variables is that w measures the degree of excitation of an atom, with $w = 1$ being in the excited state, $|0\rangle$, and $w = -1$ being in the ground state, $|1\rangle$, while the quantity

$$u - iv = 2\rho_{12}, \tag{2.14}$$

describes the phase of the state, and the u- and v-axis span the equator plane in the Bloch sphere, as seen in Figure 2.2.

2.2.2 Bloch Equations

Taking the time derivatives of variables (u, v, w) in Equation (2.13) above, and using the equation of motion for the atomic system in a field (see [4]), we get

$$\begin{cases} \dot{u} = -\frac{u}{T_2} - \delta v + \Omega_{\mathrm{Im}} w, \\ \dot{v} = \delta u - \frac{v}{T_2} + \Omega_{\mathrm{Re}} w \\ \dot{w} = -\Omega_{\mathrm{Im}} u - \Omega_{\mathrm{Re}} v - \frac{w+1}{T_1}, \end{cases} \tag{2.15}$$

where it has been assumed that the ground state, $w = -1$, is the equilibrium state, to which the system will decay at a rate of $\Gamma_1 = 1/T_1$. The difference between the light frequency and the atomic resonance frequency is called detuning and is denoted by δ, while T_2 is the phase decay time. The two different decay mechanisms with time scales of T_1 and T_2, warrants further discussion and will be explained in more detail in Section 2.3. The coupling between the field and the atom is expressed by the Rabi frequency

$$\Omega(t) = \frac{\mu_{eg}\mathcal{E}(t)}{\hbar}, \tag{2.16}$$

where μ_{eg} is the dipole moment for the transition, and $\mathcal{E}$ is the complex electric field amplitude, as before. The Rabi frequency has the property that it expresses the angular velocity of a state in the Bloch sphere, and is determined by the amplitude of the light. Thus, for a pulse with a duration of t, the total angle, or pulse area, Θ, by which a state is changed due to the effects of the light, is given by

$$\Theta = \int_0^t \Omega_{Re}(t')dt'. \tag{2.17}$$

If the pulse is a square pulse, then the expression is simply reduced to $\Theta = \Omega_{Re} \cdot t$.

2.2.3 Maxwell-Bloch equations

In the Maxwell wave equation (Equation (2.7)) the atoms were described by the polarization, $\mathcal{P}$. We have seen that the Bloch vector, (u, v, w), is very convenient for describing the atoms, and so it makes sense to rewrite the wave equation (see e.g. [6, 7]), with the polarization picture replaced by the Bloch picture:

$$\frac{\partial \Omega_0}{\partial z} + \frac{n}{c}\frac{\partial \Omega_0}{\partial t} = \frac{i\alpha_0}{2\pi}\int_{-\infty}^{\infty} g(\delta)(u - iv)d\delta. \tag{2.18}$$

The electric fields have now been replaced by the complex Rabi frequency, and $g(\delta)$ is a function describing the distribution of atoms as a function of detuning, δ. This equation, together with Equations (2.15) form the Maxwell-Bloch equations which is the starting point for calculations in some of the chapters or Papers included in this thesis.

2.3 Decay mechanisms

In the Bloch equations above we noticed two different decay terms, either proportional to $1/T_1$ or to $1/T_2$. The difference between these two will be explained in this section, with examples taken from the ion-doped crystals that we have used, which will be further detailed in the next chapter.

2.3.1 Lifetime, T_1

T_1 is the lifetime of the excited state, i.e. how long it takes on average before an atom in an excited state has decayed to a lower lying state. The fact that it decays at all is not at all obvious, and although this is usually discussed in basic courses in atomic physics I will dwell on it briefly for the sake of completeness of the overall discussion.

When an electric field, in the form of a photon with an energy corresponding to the difference between two levels in an atom,

appears near the atom, the field couples the two levels by means of induced dipole moments, as was described before. This coupling gives rise to a probability for the atom to make a transition to the other state. If the final state has a higher energy than the initial state, the excitation energy is taken from the photon, which is absorbed in the process. On the other hand, if the final state has lower energy, the excess energy difference is released in the form of another photon. It turns out that this new photon has exactly the same properties as the first in terms of frequency, phase and spatial mode. This is the process that is known as stimulated emission and is the foundation of lasers for example.

However, even in the absence of such a starting field, the atom still has a chance of decaying to the lower state. This is caused by vacuum fluctuations, which essentially are randomly, out-of-nothing-created photons that will disappear again after a short time inversely proportional to their energy and which is given by Heisenberg's uncertainty relation, $\Delta t \gtrsim \hbar/\Delta E$. These spontaneously created photons have the roll of catalyst field, and again a coupling is created that can allow a transition. The probability for this transition to happen is governed by the overlap of the matrix elements for the two states coupled by the field, which is described by its Hamiltonian, H, $\langle g| H |e\rangle$. In a more intuitive formulation, the transition probability is determined by "how similar" the two states are geometrically, with respect to the charge distribution.

2.3.2 Coherence time, T_2

The lifetime decay describes an energy loss mechanism for the atom, but there are perturbations that change the state position on the Bloch sphere, without constituting an energy loss. These mechanisms are known as decoherence, or phase noise. The time that the state keeps its phase, the coherence time, is usually denoted as T_2.

The following is intended to give a more intuitive understanding of decoherence: imagine that you have a quantum state in a superposition. It will then oscillate with the frequency of the separation of the two levels involved (motivated in Section 8.1). The exact energy of the levels will be dependent on the fields in the surroundings, including those coming from other electrons, the nucleus or other atoms close by. For example, if the spin of a nearby atom gets a random flip, the surrounding field will change slightly, causing an energy shift of the levels, and thus a shift of the oscillating frequency. This shift in frequency is unknown to us, and thus if in a measurement we were trying to establish the phase of the system, by comparing it to a reference such as a laser, we would no longer have perfect agreement. There is a discrepancy in the rotation frequency between the atom and our reference, and we cannot determine the correct phase. This is the process known as deco-

herence, and is thus intimately related to our knowledge of what happens to the atom, because any process that can be predicted and compensated for, will not contribute to the decoherence.

It is obvious that the phase of the superposition will ultimately be limited by the lifetime, because when the system relaxes to the ground state, the phase is lost. This is expressed by $T_2 \leq 2T_1$, with equality if there are no other sources for decoherence than the lifetime decay.

When an atom decays to the ground state and sends out a photon, the phase of that photon will depend on the phase of the atomic charge distribution. In the case of a strongly dephasing environment, the phase of the light will also change significantly, and we can understand that the homogeneous spectral width of the light, Γ_h, is given by the coherence time of the atom, T_2, rather than the lifetime, according to

$$\Gamma_h = \frac{1}{\pi T_2}. \tag{2.19}$$

2.4 Entanglement

One of the most important differences in the quantum world compared to the classical one, is the ability for two states to be entangled. Entanglement is best described as a form of non-classical correlation between two objects, that can be potentially far away from each other, and can be looked upon as a new physical *resource*, just like charge or mass. This section will serve as a brief introduction to entangled states.

2.4.1 Two-qubit states

As mentioned before, an arbitrary single qubit state can be expressed as $|\Psi\rangle = \alpha\,|g\rangle + \beta\,|e\rangle$. If we consider two qubits, they can have a number of different states, and it is interesting to consider a state in particular looking like:

$$|\Psi\rangle = \frac{|eg\rangle + |ge\rangle}{\sqrt{2}}. \tag{2.20}$$

Just like the single qubit state, this state is in a superposition; either the first qubit is excited and the second is in the ground state or the second qubit is excited and the first is in the ground state. Making a measurement on the two qubit system will tell what it is for any particular case, but every time it is random and each case has the probability $|1/\sqrt{2}|^2 = 1/2$, very similar to the single qubit case.

It becomes interesting however, when we ask the question: What are the individual states of each qubit? Since we already

know how to express an arbitrary single qubit, we may try to express two qubits as

$$\begin{aligned} |\Psi_{12}\rangle &= (\alpha_1 |g\rangle + \beta_1 |e\rangle)(\alpha_2 |g\rangle + \beta_2 |e\rangle) \\ &= \alpha_1\alpha_2 |gg\rangle + \alpha_1\beta_2 |ge\rangle + \beta_1\alpha_2 |eg\rangle + \beta_1\beta_2 |ee\rangle \end{aligned} \tag{2.21}$$

Comparing this state with the desired state given in Equation (2.20), we can try to identify the values of the four coefficients that would produce such a state. The desired state contains neither $|gg\rangle$ nor $|ee\rangle$ terms, so at least one of the α's as well as at least one of the β's must be zero. But, on the other hand, the desired state does contain the two mixed terms, $|eg\rangle$ and $|ge\rangle$, and from that we gather that none of the coefficients can be zero. This contradiction means that we cannot express the state as a product of any two single qubit states. The interpretation is that it is simply not possible to speak of such a state as Equation (2.20), in terms of the individual qubit states. Or, expressed in other words, the full information of this state can only be obtained from looking at the combined, two qubit system, and not from any of its parts separately, i.e. the sum is here indeed greater than its parts.

2.4.2 Implications

It is also interesting to consider the implications of these multiple object correlations. Let us say that we create the state in Equation (2.20), but we now send the two qubits far away, say 1 km away, a very macroscopic distance. If the transportation is free from decoherence, then the state is still entangled, and it is still undecided (until the moment of measuring) which qubit is in which state. If a person now measures the state of qubit 1 to be in the ground state, then it is instantly decided that the second qubit, 1 km away, is in the excited state, and any measurements thereafter will agree with this. Einstein did not like this notion that the decision on the second qubit state seemed to have traveled faster than the speed of light, and called it "Spooky action at a distance". He, together with Podolsky and Rosen, wrote in 1935 the famous EPR-paper [8], in which they asked the question whether quantum mechanics could really be considered a complete description of nature, if it behaved like this.

I will not go into a full discussion of this, but the problem can essentially be resolved by removing *local realism* from the set of assumptions that we require from physical systems. One interpretation of this is that we should accept that an entangled state is not two objects that have a distant correlation, but rather that it is *one* system that manifest itself in two spatial points, i.e. it is non-local.

2.5 Interaction with specific pulse types

There are many ways to shape the light pulses that interact with the atoms, and as we will see in this section, some shapes have very useful properties for our purposes.

2.5.1 Square pulses

The simplest pulse we can think of is the square pulse. One that has a constant amplitude for a given duration, τ, and is zero everywhere else. When interacting with atoms in a certain frequency range however, this pulse type is not very efficient. This can be seen by looking at the Fourier transform of the pulse, which is shown in Figure 2.3. The sharp edges of the square pulse gives rise to high frequency terms, and a significant part of the energy in the pulse will either miss the atoms entirely, or have undesired effects on the atoms outside the interesting region. The meaning of spectral atomic regions and how to create them is explained in Chapter 3.

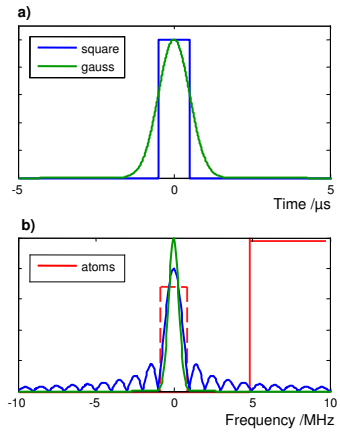

Figure 2.3. *a) shows the time domain pulse shape of a square pulse (blue line) and a gaussian pulse (green line). In b) the Fourier transform of the signals in a) is shown, together with a spectral atomic feature (red lines)*

2.5.2 Gaussian pulses

A slightly more sophisticated approach is Gaussian-shaped pulses. Since the Fourier transform of a Gaussian is another Gaussian, we can put the pulse energy to much better use. However, the energy distribution is still not perfect, because atoms at the center of the pulse will be subject to a higher Rabi frequency than atoms at the edge (see Figure 2.3**b**), and so the light will affect different atoms differently. Furthermore, if an inhomogeneous distribution of atoms are excited then they will dephase during the excitation duration, since a gaussian pulse does nothing to prevent this.

2.5.3 Sechyp pulses

When dealing with inhomogeneously broadened atomic ensembles, it is very convenient to employ more complicated pulses than the ones previously mentioned. It was discovered originally in the NMR field [9, 10] that complex hyperbolic secant pulses, or *sechyp* for short, can be used to compensate completely for the inhomogeneities, and this has been adapted to the optical regime [11]. The sechyp pulse shape is defined as

$$\Omega(t) = \Omega_0 \mathrm{sech}(\beta t)^{1+i\mu}, \tag{2.22}$$

where β and μ are real parameters and Ω_0 is the Rabi frequency at the center. The real part of Equation (2.22) gives the envelope of the pulse

$$\Omega_{real}(t) = \Omega_0 \mathrm{sech}(\beta t). \tag{2.23}$$

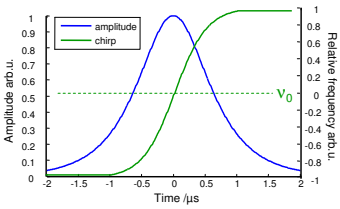

Figure 2.4. *The blue line shows the hyperbolic secant (sechyp) function which is the amplitude envelope of the complex sechyp function. The green line is the chirp of the pulse, given by the hyperbolic tangent function.*

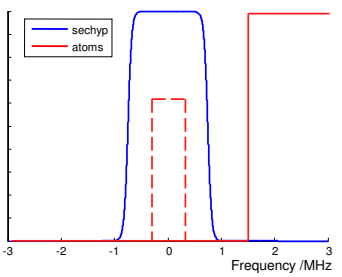

Figure 2.5. *The blue line is the transfer efficiency of a sechyp pulse as a function of detuning. The red lines indicate the spectral distribution of the atoms. The dashed red line is the ensemble of interest and the solid line is atoms further away that we wish to avoid.*

The time derivative of the complex angle of Equation (2.22) gives the instantaneous angular frequency of the light:

$$\frac{\partial\phi(t)}{\partial t} = \mu\beta\tanh(\beta t), \tag{2.24}$$

where the convention that the phase of $e^{-i\phi(t)}$ is $\phi(t)$ has been used. The amplitude envelope and frequency chirp is shown in Figure 2.4.

The somewhat abstract parameters μ and β can be directly related to the more tangible duration (with respect to intensity) and frequency width (Hz) of the pulse according to

$$\begin{aligned} t_{FWHM} &= \tfrac{2}{\beta}\mathrm{arcsech}\sqrt{\tfrac{1}{2}} \approx \tfrac{1.76}{\beta} \\ \nu_{width} &= \tfrac{\mu\beta}{\pi}. \end{aligned} \quad . \tag{2.25}$$

These sechyp pulses can transfer an ensemble of atoms between two states without any inhomogeneous dephasing. This gives a very high transfer efficiency, which is illustrated in Figure 2.5. As can be seen, the pulse is very flat around the ensemble, ensuring that all atoms experience the same Rabi frequency, and then have a very low transfer efficiency outside the range of the chirp width so that unwanted excitations are kept to a minimum. In addition, it turns out that these pulses are also robust against fluctuations in Rabi frequency, which is experimentally very convenient.

2.6 Readout technique

In most of the experiments described in this thesis, a special coherent absorption technique has been used for reading out the spectral structure of the atoms, and the idea behind this technique will be discussed in this section.

The basic idea of the technique is to scan the laser in frequency across the spectral structure and detect the transmission after the sample. For slow scan rates, i.e. slow compared to the coherence time of the atoms, the result of the scan will be very straight forward, giving the transmission profile of the structure. However, for fast scan rates, in addition to the transmission, the detected light after the sample will also contain coherent radiation from the atoms previously excited during the scan. This total signal is more complicated and it requires some post-processing to deduce the real spectral structure. An example of the total detected signal is shown in Figure 2.6. The following will not be a mathematically stringent proof of the technique, but rather an attempt to justify the main steps of the idea. For a more complete description, see Ref. [12].

Readout technique

The light-matter interaction here can be described by Equation (2.7), the wave equation. We can neglect the term $\frac{1}{c}\frac{\partial E_0}{\partial t}$ as it will be small, and furthermore, if we assume a thin crystal, we can remove the z dependence from the polarization and write the electric field coming out of the material as

$$E_{out}(t) = E_{in}(t) + \frac{i\pi\nu_0}{\epsilon_0 c} P(t) \cdot dz. \tag{2.26}$$

The polarization, $P(t)$, depends on the incoming field at an earlier time, through the complex susceptibility, χ, as explained in Section 2.1, where the imaginary part of χ is the absorption coefficient that we are interested in, $\alpha = \mathrm{Im}(\chi)$. In the time domain, the polarization can be written $P(t) = \epsilon_0 \int_0^\infty \chi(\tau) E(t-\tau) d\tau$, where $\chi(\tau)$ is the time-domain Fourier components of the susceptibility. We can now rewrite Equation (2.26) as

$$E_{out}(t) = E_{in}(t) + i\pi dz k_0 \int_0^\infty \chi(\tau) E_{in}(t-\tau) d\tau, \tag{2.27}$$

where we can see that the outgoing field depends only on the incoming field and on the shape of the material, $\chi(\tau)$. In addition, we can recognize that the integral in Equation (2.27) is a convolution, $(\chi * E_{in})(t)$. The best way to deal with convolutions is by a Fourier transform, $\mathcal{F}$, since it turns into a product in the frequency plane, $\mathcal{F}(\chi * E_{in})(t) = \chi(\nu) \cdot E_{in}^{\mathcal{F}}(\nu)$. The Fourier transform of the input field, $E_{in}^{\mathcal{F}}(\nu)$, is fully known, and can be compensated for by division. The idea to retrieve the spectral shape from our signal can be formulated

$$\alpha(\nu) = \mathcal{F}^{-1}\left(\frac{\mathcal{F}(E_{out}(t))}{E_{in}^{\mathcal{F}}(\nu)}\right)\Bigg|_{\kappa t=\nu} = \mathcal{F}^{-1}\left(\frac{\chi_{\mathrm{Im}}(\nu) \cdot E_{in}^{\mathcal{F}}(\nu)}{E_{in}^{\mathcal{F}}(\nu)}\right)\Bigg|_{\kappa t=\nu}, \tag{2.28}$$

where κ is the chirp rate of the input field.

Now, the description above uses E-fields, but the actual detected signal is of course the intensity, and we need to square the expression in Equation (2.27) to get a correct treatment. The result of this would be more complicated expressions, but the intuitive point that we can use the Fourier plane to compensate for the chirp of the incoming field will still be true, and so I will leave it at that.

To recapitulate, a chirped pulse is sent through the material and the total signal of scan + coherent transmission from the atoms is detected. This signal is Fourier transformed, divided by the known input field, transformed back, and rescaled through $\kappa t = \nu$, with the result of $\alpha(\nu)$ being obtained. An example of such a deconvoluted waveform is shown in Figure 2.7.

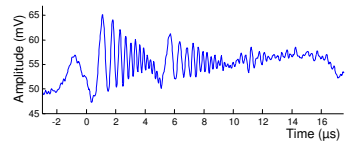

Figure 2.6. *A linearly chirped pulse sent through the material as it is detected. The beatings come from the interference between the pulse and the coherent radiation from the atoms (Free induction decay).*

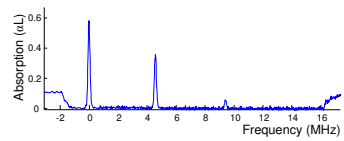

Figure 2.7. *The signal from Figure 2.6 after it has gone through the deconvolution procedure. For details of this procedure, see the text. The three absorption peaks correspond to the three transitions in* Pr^{3+} *which is discussed further in Chapter 3.*

Chapter 3

Rare-earth-ion-doped crystals

The material used throughout the experiments related to this thesis is rare-earth-ion-doped crystals (REICs). The aim of this chapter is to discuss some features of these crystals that will be important in the following chapters. In general, there is a whole range of rare-earth elements that could be valid as qubits, for example erbium (Er), europium (Eu) and thulium (Tm), but in this thesis the focus has been on working with praseodymium (Pr). The useful rare-earth elements all belong to the Lanthanides, which range from element 57 up to 71 in the periodic system. In Figure 3.2 all the relevant rare-earth ions are listed with their energy level diagrams.

These rare-earth ions can then be doped into host crystals such as $Y_3Al_5O_{12}$ (yttrium aluminium garnet, YAG) or Y_2SiO_5 (yttrium silicate, YSO). The host material affects the properties slightly, but most of the structure of the free ions is retained, since the main contribution comes from spin-orbit interaction and not crystal field interaction. A general, and for our purposes very useful, property of the rare-earths, is that the active electronic shells are shielded from the environment. There are 13 lanthanides that do not have full 4f shells, and they can all make inner 4f-4f transitions. The 5s and 5p shells are both full and energetically lower, but because of lower angular momentum, and thus less ellipticity, they are spatially outside (see Figure 3.1) the active 4f shell, acting as a shield against some dephasing mechanisms. A good overview of the spectroscopy of rare-earths in crystals was given by Macfarlane and Shelby [13] in 1987.

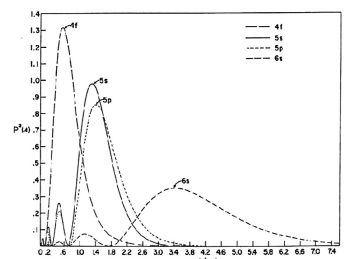

Figure 3.1. *Radial part of the wave function for orbitals of different angular momentum. Energetically lower, filled shells, are shielding the inner active shells.*

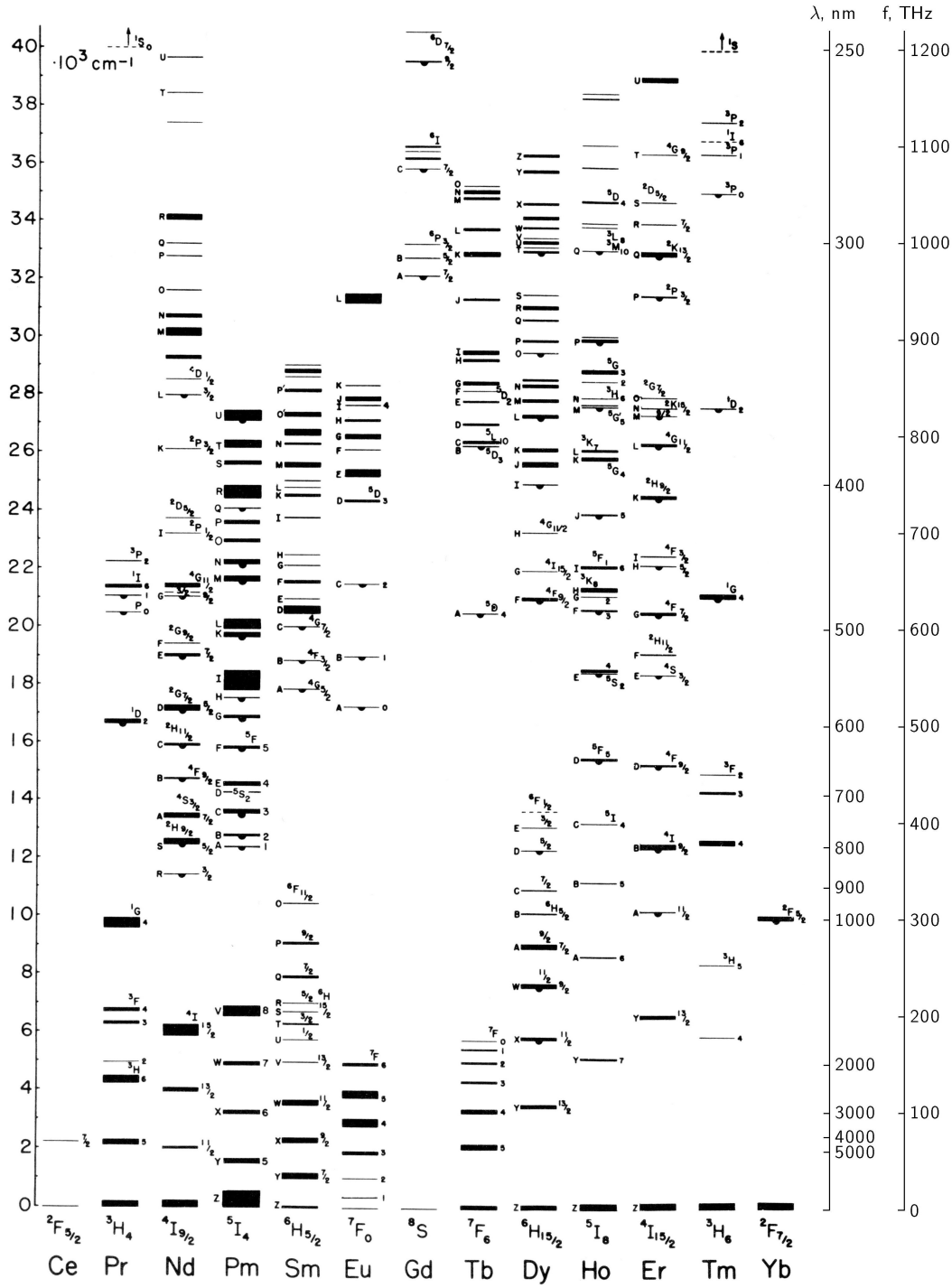

Figure 3.2. *Energy level diagram for all rare-earth ions. They were measured by Deike et al. [14], and correspond to trivalent ions doped into* $LaCl_3$ *crystals. The figure is reproduced from [15].*

Another way of utilizing ions for quantum computing purposes is trapping them artificially in, for example, ion traps or MOTs (magneto-optical traps). These techniques have been very successful in quantum computing, but using naturally trapped ions in these types of host crystals does offer some advantages. Experimentally, dealing with crystals is simpler than working with ion traps, which require well aligned magnetic fields for trapping as well as a very high vacuum. In addition, in ion traps, the ions are forced to be well separated because they are addressed spatially and there is a minimum laser focus. In crystal lattices on the other hand, the ions can have as little as sub-nanometer separations, which enables strong ion-ion, and thus also qubit-qubit, interactions. For rare-earth-ion-doped solids the addressing can be done spectrally, as discussed in Section 3.4.

3.1 Why work with the Rare-earths?

The main reason for choosing rare-earths for coherent quantum experiments, is long coherence times. Free rare-earth ions have long lifetimes due to forbidden transitions to the ground state, which become weakly allowed due to interactions with the crystal field of the host material. Long lifetimes also give potentially long coherence times. Some of the rare-earths are also what are called non-Kramers' doublets, whose electronic angular moments are quenched by the crystal field, which means that they have no first-order Zeeman or hyperfine interactions. This, together with the outer shell shielding, means they couple only weakly to the dephasing environment, ensuring that the coherence time, T_2, is as long as possible. It should be noted that, to obtain these good coherence properties it is necessary to keep the crystals at liquid helium temperatures, i.e. $< 4\,\mathrm{K}$. Above this temperature, crystal lattice phonons contribute strongly to decoherence mechanisms.

Another important feature is the availability of a small hyperfine splitting of the electronic states. This occurs for the rare-earths that have non-zero nuclear spin, which couples by second order hyperfine or quadrupole interaction. Relaxation between the hyperfine levels in the electronic ground state is even less allowed, and with such a metastable character, they are very good for quantum information processing. For this, at least two hyperfine states are needed, representing the $|0\rangle$- and $|1\rangle$-states, but some of the protocols, like quantum computing, also require additional hyperfine levels to act as auxiliary states, $|\mathrm{aux}\rangle$, into which the ions are temporarily put during the process. This will be explained further in Section 3.7.

The host crystal will affect the size of the hyperfine splitting, and for Pr^{3+}:Y_2SiO_5, which is the crystal used most extensively in our experiments, the splitting is shown in Figure 3.3**a**.

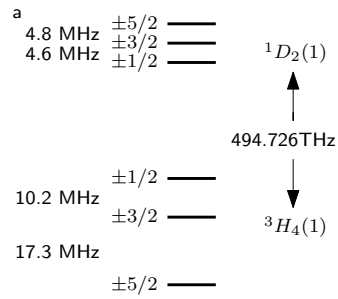

b

g \ e	±1/2	±3/2	±5/2
±1/2	0.56	0.38	0.06
±3/2	0.39	0.60	0.01
±5/2	0.05	0.02	0.93

Figure 3.3. *Properties for Pr^{3+}:Y_2SiO_5. In* **a** *the level structure of Pr^{3+} is shown and* **b** *contains the relative oscillator strengths for all 9 possible transitions.*

3.2 Crystal properties

The rare-earth-ion crystals are produced by mixing the appropriate amounts of the elements involved, in gaseous form, in a chamber. By controlling the temperature and pressure, the crystal growth process can be regulated.

The Y_2SiO_5 crystal has a monoclinic crystal structure, which is a rectangular prism with a parallelogram as its base. The unit cell is $1.04 \times 0.67 \times 1.25$ nm^3, contains 8 molecules, and thus 16 yttrium atoms. There are two non-equivalent yttrium sites, which means that for Pr^{3+}-doped crystals the praseodymium can also end up in two different sites. Roughly 90% of these occupy site 1, which has a wavelength of 605.813 nm. The rest are in site 2 which is 2 nm away, at 607.770. For our experiments, we are interested only in site 1, which has a transition dipole moment of $2.5{\cdot}10^{-32}$ Cm [16][1]. The Pr^{3+} ion in this host also has a permanent electric dipole moment, which for each site can be oriented in two energetically equivalent directions, and the angle between the two directions is 24.8°. It is assumed that the transition dipole moment is oriented along the same directions as the permanent one, but in experiments, the crystal is most often just rotated until maximum absorption is obtained, which should be half-way between the two directions, getting an equal contribution from both.

3.3 Homogeneous linewidth

For Pr^{3+}:Y_2SiO_5, the transition $^1D_2 \rightarrow {}^3H_4$ has a population decay rate of $\frac{1}{10}$ ms at liquid helium temperatures. From that level however, most ions do not decay directly to the ground state, but via some of the intermediate states (see Figure 3.2), resulting in a total lifetime of $T_1 = 164\,\mu s$. As mentioned in the previous chapter, the lifetime gives an upper limit to the coherence time of the state in the form of $T_2 \leq 2T_1$, with equality if there are no other significant sources of dephasing than state decay. For rare-earths however, there are usually also some other dephasing mechanisms, such as crystal field fluctuations caused by random spin flips of neighboring atoms. The effects of the spin flips can be minimized by choosing a crystal host that has atoms with low nuclear magnetic moments. One can also apply external magnetic fields, either with low strength to make sure ground and excited states do not shift, or shift equally, to first order, or with high magnetic strength to prevent spin flips altogether.

For Pr^{3+}:Y_2SiO_5, T_2 of the electronic transition is about 110 µs [17], giving a spectral width of 2.8 kHz according to Equation (2.19), which is very narrow for a solid state material. This

[1] This value can also be expressed as $7.5 \cdot 10^{-3}$ Debye, which is a common unit for dipole moment.

value was measured in photon echo experiments, where the data was extrapolated to zero excitation energy. With increasing pulse energy the number of excited atoms is increased, and since the permanent dipole moment is different for the ground and excited states the fields in the crystal will change as atoms are excited, causing extra dephasing. This is called spectral diffusion or excitation-induced broadening. As an example, for a reasonable excitation energy of about 1 mW focused down to a spot with a diameter of 100 µm, the coherence time was halved to about 50 µs [17]. These values are obtained in zero external magnetic field, and with an applied field of 7.7 mT the coherence time is increased to 150 µs. Other rare-earths can have even longer coherence times, for example 6.4 ms reported in $Er^{3+}:Y_2SiO_5$ [18].

3.4 Inhomogeneous broadening

The line broadening mechanisms described so far are all homogeneous, meaning they are caused by something that affects all atoms the same way. The rare-earth ions however, also exhibit inhomogeneous broadening, caused by the fact that all ions are situated in different positions in the crystal where different crystal fields exist. The crystal fields are spatially dependent, partially because of manufacturing imperfections, but also because the Pr^{3+} ion has a different size than the Y^{3+} ion it is replacing in the lattice, which causes unavoidable deviations from the perfect crystal lattice in its proximity. As mentioned in the previous section, the homogeneous linewidth is of the order of kHz, which can be compared to the inhomogeneous width of ∼5 GHz in the case of Pr^{3+}:Y_2SiO_5 .

In many other type of experiments, inhomogeneous broadening is unwanted and can reduce the accuracy of measurements, or call for additional experimental complications to remove it, but in our case it is found to be very useful. For the quantum computing scheme, it is in fact the main mechanism for addressing multiple qubits. Even a small laser focus with a diameter of ∼ 10 µm, will, with a standard doping concentration of 0.05 %, contain in the order of 10^{12} Pr^{3+} ions, which cannot be spatially separated by the laser. But with the inhomogeneous broadening they can be further separated if addressed spectrally. With a kHz homogeneous linewidth and a GHz inhomogeneous width, the maximum number of available frequency channels is about 10^6, giving a high potential for many qubits. In practice however, there are some scaling issues in utilizing this power, which will be discussed in Chapter 5.

3.5 Hyperfine levels

The rare-earth elements that have a nuclear spin greater than 1/2 also have a hyperfine splitting of all electronic levels. Pr^{3+} for

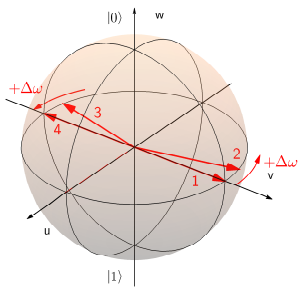

Figure 3.4. *Bang-bang pulse sequence can be used to cancel random frequency shifts. We start with the desired state at 1, then a frequency shift of $+\Delta\omega$ causes a rotation counter clockwise compared to our reference frame onto the position 2. Here, a fast π-pulse is applied that takes the state over to 3. The direction of rotation has not changed if the noise is on a slower timescale than the flips and the state will thus rotate towards position 4. The $-\pi$-pulse is applied and the state is back to the original one, with the phase error due to noise canceled out.*

example, has a nuclear spin of 5/2 and thus each electronic level is split into 6 hyperfine states, labeled $|\pm 1/2\rangle$, $|\pm 3/2\rangle$ and $|\pm 5/2\rangle$, which at zero magnetic field are two-fold degenerate to yield only 3 resolvable levels. One must be cautious however, when applying magnetic fields to increase the coherence time as described above, because this will also lift the degeneracy of the levels, which may not always be convenient.

The lifetime of the hyperfine levels is much longer than for the electronic states. For Pr^{3+}:Y_2SiO_5 for example, $(T_1)_{hf}$ is 90 s, and $(T_2)_{hf}$ is about 500 µs at zero field and as high as 860 ms for non-zero fields [19, 20]. It is also possible to further decouple the quantum state from the dephasing environment by the use of what is called bang-bang pulses. In this technique [20], if one has a quantum state in a superposition that is to be preserved, a sequence of pulses with a pulse area of alternating π and $-\pi$ can be sent in. This periodical flipping can strongly reduce the effects of any dephasing mechanisms that happen on a time-scale longer than the period of the flips. As discussed in Section 2.3.2, dephasing mechanisms are changes in the environment, such as nearby spin flips, that cause the energy levels to shift slightly, which also changes the oscillation frequency of the superposition state. The π-flips will cause the sign of this frequency error also to flip, which will make the total phase of the state accumulate as much positive contributions as negative ones, strongly reducing the phase error. This procedure is further explained in the caption to Figure 3.4.

The splitting of the hyperfine levels is of the order of 10 MHz for Pr^{3+}:Y_2SiO_5 (see Figure 3.3) but it can be up to GHz in other host materials or for other ions. There is also an inhomogeneous broadening of the hyperfine states, which we have measured to be about 16 kHz. This was measured by putting the hyperfine levels into a superposition and measure the decay of the resulting beating by probing on the optical transition at different time intervals.

3.6 Ion-ion interactions

The same permanent dipole moment that was responsible for the excitation-induced frequency shift described earlier in Section 3.3, is also very useful for getting qubit-qubit interactions in the quantum computing scheme. The idea is that if a target qubit has a certain frequency width, for example 100 kHz, we want to find a similar control qubit, that when excited, shifts the center frequency of the target by more than its width. A laser pulse on the original target qubit frequency will then no longer interact with it, and we can use this for conditional operations between the two qubits. The shift declines as the cube of the distance, and for our materials some rule of thumb values are: at a 1 nm ion separation

the shift is approximately 1 GHz, at a 10 nm separation it is 1 MHz and so on. For a qubit width of 100 kHz, the maximum distance the ions are allowed to be separated for the scheme to work is then about 20 nm. At greater distances the shift will be insufficient to be able to distinguish between shifted and unshifted ions. The ion-ion interaction will also be discussed in Section 5.4, in connection with two-qubit gates.

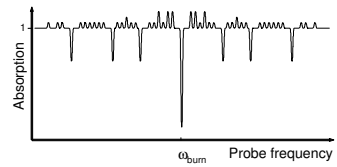

Figure 3.5. *The intricate pattern of holes and anti-holes is formed by different combinations of ground and excited state hyperfine levels. The different sizes of the features are a product of the number of atoms in each level and the relative oscillator strength for the transition.*

3.7 Hole-burning techniques

A very useful technique for dealing with inhomogeneous atomic systems is spectral hole-burning. The simplest case of hole-burning is a two-level system where the absorption coefficient is decreased as a result of atoms being transferred to the excited state by, for instance, a laser. This is also called transient hole-burning, since the effect will disappear as soon as the atoms decay back to the ground state. There are also other types of more persistent hole-burning, which involve optical pumping of atoms to additional metastable levels, as in the case of Pr^{3+} which we are interested in. If the absorption is bleached in this way, it means that there are now more atoms absorbing on the other level, to which they decayed. The peak in the absorption profile that this gives rise to is called an anti-hole. In Figure 3.5 a full array of holes and anti-holes is shown.

3.7.1 Spectral pit creation

By scanning the laser in frequency it is possible to create a wide hole, known as a spectral pit, illustrated in Figure 3.6. The maximum pit width is determined by the splitting of the hyperfine states and the fact that the atoms have to be in one of the states. The total splitting of the ground states is 27 MHz (see Figure 3.3), but then, because of the inhomogeneity of the relative position of the excited states, the maximum width is reduced by the excited state splitting of 9 MHz, down to 18 MHz.

The straight edges that the pit in Figure 3.6 has, is not an optimal solution. Atoms just outside the pit can still be off-resonantly excited by pulses of frequencies inside the pit, as has been discussed in Ref. [21]. To limit this effect, we must attempt to make sure that atoms are put into states which are as far away from the pit as possible, as demonstrated in Figure 3.7. If we burn only inside the pit, the structure would look like the one in Figure 3.6, shown by a thin dashed line in Figure 3.7, where the selected atoms exist in both $|3/2\rangle$ and $|5/2\rangle$. With additional burning pulses outside the pit, followed by more inside the pit, we can transfer all atoms out to $|5/2\rangle$, i.e. as far away as possible. The pit edge will now become stepped, as shown by the solid line.

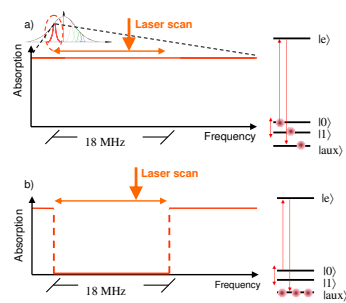

Figure 3.6. *In a) the starting situation is shown, with all the ions in the inhomogeneous profile in thermal equilibrium. After the hole-burning pulse sequence, a spectral pit is formed.*

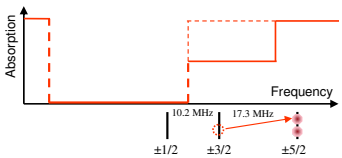

Figure 3.7. *Improved pit burning scheme. By cleverly selected burning pulses, we can ensure that atoms are as far away from the pit as they possibly can, by moving them out to the ±5/2 state in the case of atoms with these particular level positions.*

It should be pointed out that in the above discussion and in the figures, the ions were thought to have a higher frequency than the center of the pit. Ions with lower frequency than the center should, of course, be shifted towards even lower frequencies, in order to get as far away as possible. This would mean that they end up in the $|1/2\rangle$-state, after the improved pit creation pulses.

3.7.2 Experimental implementation

The actual pulse sequence that is used to create a spectral pit is not trivial and very dependent on the particular level structure of the given ion and host material. For Pr^{3+}:Y_2SiO_5 the burn pulses we employed are listed in Table 3.1.

Pulse	ν_{start}/MHz	ν_{end}/MHz	Ω_{rel}
BurnPit1	+31.85	+24.15	$3/2_g \rightarrow 1/2_e$
BurnPit2	+23.85	+16.15	$3/2_g \rightarrow 5/2_e$
BurnPit3	+15.95	+7.65	$3/2_g \rightarrow 5/2_e$
BurnPit4	+23.85	+16.15	$3/2_g \rightarrow 5/2_e$
BurnPit5	-16.85	-9.15	$5/2_g \rightarrow 5/2_e$
BurnPit6	-8.85	-1.15	$5/2_g \rightarrow 1/2_e$
BurnPit7	+15.95	+7.65	$3/2_g \rightarrow 5/2_e$
BurnPit8	+7.35	-1.10	$3/2_g \rightarrow 5/2_e$
BurnPit9	-1.10	+7.35	$5/2_g \rightarrow 1/2_e$
BurnPit10	+7.65	+15.95	$5/2_g \rightarrow 1/2_e$

Table 3.1. *List of pulses used for the pit burning sequence, with start and end frequencies. The column of Ω_{rel} lists the primary target transition of the scan, for the purpose of matching the rabi frequency to the relative oscillator strength. Note that pulses number 2 and 4 are the same, as is pulses 3 and 7.*

The pulses listed in Table 3.1 are of a special type which we have called *SechScan*. As the name implies it is a cross between a simple frequency scanned pulse, and a sechyp pulse. The start and end frequencies specified in the list are the values for the linear scan part in the middle of the pulse. To this otherwise square-shaped scan we have then added rounded edges in the form of a sechyp shape for the amplitude and a tanhyp shape for the chirp. The reason for rounding of the edges in this manner is to avoid sharp temporal features, which would result in high order frequency components. The fitting between the linear and the sechyp parts have been done with splines that check for continuity of the function, as well as of the subsequent derivatives. These pulses are then repeated in an iterative sequence in the following manner:

1 *Repeat 60 times:*
BurnPit5, BurnPit6

2 *Repeat 30 times:*
BurnPit1-4, BurnPit6-10

3 *Repeat 20 times:*
BurnPit1-4, BurnPit6

4 *Repeat 30 times:*
BurnPit7-10

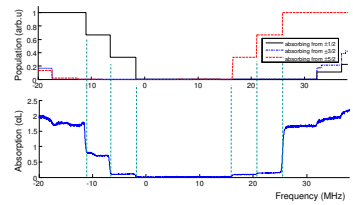

Figure 3.8. *Theoretical simulation of a pit-burning sequence in* **a)***, and the same sequence detected in the lab in part* **b***. The ∼ 18 MHz that has zero αL is the bottom of the pit, while anything non-zero is outside.*

It is important to note that there is a waiting time of about 1 ms after every single burn pulse, to allow the system time to decay back to the ground state. The number of times each sub-sequence is repeated is determined by the relative decay probabilities to the different levels, to which the system will decay. The values listed are not the only ones possible, one could imagine other values, but these are simply the ones we actually used.

A simulation of the system (described in [21]), was found very useful in the search for the exact burning sequence and while testing different combinations of pulses. The result of the simulation for the list of pulses above is shown in Figure 3.8**a**, and the **b** part corresponds to the experimental implementation of the same pulse sequence. As can be seen, the steps that were a result of the improved pit-burning scheme, match very well in frequency but not in height. The reason for the step height discrepancy is that the y-axis in **a)** is the *number of atoms*, while it is the *absorption* in **b)**. In an absorption measurement, the relative oscillator strength also needs to be factored in, and steps with low heights thus stem from transitions with low oscillator strengths.

3.7.3 Peak creation

After a wide pit has been created, a narrow selection of ions is burnt back into the pit to act as a qubit. Inside the pit, the qubit ions are now well separated from all other ions, which means that the effects of the interacting laser pulses, on non-qubit ions, is kept to a minimum. The pulses used to create the peak are two sechyp pulses, the first one on the $|5/2\rangle_g \rightarrow |5/2\rangle_e$ transition, exciting ions outside the pit with a frequency width given by the sechyp pulse parameters. This pulse is then followed by a sechyp pulse on the $|5/2\rangle_e \rightarrow |1/2\rangle_g$ transition, bringing the ions to the ground state. Inside the pit, all ions now exist in a single ground state level, i.e. the system has been initialized to $|0\rangle$, as shown in Figure 3.9. There is a reason for choosing $|5/2\rangle$ as the intermediate excited state, and not any of the others. For this particular state, the first transition ($|5/2\rangle_g \rightarrow |5/2\rangle_e$) can use a very low laser intensity, since this transition has a very high oscillator strength. Low intensity means better performance, since we thereby reduce effects such as power broadening and off-resonant excitations. The price we pay for this is that the deexcitation ($|5/2\rangle_e \rightarrow |1/2\rangle_g$) will require high

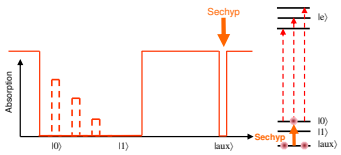

Figure 3.9. *Sechyp pulses applied to ions outside of the pit will efficiently transfer them into the pit in the form of a spectral peak, which will act as a qubit.*

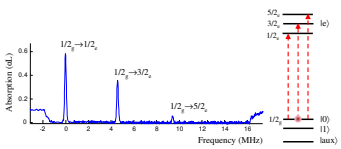

Figure 3.10. *Experimental version of Figure 3.9. The different size of the peaks are due to the different relative oscillator strengths, as can be identified in the table in Figure 3.3b. The three peaks mean all ions are in the same ground state, i.e. the system is initialized to the $|0\rangle$-state.*

laser power, because the oscillator strength on this transition is complimentarily weak. This is however not a problem, because the frequency for this transition is inside the pit, where no other ions are located, and consequently, the effects of power broadening and off-resonant mechanisms are greatly reduced.

An experimental readout scan with peaks inside the pit is shown in Figure 3.10. The figure shows the qubit initialized to the $|0\rangle$-state, which is the starting point for most experiments in this thesis.

Chapter 4

The experimental system

Having atoms that have a very long coherence time is important in quantum computing, as described in the previous chapter, but the coherence time of the atoms means nothing if the device that controls them cannot retain its own phase. It was therefore necessary to construct a laser at the right wavelength, with at least the same phase stability as the Pr^{3+} ions used for the qubits. A system to create the advanced pulse shapes needed for the experiments was also developed and will be discussed in this chapter.

4.1 Choice of laser source

There are many different types of lasers available on the market, ranging from compact lasers like the diode laser, used in everything from CD-players to pumps for bigger lasers, up to the carbon dioxide laser, which is a high power industrial gas laser, but each of these lasers function only in a very restricted wavelength region. Depending on the exact mechanism of the lasing for each type they also have varying degrees of natural stability. For example, solid state lasers, such as the diode laser or neodymium-based lasers are naturally more stable than discharge lasers, such as the argon ion laser or liquid based lasers such as the dye laser. Therefore, solid state lasers would be a preferable choice of source for coherent experiments, but unfortunately there was no solid state solution available that could reach the desired wavelength of 606 nm. There are diode lasers available down to 633 nm at room temperature, which can be taken down further by cooling with liquid nitrogen. This was tested but it was possible to reach only about 612 nm. There is then a large gap of available wavelengths down to about 400 nm, where GaN lasers have just recently become available. The best option was therefore deemed to be a dye laser, with an extra stabilization system.

4.1.1 Dye laser

The laser used in most of the experiments for this thesis is an externally stabilized, continuous dye laser, based on the commercially available Coherent 699-21 ring cavity dye laser. The dye used is Rhodamine 6G, which can be tuned to 606 nm at the edge of its tunable range. This dye is dissolved in ethylene glycol, pumped through a narrow nozzle at 4-5 bar pressure, and kept at a temperature of 8° C, using an active temperature stabilization system. For a given cavity alignment it is important to keep parameters such as dye pressure and viscosity, and thus temperature, constant, because any changes can lead to the dye jet changing position, which will negatively affect the stability of the laser.

The dye is pumped by a Verdi V6 system, which is a neodymium laser at 532 nm giving 6 W power, which in turn is pumped by a 20 W array of laser diodes at 800 nm. With all intracavity components mounted, the dye laser will give a maximum output power of about 600 mW at 606 nm when it is optimally aligned. From the original dye laser a number of things have been altered or added. The nozzle as well as the holder for the pump mirror have been replaced by an assembly made by Radiant dyes, for increased performance. An intra-cavity EOM (Electro-optic modulator) with very low losses, was added, to be used as an actuator for the stabilization system described in the next section. To this end the error signal from the internal locking system of the dye laser, was also changed to include a signal from our external, more accurate, error signal.

4.2 Laser stabilization

The stabilization of the laser was done using a coherent hole-burning technique, rather than as usual, by locking to a fixed cavity. The theory that was developed with regards to this technique is described in Paper **I**, while the electronics that was constructed is discussed in detail in the thesis of Lars Rippe [22], who designed them.

4.2.1 Introduction to the locking system

A schematic overview of the dye laser stabilization system is presented in Figure 4.1, and a real picture of it is shown as Figure 4.2. The original Coherent dye laser has an internal stabilization system, which can keep the linewidth of the laser at about 1 MHz. The task of our stabilization system is to further narrow this linewidth down to about 1 kHz. Due mostly to the liquid jet, dye lasers are not the most naturally stable lasers. Nevertheless dye lasers have been used in the past for extreme stabilization down to a linewidth

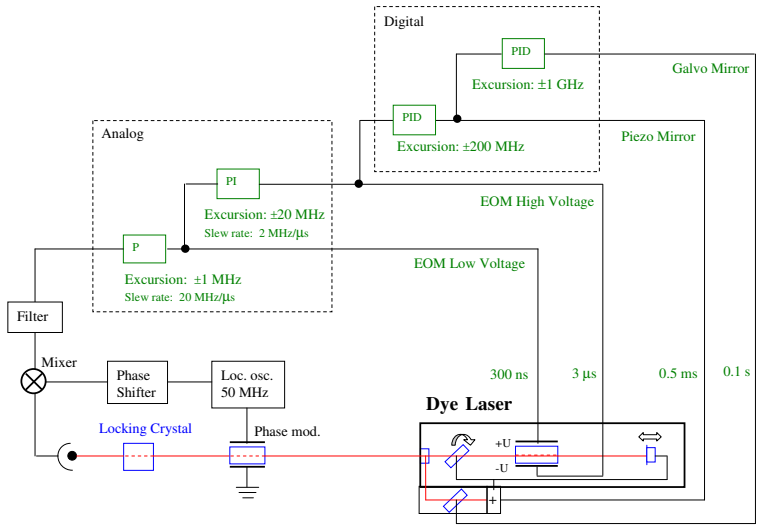

Figure 4.1. *Overview of the laser stabilization system. Detection of a 50 MHz modulation of a part of the laser beam that has gone through gives rise to an error signal which can be fed through a series of feedback filters on different time scales, and onto the laser correcting any frequency errors.*

of about 0.5 Hz [23, 24], although that required an extreme experimental setup as well.

There are some advantages of locking to a spectral hole rather than to a cavity. For example, when locking to a cavity, it is very important to stabilize the cavity itself, as any vibrations or variations of length will directly limit the stability. Variations of the cavity length can be particularly detrimental because for high finesse cavities the light makes many roundtrips, greatly increasing the effect of a change in length. Cavities are therefore typically made of Ultra Low Expansion glass (ULE), in addition to requiring temperature stabilization down to an accuracy of mK. When locking to a spectral hole, this is not an issue since the potential stability is mainly determined by the coherence time of the atoms. On the other hand, a cryostat setup is needed to cool the atoms for spectral hole locking, but it can still be regarded as a bonus, since the coherence time and thus the stability is not effected by temperature changes of the atoms (once you go below $4 - 5$ K).

Another interesting benefit of locking to holes, is related to coupling the light to the locking mechanism. For cavities, high stability requires high finesse, which makes it very difficult for the light to get coupled into the cavity, maybe even impossible for the initially broad laser, in fact, a pre-lock system may be required, to narrow the laser enough to get it into the cavity. This is taken care

Figure 4.2. *Picture showing the laser stabilization setup.*

of automatically for spectral holes, since at the start when the laser is broad, the spectral hole is also broad, and as the laser narrows the hole narrows, acting like a form of self-regulating finesse.

4.2.2 Theoretical overview

Our locking system is based on getting a response from the atoms that gives an indication of the size of the phase error of the light, if there is any. This section will give a brief introduction to what happens in the locking crystal and what the atomic response, the system transfer function, looks like. This function can then be used to create a feedback filter in the form of a series of control loops.

Transfer function

As illustrated in Figure 4.1 the light beam from the laser goes first through an EOM and then the crystal with the Pr^{3+} ions, to be detected further on. The EOM is modulated with a 50 MHz sinusoidal signal from a stable local oscillator. The light after the EOM can be seen as a carrier wave plus two sidebands at ± 50 MHz. If the light could originally be written as a complex Rabi frequency, $\Omega_0 e^{-i\omega_0 t}$, then after the EOM, it can be expressed as

$$\begin{aligned}\Omega(t) &= \Omega_0 e^{-i(\omega_0 t + m\sin(\omega_m t))} \\ &\approx \Omega_0 \left[J_0(m) + J_1(m)e^{-i\omega_m t} - J_1(m)e^{i\omega_m t}\right] e^{-i\omega_0 t},\end{aligned} \tag{4.1}$$

where m is the modulation index, the strength of the sidebands, and $\omega_m = 2\pi \cdot 50$ MHz is the modulation frequency. The lower line in this equation is obtained by expansion of the signal in terms of Bessel functions, and it is here assumed that the modulation index is so low that higher order terms can be neglected.

The light at these three frequency components then enters the crystal where atoms at the same three frequencies start getting excited. Within the coherence time of the atoms, the excitation essentially puts the atoms into a superposition state. As is explained in Section 8.1, this will cause the atoms to radiate coherently along the same mode as the incoming light (although with the opposite phase). Some light will be absorbed by the atoms and give rise to this coherent radiation, but some light will pass through the crystal unaffected. After the crystal we therefore have six light field components, three from the atoms and three from the unaffected laser light. These six components will create a total beat pattern that can be detected in the form of the intensity, i.e. $I \propto |\Omega_{tot}(t)|^2$. If there is a sudden phase error, ϵ, in the laser, then the three unaffected components will change accordingly, but the three components from the atom radiation will still radiate at the original frequency, with the original phase. This change to half of the components in the total beat pattern, will naturally also give rise to a change in the beat pattern itself. A harmonic phase error, $\epsilon \sin \omega t$, can be introduced as a modulation to an otherwise stable laser, i.e. we replace $\omega_0 t$ in Equation (4.1) by a resulting laser phase

$$\varphi_{laser} = \omega_0 t + \epsilon \sin \omega t. \tag{4.2}$$

The total resulting light intensity coming out of the crystal was calculated in Paper **I**, where the details can be found. Here only the result will be given:

$$I_{out}(t) = 4 I_{in} J_0 J_1 \mathrm{Re}\left[T(\omega)\right] \epsilon\omega \cos\omega t \cdot \sin\omega_m t, \tag{4.3}$$

where

$$T(\omega) = \frac{\eta_c(\omega)\eta_s(0)e^{i\phi_c(\omega)} - \eta_c(0)\eta_s(\omega)e^{i\phi_s(\omega)}}{i\omega + \frac{1}{T_{hole}}}. \tag{4.4}$$

Here, T_{hole} is the lifetime of the hole, and $\phi_i(\omega)$ and $\eta_i(\omega)$, with $i = c$ for the carrier and s for sideband, is the phase change and attenuation respectively, that arise from the interaction of the light with the atoms as it passes through the crystal. The explicit expressions for these are not important for the discussion here, but can be found in Paper **I**. What is essential in the total signal, Equation (4.3), is that it oscillates with frequency, ω_m, and that the amplitude of this oscillation is proportional to the phase error, ϵ.

A further aspect of the lifetime of the hole, T_{hole}, should be noted. With no other influence, the lifetime of the hole would be the lifetime of the hyperfine states, which is more than 1 minute. This is a very slow, natural refilling rate, which can be compared to the hole digging rate, which is given by the laser intensity. Doing so, one would see that if we relied only in the natural lifetime the hole would soon be burnt all the way to the bottom, at which point the error signal would fail due to lack of interacting atoms left at that frequency. In order to prevent this from happening, an RF repumping system was created. A system of RF coils was put close to the crystal, and the coils were doubly resonant with both the 10.2 MHz and the 17.3 MHz hyperfine transitions. Varying the strength of the RF power provides a very convenient way to fine tune the hole lifetime, which in turn also tunes the depth of the locking hole.

Feedback response

In Equation (4.2) a phase error was introduced and we see that this gives an instantaneous laser frequency of

$$\frac{\partial \varphi_{laser}}{\partial t} = \omega_0 + \epsilon\omega \cos \omega t. \tag{4.5}$$

In the total light intensity in Equation (4.3) we can directly identify the instantaneous frequency error $\epsilon\omega \cos \omega t$, and we see that $T(\omega)$ acts as a transfer function, mapping this error onto the detected light intensity. Given this transfer function, we can now design a feedback circuit that compensates for the error. It is known from control theory that if the total response of the system, including both the transfer function of the atoms and our feedback filters, is proportional to $\frac{1}{i\omega}$ for all frequencies, then the system is stable [25]. The full spectral response of $T(\omega)$ was analyzed and for high frequencies ($\omega > \Gamma_{hole} >> 1/T_{hole}$) a suitable analog circuit was constructed. Similarly, for errors of low frequency ($\omega < \Gamma_{hole}$) a digital processing card was programmed with a correcting response function. As an example of how to pick such a correcting response function, we can consider the denominator of the $T(\omega)$, $\frac{1}{i\omega + \frac{1}{T_{hole}}}$, which is dominating for low frequencies. This part can

be stabilized with a feedback filter of the form $\frac{1/\tau+i\omega}{i\omega}$, since

$$\frac{1}{i\omega + \frac{1}{T_{hole}}} \cdot \frac{1/\tau + i\omega}{i\omega} = \frac{1}{i\omega}, \tag{4.6}$$

if $\tau = T_{hole}$. The value of τ can be chosen easily on a digital processing card, and for the fast analog response systems, similar critical constants can be tuned by choosing correct resistors and capacitors [22].

An interesting quantitative result was also obtained in Paper **I**. When locking to cavities, the optimal modulation index is 1.08 [26], while we obtained an optimal value of 0.56 for locking to spectral holes. The reason that the optimal value is less in the spectral hole case is that the error signal depends partly on the difference between the depth of the holes burnt by the carrier and those burnt by the sidebands, and a lower modulation index increases this difference.

4.3 Pulse-shaping system

The quantum computation scheme is based on using light pulses as gates for the operations. In order to compensate for inhomogeneities in both the spectral and the spatial domain, relatively advanced shapes for the pulses are required. As explained in Section 2.5, sechyp pulses can be used to achieve this compensation, and so we will need a system that can to a very high accuracy create this shape, and in our system this is done by AOMs. For the qubit rotation experiment (Paper **II**), we also require the option to drive two transitions simultaneously, both $|0\rangle \rightarrow |e\rangle$ and $|1\rangle \rightarrow |e\rangle$, and in order to do this we opted for a two-AOM setup, where the sechyp shape can be created in the first AOM, and where a second AOM is run with the sum of the two involved frequencies, effectively creating a sechyp pulse for each of the two transitions. A schematic of the experimental setup is shown in Figure 4.3.

The pulse shapes are created in Matlab on the computer, and sent to the AOM's using a 2-channel, 1 GS/S Tektronix 520 Arbitrary Waveform Generator (AWG), via some RF amplifiers. The oscilloscope is a 4-channel TDS540 Tektronix, with 1 GS/s sampling rate, and the detectors are Thorlabs PDB150A, which have a switchable gain function, that can be changed from a gain of 10^3 and bandwidth 150 MHz in 5 steps to a gain of 10^7 with a bandwidth of 0.1 MHz.

4.3.1 Acousto-optic modulators

An acousto-optic modulator (AOM) is a crystal with a piezoelectric element attached to it that can run at RF frequencies to

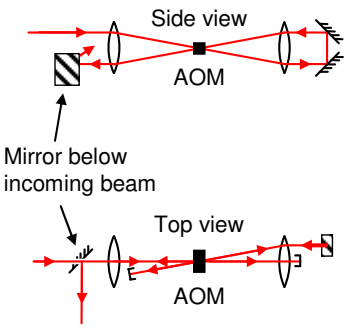

Figure 4.4. *An AOM in a double pass configuration, seen from both side and top view. The advantage of the setup is that it cancels out spatial movement due to frequency shifts.*

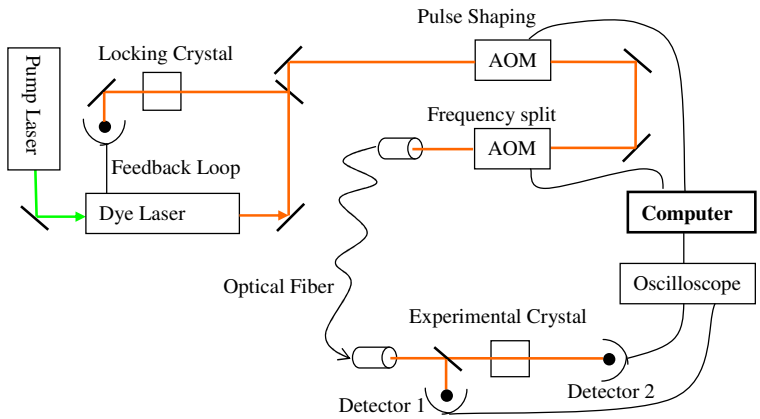

Figure 4.3. *An overview of the experimental setup. Approximately 4 % of the light is picked off for the locking system. The rest goes on through two AOMs, which create the pulses, and over to the experimental crystal, via an optical fiber, where it can be detected.*

induce wave patterns in the crystal. The sound waves created inside the crystal act as a Bragg grating, diffracting the light as it passes through. This Bragg grating also moves along the crystal, and the light that is reflected from the grating, is also doppler-shifted in the process. Another way of looking at this is to consider the sound wave as phonons. The light photons then have a chance of colliding with a phonon as it passes through the crystal, and if that happens it would pick up the phonon momentum, which, just as for classical particles, changes both its direction and energy, i.e. its frequency.

The spatial position of the diffracted beam will depend on the current RF frequency, and if the pulse shape contains a frequency chirp, the resulting beam will move spatially during the course of the chirp. To prevent this beam walk, a double pass configuration can be used, where the photons pass through the AOM twice, picking up phonons each time. The effect of this is a frequency shift twice as large, but, with a suitable alignment one can ensure that the changes of the direction for the first and second pass cancel out. A double pass setup can either be implemented using polarizers and $\lambda/4$-plates, or with non-orthogonal incoming and outgoing beams, which is done in our case, as seen in Figure 4.4.

Both our AOM's are from AA, made of TeO_2, which have a sound velocity of 4200 m/s. The first AOM has a center frequency of 200 MHz and a bandwidth of 100 MHz, for a total of 200 MHz bandwidth after the double pass, and the second AOM has a center frequency of 360 MHz and a bandwidth of 200 MHz.

4.3.2 Calibration system

The diffraction efficiency is typically about $50-80$ % per pass, at maximum RF power, which is about 2 W. The efficiency changes with RF frequency, and scales with RF power according to

$$I_{diff} \propto \sin^2\left(c\sqrt{P_{RF}}\right), \tag{4.7}$$

where c is a scaling coefficient. This behavior is illustrated in Figure 4.5. The sechyp (and other) pulses needed, can have greatly varying intensities. To make sure that any intensity can be accurately produced, we need a function that, given a desired intensity, returns the corresponding RF power, and does so correctly for any RF frequency. Simply using Equation (4.7) is not accurate enough, since we require the error to be at least less than 1 % over a calibration range of more than six orders of magnitude in intensity. In addition, Equation (4.7) does not account for the RF frequency dependence. To get such a function, $P_{RF} = f(I_{light}, \nu_{RF})$, a calibration system was designed.

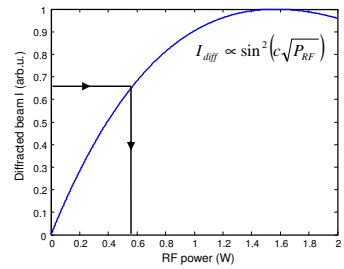

Figure 4.5. *Graph showing the intensity in the diffracted beam as a function of RF power. The arrows illustrate that a function is needed to find the RF power for any pulse intensity value.*

The calibration system is connected to both the waveform generator that controls the AOM's and to the oscilloscope that receives the signals from the detectors. Since the intensity of the diffracted beam depends on two variables, it is convenient to keep one variable constant and scan the other, while reading the result on the detector. And since we want the intensity to scale over six orders of magnitude, the RF power should be kept constant while the 200 MHz total bandwidth of the AOM is covered. This operation is then repeated for numerous values of the RF power. The advantage of keeping the RF power constant for each scan is that the detectors can be kept at a suitable trans-impedance gain throughout the scan, and be changed only between the scans, which greatly increases the accuracy over such a large dynamic range. In order to keep the calibration system fully automatic, a motor, physically switching the gain on the detector, was controlled via pulse-width modulation [27] through one pin on the serial port on the computer. The oscilloscope gain was also controlled by the calibration program, and obtained via an algorithm that analyzed each resulting scan, repeating a previous scan with new settings if required.

With this method the function $I_{light} = f^{-1}(P_{RF}, \nu_{RF})$ is obtained, which has the geometrical shape of a surface in a 3-dimensional space. To get the desired function, f, we need to invert this surface with respect to the two variables I_{light} and P_{RF}. After the inversion the function must be stored in such a way that it can be called very efficiently. It is not uncommon for pulses in our experiments, to be around 100 µs, which with a 1 GS/s rate, corresponds to 100 000 sample points on the AWG. Since the function f needs to compute the required RF power for each sample point, for potentially very many pulses, it becomes clear that this

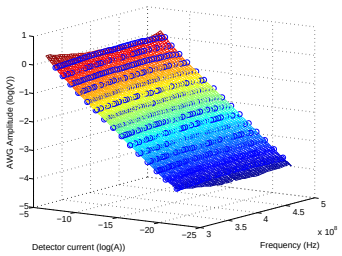

Figure 4.6. *A typical calibration curve. The blue rings mark the points in the lookup table, and the mesh illustrates the space available through interpolation. Note that the axes corresponding to the AWG signal and the detector current (which is proportional to the light intensity) are given in log scale.*

operation must be very efficient while maintaining the high accuracy. We therefore chose to store, not the function directly, but rather a logarithmic lookup table of it. In log space the function is almost completely linear (at least in the P_{RF} variable), and any function calls can be computed very efficiently from a few points in the lookup table using simple linear interpolation techniques, which greatly speeds up the process. An example of a calibration surface is given in Figure 4.6.

A special calibration for the second AOM is also required. As mentioned earlier, the task of the second AOM is to split the pulses in frequency to match the two qubit transitions. This operation causes an additional non-linear change to the dependence of the intensity on the RF power, because the two frequency components will "steal" power from each other at high total RF powers. This can be compensated for by a two-color scan that varies the amplitude for both frequency components, and for each value of one component, records the corresponding value of the other component.

4.3.3 Pulse sequence interface

Given that the pulses themselves are fairly advanced, each with many control parameters, and that the timing between them would also be important for some pulse sequences, it was clear that software that could manage this in a fast and flexible way would be required. The exact pulse sequences will be described in more detail in Chapter 5, but a few words can be said here about the timing requirements for the sequence. If we put the atoms in a superposition of the ground and excited state, the phase of that state will oscillate with a frequency corresponding to the energy difference between the two states. The exact frequency of the atoms that are targeted by the laser pulse is given by $\nu_{atom} = \nu_{laser} + 2 \cdot \nu_{AOM1} + \nu_{AOM2}$, since the laser frequency is shifted when it passes through the AOM system. If we make two successive coherent operations on the atoms it is clear that the relative phase of the light and the atoms is important. The same light pulse could for example drive the atoms up just as well as down in the Bloch sphere, depending only on this relative phase. Thus, we need to keep track of the phase evolution that the atoms go through because of their oscillation. During whatever time, τ, we wait between the two coherent pulses, the atoms will have evolved a total phase of $\phi_{atom} = \nu_{atom}\tau$, while the laser has only gained a phase of $\phi_{laser} = \nu_{laser}\tau$. The AOM's do not evolve by themselves while we wait for the next pulse, and so, to be able to set the second pulse to the correct phase, this difference $\phi_{AOMs} = (2\nu_{AOM1} + \nu_{AOM2})\tau$, must be added manually in the program to any coherent pulses.

The software, besides handling simple communication to the oscilloscope and waveform generator, is divided into two sections.

In one section, all the parameters of all pulses to be used in the current sequence, are defined, and in the other section the ordering of each pulse within the sequence is listed. The pulse parameters include for example duration, amplitude and center frequency, and specialized parameters such as the β and μ coefficients for sechyp pulses. Most of the parameters are decided only by individual optimization of each pulse, but some parameters, such as the starting phase of the pulse, is more complicated to determine. As discussed above, the phase of a pulse may depend, for example, on the time since the previous pulse was sent in, meaning that there are parameters that depend on their position in the sequence. To handle this dependence, both the pulse definition list and the sequence list are usually generated from a Matlab script that can keep track of the atom - laser phase discrepancy created by the AOM's.

4.4 Other equipment

4.4.1 Lab environment

The room that contains the stabilized system and the experimental crystal and detection system, is temperature as well as humidity stabilized. The optical table with the stabilized laser is housed in a clean room, class 100. The clean room is from Terra Universal, with the MAC 10 IQ HEPA filters and fan units from Envirco. The DC motor fan units were specially selected because of low noise, only 48 dB, producing low vibrations as well as providing comfortable working conditions.

4.4.2 Cryostats

As can be seen in the experimental setup, Figure 4.3, there is a need for two cryostats, one for the locking crystal and one for the experimental crystal. Both cryostats are made by Oxford Instruments, but function slightly differently. The cryostat for the locking system is a flow cryostat, in which a constant flow of helium fluid cools down a coldfinger, which then in turn cools down the crystal. There is no direct contact between the helium and the crystal, which makes it important that the coldfinger is very efficiently in touch with the crystal. The crystal mount is in fact a part of the coldfinger, and encloses the sides of the crystal very closely, where thermally conducting vacuum grease is used to bridge any small remaining gaps between the mount and the crystal. During the experiments it turned out that in order to get the crystal temperature low enough, we were forced to tighten the mount screws so much that the mechanical pressure on the crystal significantly changed the inhomogeneous Pr^{3+} absorption profile. There was an average shift of the absorption line in the order of GHz (the same order as Γ_{inh}), but more interestingly, because the pressure

was unevenly distributed, there appeared a strong spatial dependence of the line across the crystal. This caused the total width of the line to be roughly doubled and when scanning the frequency across the structure, the spatial inhomogeneity could be seen even with naked the eye as a dark band of absorption moving across the crystal.

The cryostat for the experimental crystal is a bath cryostat, which means that the crystal is fully submerged in liquid helium. This provides good cooling power, but requires the chamber to be pumped down to a pressure of less than $\sim$50 mbar in order to cool the helium to below 2.17 K, at which it becomes a superfluid. In the superfluid regime the helium boils without producing bubbles, which ensures a clean passage for the light pulses, as bubbles in the helium would scatter the light quite significantly. This cryostat is also equipped with superconducting magnets capable of generating a magnetic field of up to 8 T. This magnetic field could be used to increase the coherence time in the material, as explained in Chapter 3.

Chapter 5

Quantum computing

In this chapter the ideas of rare-earth quantum computing (REQC), on which this thesis is centered, will be discussed. When describing subsections of the quantum computing scheme, such as qubit creation or detection, it is useful to compare them to general requirements for any quantum computer to work satisfactorily. Such requirements were discussed over several years and finally summarized by David DiVincenzo in 2000 in a very influential paper [28], where he lists what became known as the DiVincenzo criteria. The list consists of five points that are directly related to quantum computing and an additional two that are related to quantum communication. In this chapter I will first go through the parts of our quantum computing scheme in detail, and then summarize it by comparing it to the DiVincenzo criteria. The goal is to be able to highlight especially strong or weak points, and to help plan the direction of future efforts.

5.1 Introduction

The quantum computing field could be said to have been started in 1982 when Feynman first suggested the idea that perhaps the only thing that could ever hope to simulate a system based on quantum mechanical rules, was a quantum computer only limited by the same rules [1]. At the heart of his argument is the fact that a quantum system, based on our current understanding, requires resources that increase exponentially with the size of the problem, in order to be accurately specified on a classical computer. Feynman was considering how to correctly simulate probabilistic systems, and found that perhaps the only way to do that both correctly and accurately, was by using the naturally probabilistic quantum computing, but another example, the best known, is that of Shor's algorithm. In 1994 Peter Shor published a concrete quantum algo-

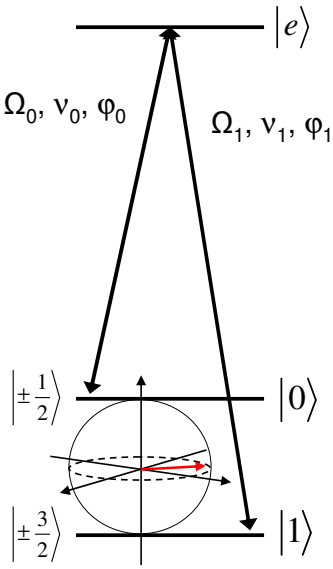

Figure 5.1. *The two ground state levels in Pr^{3+} serve as a qubit, as indicated by the Bloch sphere. Operations on the qubit states are done via the optically excited state.*

rithm for factorizing numbers into their prime components, which use only polynomial resources, compared to the best known classical algorithm that requires resources that increase exponentially with the size of the problem. Even though Grover's algorithm for searching unstructured databases also offers some speed-up compared to its classical counterparts, Shor's factorization algorithm is the only known example for which the actual complexity class of the problem is changed by utilizing the quantum rules. It should be pointed out that it is still unknown whether quantum computers really offer a fundamental speed-up, i.e. is they possess the ability to change the complexity class of a problem, or whether it just happens that no one to date has found sufficiently good classical algorithms. Shor's algorithm however, makes a very strong point in favor of a real fundamental improvement.

It can also be mentioned that the classical algorithms we do have are very good for small systems, and it will probably require a relatively large system before a quantum computer could win out on calculations like factoring, maybe several hundreds of qubits. With today's experimental situation we are very far from this, but long before a full quantum computer is realized, one could perform quantum simulations. A specific quantum simulation could not be used for generic purpose computation, but would rather consist of a controllable quantum system, that behaving in the same way as another, perhaps uncontrollable, system under investigation. Such a quantum simulation system could become useful and better than classical implementations already at a level of a few qubits, and is therefore the type of quantum application that would first become available, much sooner than full quantum computation. In addition, as conventional technology is moving closer and closer to the quantum scale, a general investigation of quantum effects becomes important even for classical systems, and this further motivates the study of few-qubit systems.

5.2 Single qubits

The main idea underlying the implementation of qubits in rare-earth ions was already mentioned in Chapter 3. Due to long coherence times, the best choice of qubit states are two hyperfine levels, as is illustrated by the Bloch sphere in Figure 5.1. In the present work the $|\pm 1/2\rangle$-level in the ground state was chosen to represent the $|0\rangle$-state and $|\pm 3/2\rangle$ to represent the $|1\rangle$ state. One could imagine that operations between the two qubit levels could be carried out with radio frequency fields, coupling the levels directly, but then the advantage of the inhomogeneous broadening in these materials would be lost. RF fields would target all atoms in the field distribution, whereas a laser working on the broadened optical transitions could select a very narrow spectral subpopula-

tion of the atoms. Such a well-defined, spectral subpopulation can be used as a single qubit, with the narrowness ultimately limited by the homogeneous width, which is about 1 kHz for Pr^{3+}. The number of qubit channels that could maximally be created is given by how many that fits into the inhomogeneous distribution, which is $GHz/kHz \approx 10^6$. However, there are several practical elements that limit this further, as will be seen later in this chapter.

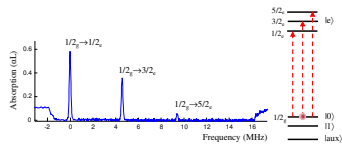

Figure 5.2. *The qubit initialized to the $|0\rangle$-state. The experimental indication of this is the three peaks corresponding to the three possible transitions to the exited state levels form a single ground state level.*

5.2.1 Initialization

For quantum computing, the first step that should be taken, is to initialize the system to a controlled reference state. In our case this can be done with the hole-burning techniques described in Section 3.7, as shown in Figure 3.10, and again in Figure 5.2. In the current scheme, an ensemble of $\sim 10^9$ ions is used as a qubit. This ensemble has about 170 kHz inhomogeneous width, and a variable αL, but for the quantum computing experiments an optical depth of $\alpha L \approx 0.6$ was used. The inhomogeneous width corresponds to an effective coherence time of $T_2^* = 1/\pi 170kHz \approx 2\mu s$. Given that most of the operating pulses have a duration of the same order as T_2^*, using simple pulses would give a significant decoherence. To avoid this, the specially designed *sechyp* pulses have been employed, as discussed in Section 2.5. Due to the nature of the amplitude envelope and frequency chirp of these pulses, all dephasing effects during a pulse transfer is negated, and the typical single pulse transfer efficiency from one ground state to an excited state is about 97 %. In order to perform a real qubit gate operation however, we need pulses that target both of the qubit levels, and can create superposition states, which the sechyp pulses cannot do directly. In Ref. [11], the concept of dark state transfers was introduced, which is the technique that was used for the quantum state tomography experiments in Paper **II**, and will be explained in the following.

5.2.2 Dark state pulses

As a starting point for the explanation of the dark state scheme, Figure 5.1 is used. Two fields will be on at the same time, one resonant with the $|0\rangle \rightarrow |e\rangle$ transitions, with a Rabi frequency of Ω_0, and the other field resonant with the $|1\rangle \rightarrow |e\rangle$, with a Rabi frequency of Ω_1. In order to identify what happens to the states when they are coupled by two fields that are on at the same time we can look at some simple rate equations (see e.g. Scully and Zubairy [29]):

$$\begin{cases} \dot{c_0} &= i\frac{\Omega_0(t)}{2}e^{i\phi_0}c_e \\ \dot{c_1} &= i\frac{\Omega_1(t)}{2}e^{i\phi_1}c_e \\ \dot{c_e} &= i\frac{\Omega_0(t)}{2}e^{i\phi_0}c_0 + i\frac{\Omega_1(t)}{2}e^{i\phi_1}c_1 \end{cases} \tag{5.1}$$

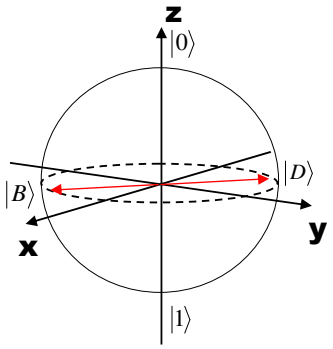

Figure 5.3. *A Bloch sphere on the qubit levels, where the Dark and the Bright state has been inscribed. The exact position of the states in the xy-plane of the sphere is determined by the angle ϕ, which is the phase difference between the two fields, as defined in the text.*

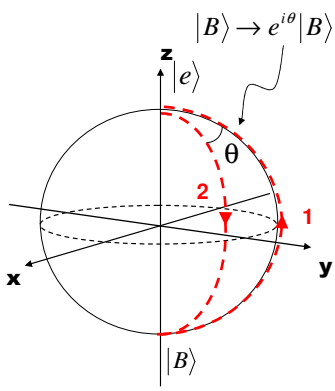

Figure 5.4. *Using dark state transfers as qubit gate operations. The Bright state ions are taken to the excited state and back down along a different path, gaining a phase factor that then corresponds to a rotation in the computational basis. See the text for more information.*

where c_i are the complex amplitude coefficients for each of the three levels involved, and ϕ_i is a phase factor associated with each of the two fields. The two transitions will have different oscillator strengths, but this can be compensated for by tuning the amplitude of each E-field such that the Rabi frequencies for the two transitions are matched, i.e. $\Omega_1 = \Omega_2 = \Omega_R$. We can then rewrite the last line in Equation (5.1) as

$$\dot{c_e} = i\frac{\Omega_R(t)}{2}\left(e^{i\phi_0}c_0 + e^{i\phi_1}c_1\right). \tag{5.2}$$

From this we see that for given values of the two field phases, $\phi_1 - \phi_0 = \phi$, there exist certain states, $c_{0,d}$ and $c_{1,d}$, such that the expression in Equation (5.2) is zero. And the interpretation that the time derivative of the excited state population is zero, is that the light field does not couple to those particular states at all. For that reason, the states $c_{i,d}$ are called dark states. An angle of $\phi = 180°$ away from the dark states, are the bright states, which couple fully to the excited state via the light, and we can change the system description into a new basis defined as

$$\begin{cases} |B\rangle = \frac{1}{\sqrt{2}}\left(|0\rangle - e^{-i\phi}|1\rangle\right) \\ |D\rangle = \frac{1}{\sqrt{2}}\left(|0\rangle + e^{-i\phi}|1\rangle\right) \end{cases} \tag{5.3}$$

where $|B\rangle$ and $|D\rangle$ are the bright and the dark state respectively, for a given phase difference ϕ. As can be seen, these are states on the xy-plane in the qubit Bloch sphere, which is also illustrated in Figure 5.3.

The main idea for using this dark state mechanics to implement qubit gates is outlined in Figure 5.4. Note that the Bloch sphere drawn in this figure does not have the same poles as previous spheres. The north pole is the electronically excited state, while the south pole is the bright state, $|B\rangle$, since this is a representation of the ions that do interact with the light. For the rest of the discussion, a dark state pulse, also sometimes referred to as a two-color pulse, is a pulse that contains both field components (ν_1 and ν_2 in Figure 5.1), i.e. a pulse that contains two colors. It should also be kept in mind that the shape of each field component is still that of a sechyp, to compensate for the dephasing due to inhomogeneous broadening. First, a dark state pulse is sent in with a certain phase relation between the two fields, $\phi = \phi_1 - \phi_0$. This is the upgoing path in Figure 5.4 designated '1', which will excite all atoms from the bright state to the excited state. Next, a second dark state pulse is sent in, again with the same ϕ, but this time with an added overall phase factor of $\theta + \pi$. The effect of the second two-color pulse is that the excited atoms will be deexcited again, back down to the bright state, but along a different path, marked '2'. As seen in the figure, the paths will be separated by an angle, θ, and the net action on the bright state by this combined operation

is an acquired phase shift, $|B\rangle \rightarrow e^{i\theta}|B\rangle$. The extra π in the overall phase factor mentioned above can be explained as follows: Without any extra angle at all added, the second dark state pulse would just continue the Rabi flopping on the $|B\rangle \rightarrow |e\rangle$ transition started by the first pulse, going down on the Bloch sphere surface along a path opposite to where it came up. With only an angle of π added, it will then instead go down exactly the same way as it came up, and thus, now with $\theta + \pi$ added, it will go down along a path shifted exactly by an angle of θ compared to where it went up. It is important that the relative phase between the two fields of each pulse, ϕ, is kept constant for both pulses, since ϕ determines the dark/bright state basis, and thus, which states are targeted by the operation.

We now know that the action of such a pulse sequence in the dark state basis is $|B\rangle \rightarrow e^{i\theta}|B\rangle$. After a straightforward basis change, we can see that in the computational basis ($|0\rangle$, $|1\rangle$), this operation corresponds to

$$U_{dark} = e^{i\theta/2} \begin{bmatrix} \cos(\theta/2) & ie^{i\phi}\sin(\theta/2) \\ ie^{-i\phi}\sin(\theta/2) & \cos(\theta/2) \end{bmatrix}. \tag{5.4}$$

As it turns out, the above matrix is a unitary operation that performs a rotation by an angle θ, around any vector on the equator plane of the qubit Bloch sphere, specified by ϕ. It is also true, that by such rotations alone, repeated if necessary, one can execute any arbitrary single qubit gate operation, which was our goal. As an example, if both θ and ϕ are set to π, a NOT gate is obtained.

It may also be said that as the bright state is being transferred to the excited state, the ions will pick up an additional phase factor due to the optical inhomogeneous broadening. This can be understood by noting that the bright state is a superposition in the computational basis and transferring this to the excited state, will create a general superposition containing the $|0\rangle$, $|1\rangle$ and $|e\rangle$-states. Such a superposition based on an ensemble of ions with different detunings, will pick up a phase factor that increases with the time spent in the excited state. This phase factor however, can be compensated for, since in general, a phase factor is irrelevant if it appears in front of all terms. And by performing a dark state operation on the *dark state*, with $\theta = 0$, i.e. where path '2' in Figure 5.4 just retraces path '1', we can get the rest of the state wave function to pick up exactly the same phase, which can then be disregarded.

5.2.3 Optimal control theory pulses

Introduction

Even though single qubit gate operations were realized with good efficiency (see Section 5.3.1) using the dark state approach de-

scribed above, the total pulse sequence needed to perform the gate operation takes some time. Two dark state pulses are needed to infer the θ-angle on the bright states, and an additional two pulses are needed to compensate for the detuning-based phase shift on the dark states. Each two-color pulse was in our experiments 4.4 µs long. This time is set by requirements on the sechyp shape to maintain an adiabatic action on the ions during the transfer, and cannot easily be reduced for a given peak width. Four pulses times 4.4 µs is almost 18 µs in total, which will contribute to decoherence from the optical dephasing and maybe from inhomogeneous hyperfine broadening. One way to reduce this gate time is to use other pulses with other shapes than a sechyp, to compensate for the optical inhomogeneity. Then the concept of optimal control theory is a promising route.

The basic concept of optimal control theory is to minimize a cost function determined by the physical system, given a set of experimental constraints. In our case we are interested in performing qubit gate operations, so the physical system includes the ion and all its relevant levels, the light field of the laser, and all equations that describe the interaction between these. Our goal is to find a new pulse shape that performs the desired gate operations with as high fidelity as possible, and in as short a duration as possible. Given this goal, there are also additional constraints set by our experimental equipment. The bandwidth, i.e. the maximum chirp rate, is limited in our AOMs that produce the pulses, and must to be taken into account. Similarly, the laser intensity is limited and can also fluctuate with time. The pulses should therefore be robust to changes in the Rabi frequency, i.e. they should give a high fidelity within a certain range, say $\pm 10\%$ of the optimum Rabi frequency. It should also be mentioned that pulses designed by optimal control theory have recently been implemented in other systems (ion-traps), in order to demonstrate such robustness [30].

Implementation

As the task of minimizing the complicated cost function can be quite demanding, it is natural to try to do it numerically on a computer. This was also done in our case by a theoretical group in Munich, who are specialized in this area. After discussing how to implement the physical system and the constraints, they were able to obtain several new pulses for different objectives. As has been said, the end goal is to obtain single pulse qubit gates, but even though at the time of writing this has not yet been achieved, we have gained some partial results that will be discussed in this section. A full gate would require the optimal control pulse to interact with at least three levels, the two qubit levels and one excited state. As it turned out, this is more difficult than creating a pulse which interacts only with two levels, one ground state

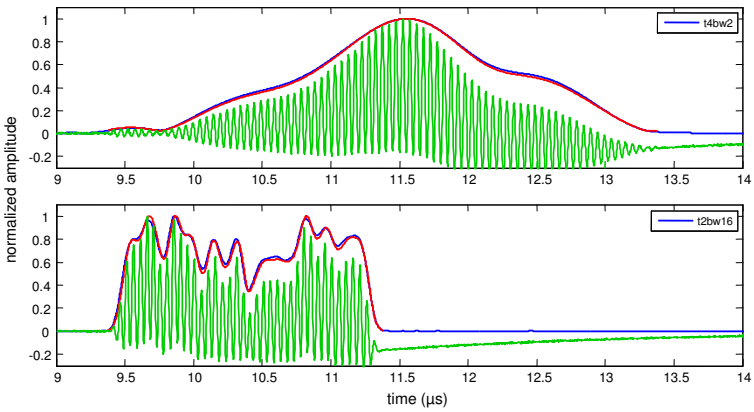

Figure 5.5. *Amplitude shape of two optimal control transfer pulses with different bandwidth. Red line is the theoretically desired shape, blue line is the experimentally detected shape. The green line shows the beating pattern that was used to measure the pulse.*

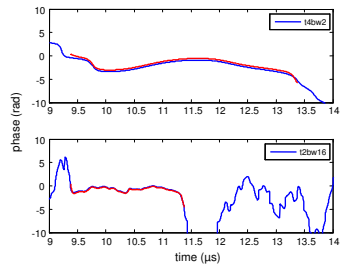

Figure 5.6. *The phase of the same optimal control pulses as in Figure 5.5. Again, the red line is the theoretically desired phase chirp, and blue shows the experimentally verified phase chirp. Note that the phase values outside the actual pulse (outside the red parts) does not have any meaning, but are arbitrary.*

hyperfine level, and one excited state level. Therefore, to test whether the system has been implemented correctly, it is good to start with an optimal control pulse designed to simply transfer the population from one ground state to one excited state. Examples of such pulses are displayed in Figure 5.5, where the amplitude is shown, and in Figure 5.6, where the corresponding phase chirp is shown. In both of these figures, the red line marks the theoretically desired shapes.

To verify that these pulses could be implemented correctly by the AOMs and the calibration system, an interference experiment was setup to detect the exact shapes of the generated pulses. In each test, the optimal control pulse was overlapped with a reference beam that was shifted 20 MHz, and the resulting beating was used to obtain information about both the amplitude and the phase content of the pulses. The beating was analyzed using a method by which the signal is Fourier transformed, and in the Fourier plane all negative values are removed, and then transformed back. The result is a complex signal of the form $A(t)e^{i\phi(t)}$, where the amplitude of the original signal, $A(t)$, and the phase of the beating $\phi(t)$, can be obtained in a direct manner. The beating itself is shown in Figure 5.5 in green, and the resulting amplitude and phase of the experimental optimal control pulse are shown in blue in Figures 5.5 and 5.6, respectively. The difference between the two pulses displayed is the bandwidth, which is 2 and 16 MHz respectively. For the higher bandwidth pulse it was possible to obtain a shorter duration, keeping the same theoretical transfer efficiency. All in all, five optimal control pulses, designed for the

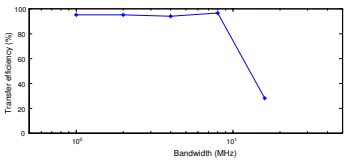

Figure 5.7. *Efficiency of a transfer from $|\pm 1/2g\rangle$ to $|\pm 3/2e\rangle$, using optimal control pulses of different maximally allowed bandwidths.*

same purpose (two-level population transfer), with similar theoretical efficiencies, but using different maximally allowed bandwidths, were created. The bandwidths used were 1, 2, 4, 8 and 16 MHz, and the pulses had a corresponding duration of 8, 4, 2, 2 and 2 µs, respectively. When applied experimentally to a peak of ions, all pulses, except the one with a bandwidth of 16 MHz, achieved the expected high transfer efficiency (of about 95%), as plotted in Figure 5.7.

The reason why the high bandwidth pulse failed is still not entirely clear, but is at this point believed to be related to the involvement of other levels. In the experiment, $|\pm 3/2\rangle$ was used as the excited state, and one can note the closest other level is $|\pm 1/2\rangle$, which is 4.6 MHz away (cf. Figure 3.3). Thus, as long as the bandwidth of the pulse is lower than $\sim 2 \cdot 4.6 = 9.2$ MHz, the pulse interacts only with the two levels involved in the transfer. We see that the 16 MHz pulse has a larger bandwidth than this, and will in fact interact with all three excited hyperfine states, which creates a much more complicated situation than when only two levels are involved. This can also bee seen by the shapes of the pulse, as the pulses of bandwidth 1 through 8 MHz all have a very similar shape, with a clear peak around the center, like the upper one in Figure 5.5. The 16 MHz bandwidth one however, looks completely different, with several sub-peaks, illustrating a more complicated behavior. The exact appearance of it cannot in general be intuitively explained, because of the nature of the optimal control algorithm, and in fact the solutions obtained are not necessarily unique or even at the global maximum. Another explanation of the poor efficiency of the 16 MHz pulse that was explored was whether the double pass AOM had problems to generate the high bandwidth, but this is not believed to be the main problem. As mentioned above, the final goal of full qubit pulses has, as yet not been achieved. Since these would necessarily also involve more than two levels, it is possible that the failure of these is related to that of the high bandwidth, therefore this is an issue that will require a continuing effort in the future.

5.3 Detection and characterization

For all qubit experiments, the detection was done by absorption measurement, although the use of fluorescence techniques is also a possibility. The advantage of fluorescence is that the background signal can be made very low, which in general makes a very high sensitivity possible. On the other hand fluorescence occurs without a specific direction, so the spatial collection efficiency will be one limitation. Another problem is that the qubit ions have very long lifetimes (one of the major reasons why we use them in the first place) which in turn means slow readouts. With absorption

measurement, the readout can be scanned very fast, as discussed in Section 2.6, but with a straightforward measurement, the background light is often very high, giving poor a signal-to-noise ratio (SNR) when low absorptions are being detected. However, several experimental techniques have been demonstrated by others to improve the SNR, such as frequency modulation spectroscopy [31] or by removing the background by staying on a dark fringe in an interferometer, as described recently in [32]. In principle however, any refinement technique used should be easily combinable with the fast chirp readout method, in order not to lose this advantage.

What has been described so far is pure population detection, which corresponds to measuring the z-axis on the qubit Bloch sphere. To measure along the other axes there are a few possibilities. One could, for example, use phase-sensitive methods, such as heterodyne detection of the free induction decay or Raman heterodyne detection, as in [20]. In our qubit experiments however, we have chosen to simply perform additional operations, rotating the whole Bloch sphere such that the x- and y-axis turn into the z-axis, and then perform a population measurement. In the following, the sequence of pulses used to completely characterize the qubit will be described.

5.3.1 Quantum state tomography

A qubit can be conveniently described using the Bloch sphere, which suggests that if one has a qubit in an arbitrary state, i.e. with a vector pointing in an arbitrary direction, it can be completely described by measuring the projection of the state onto the three principal axes. Furthermore, from Chapter 2 we know that the density matrix is another good way of representing the state of a qubit. The density matrix of a qubit can be obtained by the use of (see e.g. [33])

$$\rho = \frac{\mathrm{tr}(\rho)I + \mathrm{tr}(X\rho)X + \mathrm{tr}(Y\rho)Y + \mathrm{tr}(Z\rho)Z}{2}, \qquad (5.5)$$

where X, Y and Z correspond to the Pauli matrices, which together with the identity, I, span the 2×2 qubit space. The above equation is useful because the traces correspond to actual physical measurements. For example, $\mathrm{tr}(Z\rho)$ means measuring the projection of the unknown state onto the Z axis, which will yield a value between -1 and +1, and the same for the other axes. Of course, for implementations where the qubit consists of single quantum states, one can only get a value of either +1 OR -1, upon measurement. One then needs many copies of the same state, or must redo the experiment many times, in order to build up enough statistics to get a more accurate number for the real value. For the ensemble approach that we used, the statistics are obtained from a single measurement, since we in principle have $\sim 10^9$ single qubits

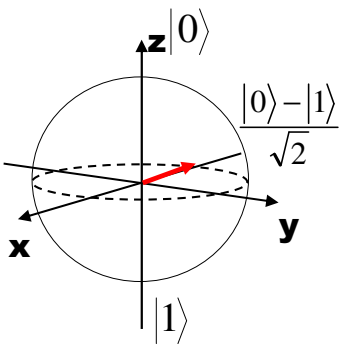

Figure 5.8. *Bloch sphere showing the* $\frac{1}{2}(|0\rangle - |1\rangle)$ *state, as is used in the example in the text.*

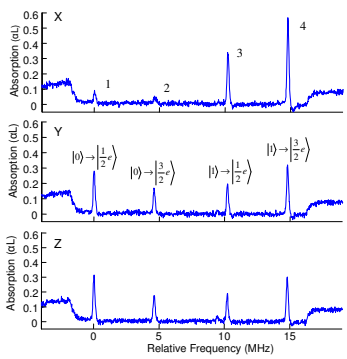

Figure 5.9. *The three different projection measurements included in the quantum state tomography sequence of the state displayed in Figure 5.8. The four main peaks correspond to the qubit states' transitions to the two strongest excited states, as indicated in the Y-measurement figure.*

working in parallel during the experiment. The advantage of this approach is a much stronger and faster readout signal, since one does not have to worry about single ion detection. The major drawback of ensembles is poor scaling for many qubits, which will be discussed later. In addition, there are some techniques that can improve the estimation of the density matrix from experimental results, such as the Maximum Likelihood Method, which are unavailable in an ensemble approach.

As mentioned above, with a simple absorption measurement we can really only measure the population, i.e. the z-axis. To measure, for example, the projection onto the x-axis, we then employ the dark state pulses to rotate the unknown state such that after the rotation, a z-measurement gives the same information as an x-measurement would have done before the rotation, i.e. the state is effectively rotated by 90°. To concretize the ideas of qubit gates with dark state pulses and characterization with quantum state tomography, an example with a particular state, is described below.

Example: Tomography of $(|0\rangle - |1\rangle)\sqrt{2}$

Starting from a situation in which all atoms are initialized to the $|1/2g\rangle$ level, i.e. the $|0\rangle$ state, we first need to apply a dark state operation to create the desired superposition state. With our definition of the Bloch sphere, the starting state $|0\rangle$ is characterized by a vector pointing north, i.e. $z = 1$. The desired state, $(|0\rangle - |1\rangle)/\sqrt{2}$, is then given by a vector pointing in the direction of the negative x-axis, and we understand that to create this state, we need to perform a 90° rotation around the negative y-axis (or alternatively, a -90° rotation around the positive y-axis). This can be accomplished by setting $\phi_{bright} = 90°$ and $\theta_{bright} = -90°$ in Equation (5.4), which gives an appropriate rotation matrix[1]. This creates the state, but all bright state ions have now in addition acquired a detuning-dependent phase shift, and we compensate for this, as mentioned above, by performing an identity operation on what was earlier the dark state ions. Recalling that ϕ determines the rotation axis and θ the rotation angle, this can be done by putting $\phi_{dark} = \phi_{bright} + 180°$, with $\theta_{dark} = 0°$.

The state has now been created and we can characterize it using the quantum state tomography described. For this, the full experiment is repeated three times, one for each axis to be measured. Z-measurement is trivial, being given by a direct absorption measurement. To measure the x-projection, we need to first make a 90° rotation around the negative y-axis, since this operation will rotate the x-axis onto the z-axis. Similarly, before the y-measurement, a

[1] for additional motivation regarding the relation between the angles and the matrix representation see e.g. section 4.2 in Nielsen and Chuang [5]

90° rotation around the positive x-axis is performed. The three resulting absorption measurements are displayed in Figure 5.9. From this figure, the traces from Equation (5.5), needed to calculate the density matrix of the state, can be obtained. Since the y-axis in the figures is αL , which is directly proportional to the number of absorbing ions, the number of ions in each qubit state can be obtained by numerically calculating the area under the peaks. Each peak area then has to be divided by the oscillator strength for that corresponding transition in order to compensate for different transition strengths. The traces can then be obtained from

$$\mathrm{tr}(Z\rho) = \frac{(\mathrm{Z_{AREA}})_{|0\rangle\rightarrow|1/2e\rangle} - (\mathrm{Z_{AREA}})_{|1\rangle\rightarrow|1/2e\rangle}}{(\mathrm{Z_{AREA}})_{|0\rangle\rightarrow|1/2e\rangle} + (\mathrm{Z_{AREA}})_{|1\rangle\rightarrow|1/2e\rangle}}, \tag{5.6}$$

and similarly for the other measurements. Note that it is possible to obtain a second set of traces from using the transitions to the $|3/2e\rangle$-state from both qubit states. This can be used to reduce errors, and to gain information about ions left in the excited state as a residue from the dark state transfers. Analysis has shown however, that there does not appear to be any significant population left in the excited state. It can also be noted that the $\mathrm{tr}(\rho)I$ part of Equation (5.5) has a normalizing meaning, in the sense that for a pure state where no atoms have decayed to states that are not measured, this term will simply be the identity matrix. In our experiments we have used the fact that we know that the lifetime of the hyperfine states is very long compared to the experiment time, together with the fact that the branching ratio to the auxiliary state (the only state not measured) is very low, in order to be able to assume that there is no non-measured decay. We now have access to all the information needed to create the density matrix. For the particular state in this example, corresponding to the measurements shown in Figure 5.9, we get

$$\rho_{exp} = \begin{bmatrix} 0.49 & -0.37 - 0.04i \\ -0.37 - 0.04i & 0.51 \end{bmatrix}. \tag{5.7}$$

The fidelity for the experiment can then be defined as

$$F_{tot} = \langle \psi_{theor} | \rho_{exp} | \psi_{theor} \rangle . \tag{5.8}$$

Here, $|\psi_{theor}\rangle = (|0\rangle - |1\rangle)/\sqrt{2}$, and the fidelity can be easily calculated in our example to be $F_{tot} = 0.87$. This is the total fidelity for the experiment, including two gates, one to create the state, and one for readout. Another interesting value is the fidelity for a single gate, which is obtained as $F_{gate} = \sqrt{F_{tot}} = 0.93$, in this example. Other states were prepared and analyzed in a similar fashion in Paper **II**, and all gate fidelities were found to be above 90%, which is a very good result. A visualization of the states analyzed in the paper is given in Figure 5.10, where all measured

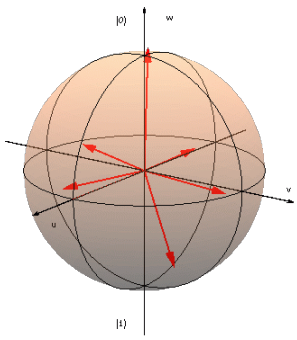

Figure 5.10. *Quantum state tomography was performed to characterize six created states (along the axes). The experimentally obtained density matrices were used to produce the state vectors inside the Bloch sphere.*

a) XOR

C	T	Result
0	0	0
0	1	1
1	0	1
1	1	0

b) CNOT

$$\begin{array}{c} \\ |00\rangle \\ |01\rangle \\ |10\rangle \\ |11\rangle \end{array} \begin{array}{c} \begin{array}{cccc} |00\rangle & |01\rangle & |10\rangle & |11\rangle \end{array} \\ \begin{bmatrix} 1 & 0 & 0 & 0 \\ 0 & 1 & 0 & 0 \\ 0 & 0 & 0 & 1 \\ 0 & 0 & 1 & 0 \end{bmatrix} \end{array}$$

Figure 5.11. *The truth table of a classical XOR gate shown in* ***a)****, while the matrix representation of a quantum CNOT is showed in* ***b)****.*

states have been inscribed into the Bloch sphere. There are six states in total, corresponding to the desired states which are located along both the positive and negative direction of each of the three axes.

5.4 Two-qubit investigations

One of the end goals for the ensemble approach to quantum computing has been to achieve a two qubit gate, such as the Controlled-NOT (CNOT). This has unfortunately not yet been achieved, but some partial results have been obtained, and some considerations regarding future efforts will be discussed here. The classical version of the CNOT is called exclusive-OR (XOR) and has a truth table which is given in Figure 5.11**a**. The CNOT is important since it is a part of a set of gates that constitutes a universal quantum computer, i.e. having access only to those gates, one can implement any quantum algorithm. The operation matrix formulation of the CNOT is given in Figure 5.11**b**, and even though one usually refers to one of the qubits as *control* and the other one as *target*, one can note that this gate is symmetric with regards to the qubits. In this section I will first present the general idea for qubit-qubit interactions in our scheme, followed by a description of how to carry out the CNOT protocol, concluding with discussions on the current experimental situation.

5.4.1 Creating entanglement

The mechanism for creating qubit entanglement in rare-earth crystals is dipole-dipole interaction between near-lying ions, illustrated in Figure 5.12. Two ions are shown each belonging to different qubit ensembles, with different resonance frequencies. The Pr^{3+} ions have a permanent dipole moment, but its value changes depending on the state it is in. Thus, if one of the ions, say the one designated control ion, is excited, with the associated change in dipole field, the other ion has its level structure rearranged slightly through the Stark effect. This causes the second ion to get out of resonance with a potential target ion operation pulse, which constitutes a good way of producing conditional operations.

Figure 5.12 illustrates the principle for the physical interaction between single ions, but in a large crystal where $\sim 10^9$ ions are used for each qubit, it is also necessary to have a protocol that can select the ions that are close enough to experience the interaction. The induced Stark shift decreases as the cube of the distance between the ions. The frequency shift must be large enough to move the ions clearly away from the gate pulse frequencies, i.e. in the order of 1 MHz, and, as mentioned in Section 3.6, this suggests that the ions should be within $\sim$ 10 nm from each other. This is only true for a fraction, of the order of 1%, of all the ions in the original

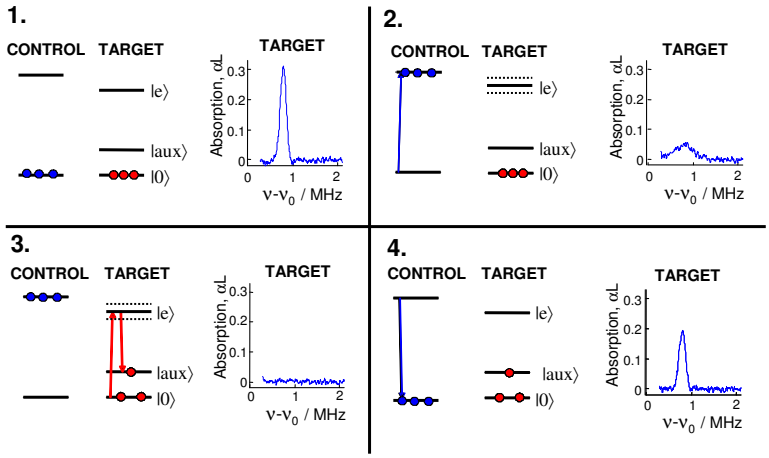

Figure 5.13. *The idea behind the distillation, namely, selecting only those ions that are close enough to be strongly interacting. First, a target and a control region are chosen, then the control region is excited which causes all target ions to shift their resonance by an amount given by their distance from the nearest control ion. In frame 3), all ions still visible in frame 2), i.e. those that did no shift sufficiently, have been pumped away to the $|aux\rangle$ state. Finally, in frame 4), the control ions have been taken back down to the ground state, and the ions that shifted away will return to their previous frequencies. Experimental figures taken from Ref. [34].*

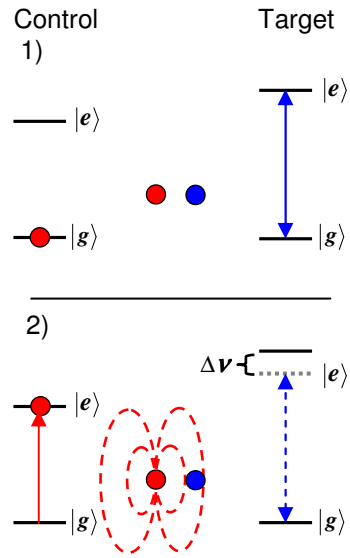

Figure 5.12. *Two near-lying ions with different resonance frequencies are selected. With the control ion still in the ground state, the target ion can be involved in operations, using a frequency ν_{ge}. In part 2), the control ion is excited and due to the Stark shift from the changed dipole moment, the target ion is no longer accessible as frequency ν_{ge}.*

qubit. To find those ions, a distillation scheme was put forward and demonstrated [34]. The main idea behind the scheme is illustrated in Figure 5.13, and is described in the caption to this figure. First, the control ions are excited, which allows all non-interacting target ions to be removed. After that however, the reverse procedure must be applied; the remaining target ions must be excited such that the control ions can be distilled in the same way.

5.4.2 CNOT scheme

In words, the action of the CNOT gate should be the following: If the control qubit is in the $|0\rangle$-state, nothing should happen to the target, but if the control qubit is in the $|1\rangle$-state, a NOT operation should be applied to the target qubit. And, since this is a quantum gate, if the control qubit is in a superposition, e.g. $(|0\rangle + |1\rangle)/\sqrt{2}$, the target qubit will also end up in a superposition, in fact, the two qubits will then become entangled. Note that in the ensemble approach, this entanglement occurs pairwise between the single ions, and upon readout, the average state will be probed. The full density matrix of the state can then be obtained in the same manner as for single qubits, by applying appropriate rotations before

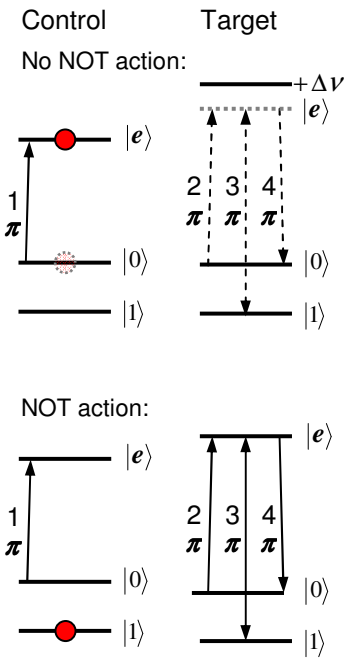

Figure 5.14. *Illustration of the REQC CNOT scheme. In the upper part, the control qubit is in the $|0\rangle$-state, which means that the control ions will become excited. This will cause a shift on the target ions, and all subsequent target pulses will not be resonant. In the lower part, the control qubit is in the $|1\rangle$-state, and will thus not be excited, which causes the NOT operation to be carried out on the target qubit.*

the readout.

Figure 5.14 illustrates the two cases of the CNOT where either the control qubit is in the $|0\rangle$-state (upper part), or in the $|1\rangle$-state (lower part). Here again, the advantage of using frequency as the means for selecting the different qubits becomes clear. The qubits can have any state on the qubit levels, and the optical transition acts as a way of switching on or shutting off the interaction between the qubits.

5.4.3 Current status

Some introductory ion-ion control experiments were done in 2005 [34], in which a narrow qubit peak was shifted by a broad range of control ions, i.e. an asymmetric action. A typical qubit peak is about 200 kHz, whereas the control intervals used in the article were up to 20 MHz, which shifted approximately half of the ions enough to be useful. A real CNOT gate should, as mentioned, be symmetric, meaning that the control interval should be a peak with the same width as the target qubit. This will decrease the control interval, and thus the number of ions, by a factor of 100, resulting in only $\sim 0.5\%$ of the ions being shifted enough to be useful. There are also other considerations when switching from simply an interval on the inhomogeneous absorption line to a prepared peak, namely that without any preparation, one frequency point on the absorption line consists of contributions from all the nine possible transitions, while a peak is only a single transition, causing a loss of a factor of 9. However, before the ion class chosen for the peak has gone through the preparation, it can be in any of the three ground states. The preparation can move ions in the other two states into the chosen state, effectively increasing the number of ions by a factor of 3, thus mitigating the loss somewhat. In total, moving to a symmetric control situation will cause the number of interacting ions to drop to $\sim 0.1\%$.

Naïvely, one might think that only the total number of ions we are left with in the end matters, i.e. that one could compensate a poor interaction probability by starting with more ions or using a more sophisticated detection system. This is not true however, as shown in Ref. [21], as the off-resonant excitations from the ions outside the pit contribute a non-negligible amount. For typical values of pit width and ion homogeneous width, one can expect the off-resonant absorption also to be of the order of $\sim 0.1\%$ of the original absorption, thus making detection of any qubit ions below this limit very difficult. The only reasonable way to get more interacting ions is to increase the interaction probability, which can be done either by increasing the concentration of doped ions, to reduce the average ion-ion distance, or by moving to another ion species that has a larger permanent dipole moment. The latter option however, will also require the pit + peak preparation se-

quences to be reworked, which makes it less feasible. Regarding increased ion concentration, this is probably best combined with working at the edge of the inhomogeneous absorption profile. The reason for this is that the main mechanism for a Pr^{3+} ion to end up at the edge of the profile is that it has a close proximity to another Pr^{3+} ion, which thus should also increase the probability for interaction with the selected qubit ions. A more radical approach would be to utilize so called satellite lines. These are absorption lines, outside the main profile, which originate from pair sites, i.e. in situations where two Pr^{3+} ions have replaced two Y^{3+} ions in directly connecting sites in the crystal lattice. These Pr^{3+} ions will experience a strong local shift, which makes them appear as narrow lines far away from the normal transition frequency. There is only a small chance for any Pr^{3+} ion to end up in a pair site, but this chance grows as the square of the ion concentration [35], and, more importantly for this discussion, any ion found in such a site has a very high probability of being involved in a potential qubit interaction.

5.5 Scaling and outlook

5.5.1 Ensemble approach

One of the major difficulties connected with the ensemble approach to rare-earth quantum computing is the scaling towards many qubits. As discussed in the previous section, it is not trivial even to find sufficiently many interacting ions for two qubits. With a constant probability p for an ion to be found near another one, the probability for n ions to be close enough for interaction scales as $p_n = p^n$, which decreases rapidly since p is often of the order of $0.1 - 1\%$.

One way to improve the scaling for the ensemble approach would be to use a bus qubit, which was analyzed in Ref. [36]. With this idea, a special qubit is used as a bus to mediate the interaction between the other qubits, which do not have to be close enough to each other, but only to the bus qubit. This increases the allowed distance from each other and thus improves p. It was also shown that if this method was combined with a very highly doped material, such as stoichiometric crystals [37], the the probability of finding a quantum computing instance of size n would approach the linear regime, instead of the exponential as stated above. Working with such highly doped materials however, introduces new difficulties connected with the higher absorption, including increased off-resonant interactions and a more strongly propagation-direction-dependent intensity. Further, more highly doped crystals also often have shorter coherence times.

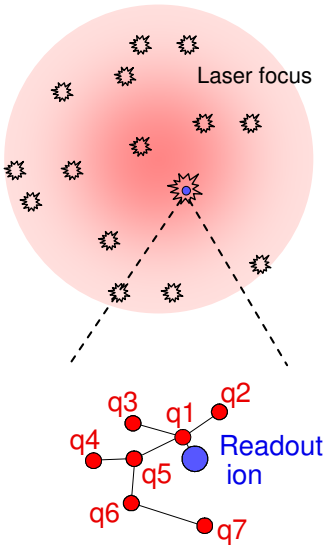

Figure 5.15. *A laser focus containing multiple instances corresponding to multiple readout ion frequencies are shown. A single instance is magnified showing the readout ion detecting a cluster of 7 qubits.*

5.5.2 Single instance approach

The most realistic way of scaling a REQC to at least a medium number of qubits, is to move away from the ensemble approach to a single ion implementation. We would then only have to find a single instance where n ions happened to be close enough, which of course has a much higher probability. An additional advantage is that all ions that are sufficiently close can be used, regardless of frequency, in contrast to the ensemble approach where the qubit frequency is chosen first, and interacting ions only determined secondly. The major challenge with the single instance approach is the detection system. For rare-earth ions used as qubits, a combination of long lifetimes and trapping in other hyperfine states, makes single ion detection very difficult. Instead, it has been proposed [36] to co-dope the qubit ion crystal with another ion type with different characteristics in order to achieve the readout. Such a readout ion would sit close to a cluster of qubit ions, similar to the bus ion, but without having to be coherent. The qubits would communicate quantum mechanically between each other through nearest neighbor interaction, which has been shown only to add a polynomial amount of steps, but would need to communicate with the readout ion only classically, i.e. the readout ion only needs to be sensitive to the state and not to the phase. This can be accomplished by the same dipole blockade mechanism that is used to implement the qubit gating interaction. Without the strict coherence-time demands on the readout ion, ions with short lifetimes can be used, which means fast cycling and thus that they are much easier to detect in single instances. A readout ion controlling a set of 7 qubits in a single instance is illustrated in Figure 5.15.

So far, the most promising candidate as a readout ion is cerium^{3+}, which has undergone some introductory investigations. For the purpose of getting a strong response it is important that the transition can occur without any phonon interaction, and such a zero-phonon line was recently measured by us in Ce to have a linewidth of about 3 MHz with a lifetime of about 50 ns. This should be fast enough to enable single ion detection, provided there are no trapping states that could stop the cycling, which must be investigated further. It is believed that this type of implementation could yield of the order of 10 qubits. For scaling to arbitrarily large systems, the most likely implementation is through flying qubits. The would be accomplished, for example, by interference between photons coming from different instances, either through free space or inside mode-matching structures such as fibers or cavities, as suggested in for instance in [38].

5.6 DiVincenzo criteria

As stated in the introduction, this chapter will now be summarized by discussing the current and future experimental status, by commenting on the REQC scheme from the perspective of the DiVincenzo criteria. I will try to keep the discussion to those aspects that have in some way been investigated experimentally, since most of the ideas still at a theoretical stage tend to have overlooked some of the experimental difficulties.

1) A scalable physical system with well characterized qubits

This is the most fundamental requirement for any quantum computer, and it is also the most difficult one. Any quantum computing (QC) scheme must start with a definition of what the qubit for that scheme would be, and in our case the qubits can be very well distinguished through their optical resonance frequencies. So, the latter part of the criteria is fulfilled well, but on the other hand there is no QC scheme to date which has demonstrated a truly scalable qubit implementation, and nor have we. The main complication is getting all qubits to interact with each other without losing the phase information. Since space consists of only three dimensions I can not think of any way to position physical qubits in such a way that any qubit can always coherently interact directly with all other qubits in the register. This leaves only the use of a special bus, similar to classical computers, that can be used to communicate between the qubits, as mentioned for our single instance approach. A photon is most often considered for this type of mediator, since it interacts only weakly with the environment and can thus travel long distances without losing its information. For the same reason however, it is also difficult to achieve single photon/single qubit interfaces. Much research has been done on these types of interfaces, including the promising method of using cavities to boost the interaction probability of the photon. I think at the point when these interfaces become of sufficiently high quality, the scaling of many different QC schemes would be improved dramatically, including our own approach.
Current REQC status: Partially fulfilled, well characterized qubits, but not yet fully scalable.

2) The ability to initialize the state of the qubits to a simple reference state such as $|000..\rangle$

This is one of the most important differences between the REQC scheme and that of NMR (nuclear magnetic resonance) quantum computing, which also uses ensembles. In NMR, the initialization becomes increasingly difficult the larger the system is. In our ap-

proach, there is only a constant number of operations required to prepare each qubit in the $|0\rangle$ state. This is very good, but some considerations still remain. Quantum error correction has not been discussed much, since it in general requires many qubits to be implemented, but since we are now looking at future scaling of this protocol, some comments are in order. It can be shown (mentioned e.g. in [5]), that in order for error correction to successfully make a quantum computer fault tolerant, a continuous supply of ancilla qubits prepared in the $|0\rangle$ state is needed. If these temporary ancilla qubits are needed during the computation, it implies that the initialization procedure needs to be fast compared to the coherence time, i.e. it must be of the same order as the quantum gate time. In our current implementation, emptying a pit requires optical pumping procedures, which involves waiting several lifetimes for ions to decay to certain states. Even though it can be done with a constant number of operations, it does take longer than the gate time. This has not been a problem so far, since we are not in the many-qubits regime, but there is certainly motivation for developing the initialization procedure further.
Current REQC status: Good, but room for improvement.

3) Long relevant coherence times, much longer than the gate operation time

For REQC there are two relevant coherence times, the hyperfine coherence time which is important for storing the qubits, and the optical coherence time, which becomes important during operations. Currently, the operation time is of the order of 1-10 µs, whereas a hyperfine coherence time close to a second has been measured with magnetic fields and up to 30 seconds with dynamic decoupling sequences, as described in Section 3.5. This gives an impressive ratio of the number of gates per coherence time of the order of 10^6. However, the optical coherence time will limit this further, since it is of the order of 100 µs. This will decrease further through excitation-induced broadening, once ions start getting excited, and will give a gate/T_2 ratio of 10-100 instead. It should be said however, that in a future multiple qubit quantum processor, not all qubits will be operated on at all times. This will allow qubits to stay longer in the hyperfine states, and thus benefit more from the longer coherence time, pushing the gate/T_2 ratio beyond the limitations of the optical transition. In addition, given the multitude of methods to improve various aspects of dephasing, including the dynamic decoupling sequence, the sechyp shapes to counter inhomogeneous dephasing as well as subradiant states/lifetime increases by using cavities to modify the radiation properties, there are many possibilities to improve this.
Current REQC status: Good, but additional thoughts on the optical coherence would be helpful.

4) A universal set of quantum gates

The set of gates known as the *standard set* of universal gates is the Hadamard, phase, $\pi/8$ and CNOT gates, which will allow the implementation of any quantum algorithms. It was an important milestone for REQC to demonstrate the arbitrary single qubit rotations on the hyperfine levels in Paper **II**, since with this, three out of these four gates were demonstrated. Unfortunately, the remaining gate, the CNOT, is the most difficult one, since it requires more than one qubit, and the issues connected with implementing it were already discussed in detail in Section 5.4.3.
Current REQC status: Partially fulfilled, all single qubit gates done, but not yet a two-qubit gate.

5) A qubit specific measurement capability

So far while discussing the criteria, no distinction between the ensemble approach and the single instance one has been made, because the qubit selection or the way operations are performed are identical for the two approaches. But the major change for single instances is the detection of single ions, which is much more difficult than detecting an ensemble of 10^9 ions. In the ensemble approach each qubit can be detected in exactly the same way as it is controlled, through frequency-resolved techniques, implying that this criterium is well fulfilled. However, in the single instance approach, the long-lived qubits cannot be individually detected, but a single readout ion is meant to supply the readout capability for a cluster of qubit ions. This clearly increases the level of difficulty when it comes to qubit-specific detection, and while the theoretical suggestions are feasible, no experimental verification has as yet been presented.
Current REQC status: Fulfilled for ensembles, but not yet for single instances.

Chapter 6

Quantum memories

The need for long distance quantum communication networks is growing rapidly, as demonstrated in particular by quantum cryptography which has already made its way into commercial products. The ability to reliably transfer single quantum states is one of the major bottlenecks for these system at the moment, and therefore the improvement of long distance quantum communication is a high priority in order to advance the field. At the heart of the problem are the natural losses in the fiber, which, even though they are small, together with the need to send single photons, eventually lead to the loss of the signal.

Transmission of photons through fibers is accompanied by some attenuation, which typically may be in the order of $a = 0.2$ dB/km at telecommunication wavelengths. This means that the probability of successfully sending a single photon through a fiber of length L is given by $P(L) = 10^{-aL/10}$. Even though the loss is initially very small, the signal strength decreases exponentially with distance and, while it is 63% at a distance of 10 km, it has dropped to only 1% at 100 km and 10^{-10} at 500 km.

In the theory of quantum error correction (see e.g. [5]), it can be shown that there are fault-tolerant quantum computing schemes that can be used to reduce the error of any operation, by encoding single qubits of information onto larger sets of physical qubits. This can also be directly applied to communication, since transmission is a special case of an operation and the state of a single photon can be encoded onto several parallel channels. Without adapting the protocol further however, the same error tolerances as for quantum error correction also apply here, i.e. less than $\sim 10^{-5}$ for local operations and 10^{-2} for transmission [39]. In 1998 however, Briegel *et al.* [40] introduced another scheme which utilizes the fact that in communication one has access also to two-way classical communication. This scheme allows for greatly reduced

error tolerances, down to the level where they might be experimentally achievable with near-future technology. Their idea was called quantum repeater, and after modifications to the scheme by Duan *et al.* [41], it appears today to be the most promising way of realizing long distance quantum communication.

An important component in the quantum repeater schemes suggested so far is a quantum memory, capable of storing and retrieving single qubits with both high efficiency and high fidelity. Several schemes using rare-earth-ion-doped crystals for implementation have been put forward and in this chapter I will introduce these schemes and present the work done by us so far. I will also briefly explain how quantum repeaters work and discuss why quantum memories are important.

6.1 Photon sources

Another important component in quantum communication is the photon source. As we will see, quantum memories are useful not only to the communication procedure as a whole, but are also useful for improving the sources. A brief description of the most common sources will follow.

6.1.1 Single photon senders/attentuated pulses

The most simple 'single' photon source to be implemented is probably strongly attenuated light from, for example, a pulsed laser. With a stable enough laser one can control the photon distribution such that on average, there is less than one photon for each wave packet, and that the chance of having two photons in any single wave packet is very small. However, the attenuated pulse implementation has several drawbacks. Firstly, given that the average photon number should be less than one and that the distribution is Poissonian, it can be seen that most of the wave packets will actually contain zero photons, which makes the source very inefficient. Secondly, even if the average photon number is small, there is still a non-zero chance to get two photons in a packet. It has been shown that in the presence of noise or fiber losses, this causes a potential security hole for quantum cryptography implementations based on these sources [42]. Nevertheless, because of its simplicity, this technique has been used extensively, primarily in the early experiments (e.g. [43]).

6.1.2 Spontaneous parametric down-conversion

Theory

Spontaneous parametric down-conversion (SPDC) is a second order, non-linear, dielectric process and was first observed in 1970

[44]. Any incoming electromagnetic field will interact with a dielectric medium. For low intensities, it is normally adequate to consider only the first order interaction, which was done in Section 2.1. However, there may be higher order interactions as well, and a general expression of the induced polarization in an atom, by field of amplitude E, is given by

$$P = \epsilon_0 \chi^{(1)} E + \epsilon_0 \chi^{(2)} E^2 + \epsilon_0 \chi^{(3)} E^3 + \dots, \tag{6.1}$$

where $\chi^{(n)}$ is the susceptibility of order n. In this process, it is possible for an incoming photon of frequency ω_p to spontaneously convert into two new photons which must satisfy energy conservation

$$\omega_p = \omega_1 + \omega_2, \tag{6.2}$$

as well as momentum conservation

$$\mathbf{k}_p = \mathbf{k}_1 + \mathbf{k}_2 \Rightarrow n_p \omega_p = n_1 \omega_1 + n_2 \omega_2, \tag{6.3}$$

where n_i is the refractive index along the respective light polarization direction. This process is illustrated in Figure 6.1.

The two frequency components ω_1 and ω_2 may, but do not have to be, equal to each other. In general, the two resulting frequencies are determined by the respective refractive indices according to Equation (6.3). There are two common ways of achieving a phase matching that complies with this requirement. The first is using particular beam angles in birefringent crystals, such that the ordinary refractive index matches one of the frequencies and the extraordinary index matches the other frequency (when $\omega_1 \approx \omega_2$). If all three components are different, more advanced rotational matchings have to be used. The second way is through what is known as *periodically poled crystals*, where the phases are allowed to drift apart for some small distance, at which point the sign of the $\chi^{(2)}$ component is switched in some way, causing the frequency components to rephase. This procedure is then repeated periodically to ensure that a quasi-phase matching is kept throughout the crystal.

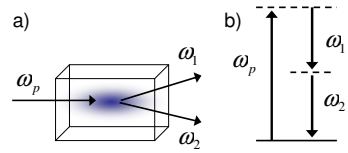

Figure 6.1. *Schematic description of spontaneous parametric down-conversion, where an incoming pump photon is converted into two photons of lower frequency components, with energy conservation as illustrated by the (virtual) level diagram in b).*

Applications

There are two main ways of using the parametric down-conversion process as a single photon source for quantum communication. The first is what is called a *heralded* single photon source. The creation of the photon pair is triggered by vacuum fluctuations, which are inherently random, and thus the two photons are created at random times. However, if one is interested only in using SPDC as a single photon source, then one can exploit the fact the two photons are created simultaneously and always in pairs. One can, for example, put a detector at the outgoing angle of the ω_1 photon and use a click in this detector as a herald that announces the coming

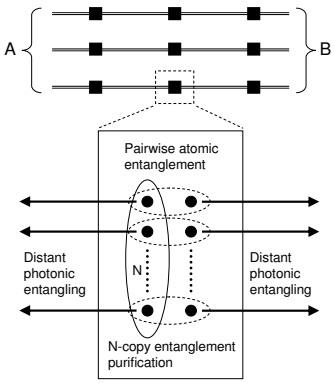

Figure 6.2. *Schematic illustration of communication by generating entangled pairs between point A and point B, using parallel channels for each desired final entangled pair, and enhancing the fidelity at several nodes (squares) along the way, in the form of quantum repeaters. The pairwise atomic entanglement within a node is generated independently for each node, which are then subsequently connected via distant photon entangling mechanisms.*

of the second photon, which can then be used in experiments. In essence, using heralded single photons is an improvement on the photon number statistics compared to using weak coherent pulses, although losses and dark counts still create some deviation from an ideal photon distribution. This is the point where quantum memories come in, since a reliable quantum memory could turn the probabilistic SPDC source into a triggered single photon source, and such a triggered source would eliminate the security hole for weak coherent pulses that was mentioned above and discussed in detail in [42].

A second way of using parametric down-conversion is generating entanglement, e.g. by putting two crystals immediately after each other, but with the second one tilted by 90° relative to the first one. Care should be taken to ensure that the two crystals both fulfill any phase matching conditions, as well as being in the same both spatial and temporal mode, i.e. they are indistinguishable. It is then not possible to determine in which of the two crystals the event actually happened, when something is detected. If they are perpendicular, then the polarization would be different depending on in which crystal the process happened, and one could then get a situation where the resulting photon pair would be in an entangled state of the form

$$|\psi\rangle = \frac{1}{\sqrt{2}}(|H_1\rangle\,|H_2\rangle + |V_1\rangle\,|V_2\rangle), \tag{6.4}$$

where H and V represent horizontal and vertical polarization respectively. Quantum cryptography can also be implemented by sharing such an entangled pair [45] and is also safe against eavesdroppers.

6.2 Quantum repeaters

The main idea behind quantum repeaters is to increase the total success rate and fidelity of quantum information that is sent along a noisy communication channel. This would be done by using parallel physical channels for each unit of information, and storing the information in quantum memory nodes along the channel, where entanglement purification can be performed. The first full scheme of a scalable repeater was described, as mentioned, by Briegel *et al.* [40], and it in turn relies on quantum privacy amplification or purification schemes described by others (e.g. [46, 47]).

The essential parts and the use of a quantum repeater is described in Figure 6.2. To establish reliable quantum communication between two distant points, A and B, for each desired entangled pair, N parallel channels will be used. Along each final line, repeater nodes are then placed to continuously remove errors in the entanglement. Each repeater node consists of quantum

memories that can be pairwise entangled in advance. These nodes can then be connected using photonic entangling procedures, such as entanglement swapping via Bell state measurements. An important aspect of increasing the error tolerance, below which the scheme works, is that the quantum memory entanglements are each prepared independently of each other, and that the result of the connection entanglement can be communicated using 2-way classical communication.

The number of channels, N, needed in the purification protocols depends on the error rates, and further, the protocols only work above a certain minimum fidelity. This restriction would have put a maximum limit on the total possible entangling distance, but, as was shown already by Briegel [40], nested levels of parallel channels can be used to overcome this issue. The total number of channels needed would be N^n, where n is the number of levels needed to obtain the minimum fidelity. However, it was then also shown that n scales only logarithmically with distance, which means that the total overhead resource cost would effectively scale only at most polynomially with distance.

For quantum memories to work well in repeaters there are a few different variables that should be maximized. These include storage time, efficiency and fidelity, and a few words about them can be said. As mentioned above in Section 6.1, the storage time in quantum memories will allow otherwise probabilistic processes to become synchronized, and, in addition, a longer storage time will also increase the maximum transmission distance. The efficiency is the repeatability of the scheme, i.e. how often it succeeds, and this will directly effect the maximum rates of transmission. The fidelity is a measure of how well the quantum state, including phase, is being maintained, and has been defined more carefully in Chapter 5. The fidelity is naturally an essential parameter for creating highly entangled communication pairs, but can be improved at a cost of additional resources, such as parallel channels.

6.3 Rare-earth implementation

Several suggestions for implementing quantum memories has been suggested, including stopped light using EIT/Dark state polaritons [48], off-resonant Raman interactions [41], Controlled Reversible Inhomogeneous Broadening (CRIB) [49–51] and, very recently, Atomic Frequency Combs (AFC) [52, 53]. Of these, both CRIB and AFC were suggested with rare-earth-ion-doped crystals directly in mind. The idea behind both of these schemes is to utilize the natural inhomogeneous absorption profiles and to store the photons in collective atomic ensemble states. These two schemes will be the focus in the following. First however, the more basic principle of photon echoes will be explained, as both CRIB and

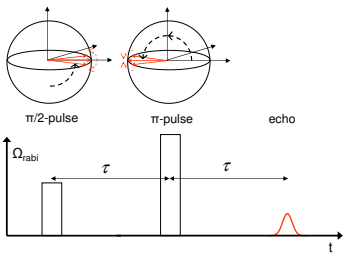

Figure 6.3. *2-pulse photon echo generation. A $\pi/2$ pulse, followed by a π-pulse causes the dephased atomic superposition to be flipped, and then rephased, which gives a strong emission peak which is called a photon echo.*

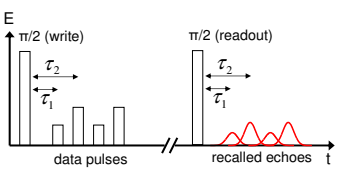

Figure 6.4. *Storage and recall of a sequence of 4 different pulses using the photon echo technique. Note that the information on both amplitude and timing of the pulses is stored by the material (in the form of a spectral grating).*

AFC are based on similar mechanics.

All of the methods explained here are based on letting photons interact directly with the optical transition. The lifetime and coherence time of the optical transition is however somewhat limited, which of course would also limit the memory storage time. But in all methods described here, it is also possible to extend this time by adding an extra procedure, using two π-pulses, that transfer the optical excitation to a hyperfine level excitation, and back again to the optical levels for recall. This effectively extends the memory time to be limited by the coherence time of the hyperfine levels instead, which is much greater, as was discussed in Chapter 3. As an extra feature of this procedure, the propagation direction of the transfer pulses can also determine the propagation direction of the recalled state. This is discussed more in connection with the CRIB protocol, where it is seen that storage efficiency depends on the direction of the recalled pulse.

6.3.1 Photon echo data storage

In inhomogeneously broadened materials one can, as the name suggests, obtain an echo of previously sent in pulses by correctly matching the sizes of the pulses. Only a brief description of photon echoes is given here, but for a more mathematical treatment, see e.g. books such as that by Mandel and Wolf [54]. An illustration of a 2-pulse photon echo can be found in Figure 6.3. For a maximized echo signal, first a $\pi/2$-pulse is sent in, putting the atoms in to a 50/50 superposition. Because of the inhomogeneous broadening, all atoms have different resonance frequencies, and they will start to dephase as the Bloch sphere in the figure shows. Then, after a certain time, τ, a π-pulse is sent in, which flips all phase vectors by 180°. The direction of rotation however, depends only on the resonance frequency, and is thus not effected by the flip. This means that the atoms will start moving back towards being in the same phase, and a time τ after the π-pulse they will have rephased again. The rephasing effect will, as is explained in more detail in Section 8.2, cause the atoms in phase to radiate quadratically stronger as a function of the number of atoms, compared to atoms with random phases. Given that a typically prepared inhomogeneous peak in rare-earth crystals consists of approximately 10^9 atoms, the intensity increase due to being in phase is also a factor of 10^9, which is such a strong effect that a macroscopic emission peak is noted, which is the echo. The main limitation of the time 2τ that one can wait before obtaining the echo is set by the coherence time, T_2 of the optical transition. When the atomic phases have been randomized through decoherence, the quadratic intensity increase is no longer reached, which means there is no visible echo.

It is also possible to store and recall more advanced pulse se-

quences using the photon echo technique. In Figure 6.4 a sequence of 4 pulses is sent in, stored and recalled with a readout pulse that can be applied at will. In essence, one can view this as splitting up the π-pulse described in the 2-pulse photon echo technique, into several smaller pieces were the final pulse, the readout pulse, has a pulse area of $\pi/2$. The data pulses can be of varying amplitude, width and number, within some restrictions. As mentioned above, the echo signal will be lost if the total time it takes to store and recall it exceeds the coherence time, but note here that this does not include the time between the last of the data pulses and the readout pulse. During that time it is sufficient that the lifetime is sufficiently long, it does not have to be coherent. The reason for this is that the temporal information in the pulses, including phase, will, after the excitations, be stored as a population grating between the two levels involved. The readout pulse will put them back into the coherent superposition that is seen in the right-hand Bloch sphere of Figure 6.3, with an "efficiency" for each detuning that depends only on how close it was to the excited state, i.e. how close the data pulse was to being a $\pi/2$ pulse. In this way a storage of 4000 classical bits was demonstrated in rare-earths in 1995 [55], where a maximum areal storage of 1.2 Gbit/cm^2 was reached.

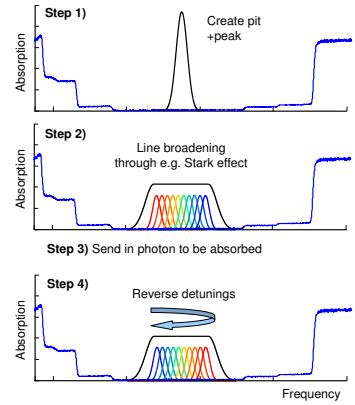

Figure 6.5. *Demonstration of the crib protocol. Step 1) Create pit and peak as described in Chapter 3. Step 2) Broaden the narrow line by some external field, e.g. by an electric field through the linear Stark effect. Step 3) Send in a photon that will be absorbed by the atoms. Step 4) Change the applied field such that the detunings are reversed, and the stored photon will be reemitted.*

6.3.2 CRIB protocol

Controlled reversible inhomogeneous broadening is based on the same idea as photon echoes in the sense that it is a rephasing effect that causes the stored pulse to be emitted again. However, as the name suggests, in CRIB the inhomogeneous character that causes the dephasing is a process that is fully controllable via external means, such as applied electric or magnetic fields. The main idea is described in Figure 6.5, which starts from an initialized system with a pit and peak created with the hole-burning techniques described in Chapter 3. The narrow peak is then broadened by applying some external field. It is for example possible to cause a detuning of the atoms through the linear Stark effect, by applying an electric field. The field could be applied in different ways, such as through a quadrupole configuration or in a linear fashion, either along the direction of propagation of the photon to be stored, or perpendicular to it. The particular choice of field configuration will influence the maximum obtainable efficiency, as we will soon see. Since the particular detuning for each atom depends on the applied electric field, if the electric field is reversed in sign for all atoms, so will the detunings away from the center frequency be. The effect of this is the same as the second π-pulse in the 2-pulse photon echo described above. The atoms that were dephasing before will now start to rephase, and when they all reach the same phase, they will emit coherently and the photon emission proba-

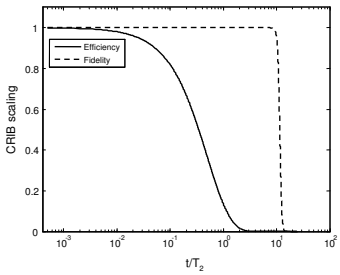

Figure 6.6. *The solid line shows the decay of a photon echo as a function of time in units of* T_2*, and is in some sense proportional to the efficiency of the CRIB protocol. The dashed line shows the visibility between the interference fringes from two echoes, which is proportional to the fidelity of the CRIB protocol. The delay before the fidelity goes down is due to a collective effect from the, in this case,* 10^9 *atoms. Note that the x-axis is on a log scale which makes the decline of the fidelity look sharper than it really is, compared to the efficiency.*

bility is greatly enhanced at this time, i.e. the photon is recalled.

Recall efficiency

The efficiency of the CRIB protocol will depend, among other things, on the configuration of the electric field. For a broadening across the transverse direction compared to the propagation axis, and for a recall in the backwards direction (accomplished through the hyperfine state transfer pulses as mentioned above), the efficiency is given by (see [56] and references therein)

$$\eta_{\text{backward}} = \left(1 - e^{-\alpha L}\right)^2, \tag{6.5}$$

where αL is the optical depth, and one can see that it is possible to achieve an efficiency close to unity for high enough values of αL. Implementing the same transverse broadening but with recall in the forward direction, the efficiency is different and instead given by

$$\eta_{\text{forward}} = (\alpha L)^2 e^{-\alpha L}. \tag{6.6}$$

It is easily checked that this function has a maximum for $\alpha L = 2$, which gives an efficiency of $\eta_{\text{forward}} = 54\%$. In this protocol it is thus not possible to get 100% efficiency in the forward direction. One could also apply the electric field longitudinally along the propagation direction however. For such a field configuration, the efficiency for recall in both directions can be the same and given by [56]

$$\eta_{\text{long}} = \left(1 - e^{-2\pi\kappa/\chi}\right)^2, \tag{6.7}$$

where κ and χ consist of material parameters, but the total exponent $2\pi\kappa/\chi$ corresponds to the effective optical depth of the medium. We see that this expression is very similar to the backwards recall scheme for transverse fields, and that the efficiency here can approach unity in both directions, although it should be pointed out that in the forward direction there is a residual distortion in the form of a chirp for the recalled pulse.

Fidelity scaling

The efficiency of the storage decreases exponentially with the coherence time, T_2, as is expected, but it is interesting to note that, because of collective effects, the fidelity of the recall gains a temporary "respite" before declining. This was first seen in an experiment described in Ref. [57], where the visibility of the coherent interference fringes from two recalled pulses was measured. This behavior is illustrated in Figure 6.6, where functions that represent the efficiency as well as the fidelity has been plotted as a function of time, in units of T_2. The delayed decline can be explained by noting that the coherent emission scales quadratically with the

number of atoms that are still coherent, while all emission from atoms that have dephased, scales only linearly (see Section 8.2). As time progresses, the number of atoms that remain in the coherent state, N_c, will be fewer and fewer, while the number of dephased atoms, N_d, will grow at the same rate. If N is the total number of atoms in a peak, and there is a constant probability for a coherent atom to become dephased per unit of time, then

$$\begin{cases} N & = N_c + N_d \\ \frac{\partial N_d}{\partial t} & = N_c \frac{1}{T_2} \end{cases} \tag{6.8}$$

Solving this system for all atoms in the coherent state initially, yields

$$\begin{cases} N_d & = N\left(1 - e^{-t/T_2}\right) \\ N_c & = Ne^{-t/T_2} \end{cases} \tag{6.9}$$

In an interference experiment, the peaks of the visibility fringes are given by the total sum of coherent and dephased emission, while the valleys are given by the light only from the dephased atoms. In addition to the difference arising from the quadratic intensity effect, the light from the dephased atoms is diminished by an additional factor, Ω_d, which is the solid angle made by the coherent laser beam. This factor appears since all light emitted by the coherent atoms goes into the same spatial mode, the laser mode, but light coming from the dephased atoms can be emitted into any direction. The visibility for the experiment can thus be expressed as

$$V = \frac{(N_c^2 + \Omega_d N_d) - \Omega_d N_d}{(N_c^2 + \Omega_d N_d) + \Omega_d N_d} = \frac{N_c^2}{N_c^2 + 2\Omega_d N_d}. \tag{6.10}$$

Inserting the expressions given in Equation (6.9), we get

$$V = \frac{1}{1 + \frac{2\Omega_d}{N}\left(e^{2t/T_2} - e^{t/T_2}\right)} \approx \frac{1}{1 + \frac{2\Omega_d}{N}e^{2t/T_2}}. \tag{6.11}$$

We can then identify the point at which the visibility drops (as seen in Figure 6.6 this happens very fast, so we can take $V \sim 0.5$), and we find that the time of the decline is given by

$$t_d = \frac{1}{2}(\ln N + \ln\frac{1}{\Omega_d} - \ln 2)T_2\Big|_{\substack{N=10^9, \\ \Omega_d = 10^{-6}}} \approx 17T_2. \tag{6.12}$$

This respite in the decline of the visibility is an advantage of the ensemble approaches to quantum memory. For typical values of the number of atoms in a peak used for photon storage, 10^9, and a laser solid angle of $\sim 10^{-6}$, we get a prolonged visibility, and thus fidelity, of about a factor of 17, compared to what would be expected from the coherence time. As both factors come in only logarithmically however, it is difficult to increase this gain

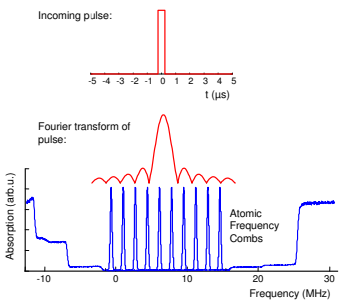

Figure 6.7. *An incoming pulse is stored in a memory based on atomic frequency combs. Even though it looks as though some parts of the frequency content is in between the combs, it has been shown that close to 100% absorption is possible [52].*

any further. One can also note that if the effective coherence time, perhaps due to inhomogeneous broadening, is very short compared to the lifetime, by using time gating, one can gain an additional discrimination effect that gives the same type of contribution as the other two effects. This was not included here, since optimally, the coherence time should be kept as long as possible.

6.3.3 AFC protocol

When considering the role of quantum memories in repeaters one sees that there is a need for multimode capacity in the memory, in the sense that it is a clear advantage if several qubits can be stored in the same memory. Both the CRIB protocol and EIT-based memory schemes can in principle handle this, but only for high values of αL. For example, the number of modes, n, that can be stored in EIT- and Raman-based memories scale as $\sqrt{\alpha L}$, which puts an effective limit on the number of modes that can be stored in experimentally achievable conditions. The CRIB protocol scales better, $n \sim \alpha L$, but will eventually also be limited by the optical depth. Very recently, a new protocol, based on an atomic frequency comb structure, was proposed [52], where the multimode capacity is independent of the optical depth. This protocol has also been experimentally demonstrated in the case of storing pulses attenuated down to the single photon level [53].

The main points of this scheme is illustrated in Figure 6.7, where a spectral grating in the form of atom population peaks is created inside a pit. An incoming pulse has a certain frequency content, determined by its fourier transform, which is also explicitly drawn in the figure. Even though some parts of the fourier transform appear to exists between the atomic peaks, it has been shown in [52] that with sufficiently high αL, all of the incoming pulses can be absorbed by the comb structure. For storage of many temporal modes, the information is maintained in the atomic peaks in the form of phase shifts. The first pulse that comes in will create a certain excitation which depends on its fourier transform, as shown in Figure 6.7. Because all peaks have different frequencies, the stored frequency components will acquire different, but periodic phase shifts. Depending on the value of each phase at the time the second pulse is absorbed, there is either a constructive or a destructive interference effect between the excitations caused by the different pulses, which effectively creates a grating that contains all the temporal information. This grating structure can be characterized by the width of each peak, γ, and the separation between the peaks, Δ. The finesse of the grating can then be defined as $F \equiv \Delta/\gamma$. It was then shown that, if each peak has a certain αL, then the effective optical depth of the whole comb structure

can be written

$$(\alpha L)_{\text{eff}} \approx \frac{\alpha L}{F}, \tag{6.13}$$

and it can be seen that a smaller finesse would increase the absorption probability. However, a higher finesse is required to obtain smaller dephasings during the storage time, so there is a conflict concerning the way to tune the finesse. For a given experimental situation, with a certain value of the peak αL, an optimum finesse can therefore be obtained. The efficiency of storage recall in the AFC protocol can be written [52]

$$\eta_{AFC} = \left(a - e^{-(\alpha L)_{\text{eff}}}\right) e^{-\frac{1}{F^2}\frac{\pi^2}{4\ln 2}}, \tag{6.14}$$

and we can see that the efficiency depends only on the optical depth and the finesse. For a reasonable value of the finesse of about $F = 10$, it can be seen that an αL of about 40 is required to obtain an efficiency of over 90%. This is a situation that is not unrealistic with today's experimental technology, although it should be noted that working in a high αL regime does introduce some additional considerations, such as off-resonant excitations, superradiance emission and slow light, as discussed in Paper **VI** and in the following chapters.

Chapter 7

Dispersion related phenomena

There are several coherent phenomena that are related specifically to the manipulation of the absorption profile, and thereby also to the dispersion profile. These phenomena include slow light, fast light and electromagnetically induced transparency (EIT), which will all be covered in this chapter. There is also a connection to other topics in this thesis. As mentioned in the previous chapter, EIT is one of the schemes that has been suggested for the implementation of quantum memories [48]. In addition, as is demonstrated in Paper **VI**, slow light will be an unavoidable factor in all quantum memory protocols, since the high optical density required for efficient memories also implies sharp dispersion profiles, which is exactly what gives rise to the slow light, as we will see.

The group velocity of a light pulse through a material is given by

$$V_g = \frac{c}{n_g}, \tag{7.1}$$

where n_g is the group refractive index, given by

$$n_g = n_R + \omega \frac{\partial n_R}{\partial \omega}, \tag{7.2}$$

where n_R is the real part of the normal refractive index. From these two equations it is clear that by tailoring the derivative, $\frac{\partial n_R}{\partial \omega}$, one can make the the light pulse travel at an arbitrary speed, including higher than c or even negative. A negative speed would mean that the pulse exits the material before it has entered, which at first sight may look preposterous. In Section 7.2 however, we will go through the phenomenon in detail and the apparent causality breach will be explained, and it will be discussed how this can be implemented in rare-earth crystals. But let us first go through how one can obtain media with suitable refractive indices.

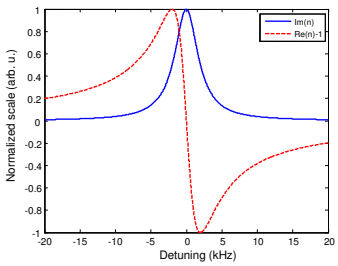

Figure 7.1. *A typical Lorentz-shaped absorption profile ($\alpha \propto Im(n)$), with the corresponding real part of the refractive index. Both have been normalized to have a max value of one.*

7.1 Absorption curves

7.1.1 Single resonances

From Equation (7.2) it is clear that for phase and group velocity to differ strongly we need a situation where the refractive index varies greatly with frequency. A very good candidate for this is an atomic resonance line, where the strong absorption exactly on resonance has major effects on the light. A typical absorption curve from a lifetime-limited resonance line follows the Lorentz shape and is shown in Figure 7.1. The absorption coefficient is given by the imaginary part of the refractive index, which, close to a resonance line, can be approximated by [58] (the Lorentz shape)

$$n_I(\omega) = K \frac{\Gamma}{(\omega - \omega_0)^2 + \Gamma^2}, \tag{7.3}$$

where $K = Ne^2 f / 4m\omega_0\epsilon_0$ is a constant. N is the difference in population (per volume) between the upper and lower state of a transition with center frequency ω_0 and width Γ. The charge and mass refer to the electron, f is the oscillator strength, and ϵ_0 is the dielectric constant.

Quite generally, one can assume that the frequency is of complex nature, i.e. $\omega = \omega_R + i\omega_I$, where the real part is the normal frequency and the complex part describes a dampening, which is easily seen from the typical expression of a wave $e^{i\omega t} = e^{i\omega_R t} e^{-\omega_I t}$. For the refractive index, $n(\omega)$, the bottom half of the complex frequency plane does not represent a real physical situation, since the 'dampening' turns into an exponentially escalating term. In order to keep the upper half of the complex plane physical, we require that the refractive index in this half plane is analytical, i.e. it is single-valued and possesses continuous derivatives. Interestingly, it turns out that the requirement of analyticity is exactly equivalent to demanding that the system obeys causality [59]. A direct consequence of this, are the Kramers-Krönig relations (see e.g. [60]), which uniquely correlate the real and imaginary parts of the refractive index to each other. Given our expression for n_I above, n_R will then be given by [58]

$$n_R(\omega) - 1 = -K \frac{\omega - \omega_0}{(\omega - \omega_0)^2 + \Gamma^2}, \tag{7.4}$$

which is also plotted in Figure 7.1. From Equation (7.2), we deduce that the group velocity is to a large extent determined by the dispersion of the real part of n, i.e. $\frac{\partial n_R}{\partial \omega}$. This derivative is given by

$$\frac{\partial n_R}{\partial \omega} = K \frac{(\omega - \omega_0)^2 - \Gamma^2}{\left((\omega - \omega_0)^2 + \Gamma^2\right)^2}, \tag{7.5}$$

and is plotted in Figure 7.2. Slow light is obtained when this function is positive and fast light is obtained when it is negative.

In particular, when the expression $n_R + \omega \frac{\partial n_R}{\partial \omega}$ is negative, the group velocity is also negative. The meaning of this is discussed further Section 7.2.

7.1.2 Gain doublets

One drawback of using single resonance lines, as discussed above for fast and slow light experiments, is pulse distortion. Since the largest velocity change occurs in the middle of the resonance line, as seen in Figure 7.2, there is also a strong absorption or gain effect, depending on inversion level. These effects can strongly alter the shape of the pulse that is sent through the material, and it can thus become difficult to analyze the resulting pulses, and separate absorption effects from the pulse propagation effects. Imagine for example an experiment on a strong absorption line, where the first 90% of the pulse is absorbed, and only the last 10% gets through. Regardless of pulse propagation effects, it would here look as though the exiting pulse was retarded by $\sim 40\%$ of its duration.

Another setup, which has been used in later experiments to greatly reduce the effects of this problem (e.g. [61]), utilizes a gain doublet line. The negative absorption that corresponds to a gain medium is shown in Figure 7.3, with the associated real part of the refractive index, whose derivative determines the propagation velocity. In the figure, we see that the greatest pulse propagation effect is obtained at the center of the figure, where the derivative is large, just as for the single resonance case. The advantage in the gain doublet case however, is that the absorption (gain) here is at a minimum, which means that we can avoid as much of the pulse distortion effects as possible. Normally a medium with a natural doublet line is chosen for such experiments, but for implementation in rare-earth crystals, it is a simple matter of preparing two peaks inside a spectral pit, using the hole-burning techniques discussed in Section 3.7.

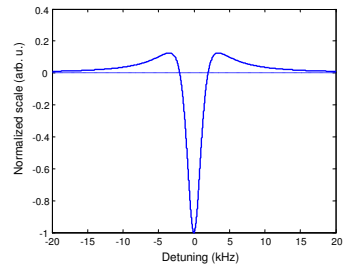

Figure 7.2. *Dispersion profile, i.e. the derivative, $\frac{\partial n_R}{\partial \omega}$, of the real part of the refractive index, plotted in Figure 7.1. Note that the largest anomalous effects are obtained at the center of the profile, when this derivative is negative.*

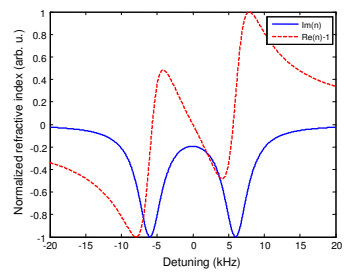

Figure 7.3. *The solid blue line represents the (negative) absorption profile of a doublet gain medium. The dashed red line is the real part of the refractive index, and, as can be seen, just as for the single resonance line, the largest dispersion effects are at the center of the figure, but here, the absorption effects are at a minimum.*

7.2 Fast and slow light

The speed of light in vacuum is (exactly) 299 792 458 m/s and is, according to the assumptions made by Einstein in the formulation of special relativity, constant and independent of the viewer's reference frame, in contrast to everything else in the universe. A necessary consequence of special relativity (but not yet of the general one) and of the preservation of causality, is that no signal can travel faster than the speed of light. Yet, according to the discussion above, it appears possible to find dispersion curves, such that the group velocity is higher than the speed of light, or even negative. To understand what this really means, it is important to clearly define what is meant by a 'signal'. Most attention in

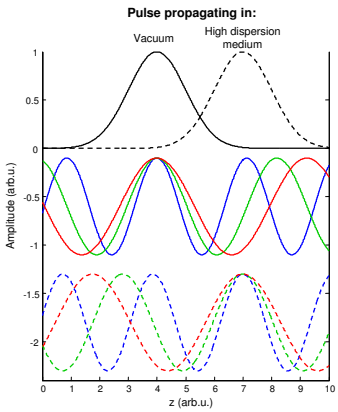

Figure 7.4. *Pulse propagation along an axis (z) for vacuum (solid lines) and through a high dispersion material (dashed lines), such as the gain doublet. The colored lines represent the Fourier components of the pulse, which in the high dispersion material propagate with different velocities, giving rise to an apparent pulse advancement.*

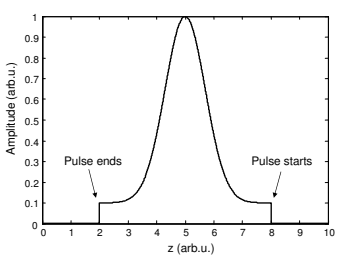

Figure 7.5. *Gaussian pulse with the switch-on and cutoff points greatly exaggerated.*

this section will be focused on fast light, since this is much more conceptually controversial, but most of the discussion is just as applicable to slow light effects.

7.2.1 Pulse peak advancement

Consider an example of sending a pulse, say a Gaussian pulse, through a medium. It would then be tempting to associate the 'information' that is being sent, with for example the peak of the pulse. This is not a good definition however, as has also been demonstrated experimentally. Even though other experiments on fast light had been done before, it is interesting to use the results of Wang *et al.* [61] published in 2000, since here, the pulse was transmitted almost without absorption or distortion. In these experiments a Gaussian pulse was sent through a medium of prepared caesium atoms, and it was reported that the peak of the transmitted pulse exited the medium 62 ns before the peak of the incident pulse entered it! In other words, the peak of the outgoing pulse travels about 19 m away from the medium before the peak of the incident pulse even arrives, though it is worth pointing out that the pulse advancement time is still much smaller than the total duration of the pulse.

To explain how these results can be interpreted, let us consider the Gaussian pulse in terms of its frequency components. According to Fourier theory, any pulse be can written as a sum of plain sine waves of different amplitudes, following a certain frequency distribution. A Gaussian pulse for example, also has a Gaussian distribution in frequency. The pulse, as a sum of sines, when it propagates through vacuum, is illustrated by solid lines in Figure 7.4. The dashed lines in the same figure show the pulse if it had instead propagated through a fast light medium, such as the gain doublet system. Due to the fact that the refractive index is different for all individual frequency components of the pulse, they all travel through the medium at different velocities. After the medium, the point where they are in phase, i.e. the point where the peak occurs, has been changed.

7.2.2 Signal definition

From the discussion in the previous section it is clear that the pulse peak (or the slopes of the pulse for that matter) can indeed travel faster than the speed of light. Therefore, if we believe in causality and Einstein's requirement that no information can travel faster than the speed of light in vacuum, we need to define 'information' as something else than the peak or the slopes of the pulses. Important work in this area was done by Brillouin and Sommerfeld [62], who offered a definition that is consistent with causality and relativity theory. What they focused on was the fact that any sig-

nal must be started as a sharp 'step'. In Figure 7.5 a Gaussian pulse is shown with these sharp cutoff's exaggerated to illustrate the effect. On the condition that

$$n(\omega) \to 1 \text{ when } \omega \to \infty \tag{7.6}$$

(which is physically perfectly reasonable), it can be shown that any information defined as the sharp switch-on, starting from zero, never propagates faster than c. In fact, the switch-on point propagates exactly at c in any medium. This can be understood intuitively because a sharp cutoff or switch-on implicates high order frequency components, which, according to the requirement of Equation (7.6), must travel at a refractive index of one.

The definition of 'information' as the start of the pulse only, seems to imply that the rest of the pulse contains no information, and this is also true to some extent. A function is said to be analytic if it is infinitely differentiable, i.e. if the function and all of its derivatives are continuous. Furthermore, if two analytic functions are identical in some small domain, then they must also be identical outside this domain (if the domain is simple enough). For this discussion, the important implication is that if we know an analytic function for a small amount of time, then we know it for all later times as well. This extension is known as analytic continuation [63], and shows that there is no information in the later parts of a pulse that cannot be obtained already from the first part of it. Of course, this is only true for pulses which have continuous derivatives. Any point in a pulse in which the pulse itself or one of its derivatives are discontinuous, is not a part of the analytic behavior. In fact, any such point acts just like the sharp switch-on, which travels at a velocity of c, regardless of medium. This effect is illustrated in Figure 7.6, which has been reproduced from Ref. [64]. This figure shows what happens to an abrupt change in an otherwise analytic function, when it passes through a fast light medium. The solid line represents the pulse sent in to the medium, and the dashed line what the pulse would have looked like, had it continued. The Gaussian pulse is cut off before the peak occurs, but after passing through the fast light medium, the pulse appears *with* a peak. This is because the information about the discontinuity travels at c, which in this case is slower than the peak, which travels at $v_g > c$. When the information about the cutoff reaches the other side of the medium, a distortion occurs, but for sufficiently large group velocities, almost the whole Gaussian pulse can be recreated by the medium, given only the small input part.

The first part of a pulse, immediately following the switch-on, effectively ignores some of the effects of the medium. As already mentioned, it travels exactly at c, and it will also pass unattenuated through the medium, even if the medium has a high absorption otherwise. This first part of the pulse is sometimes referred to

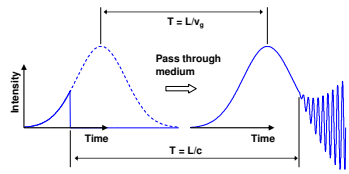

Figure 7.6. *A Gaussian pulse that is cut off at an early time is seen before the medium, to the left, and after a fast light medium to the right. Because of analytic continuation, the effects of the cutoff cannot be noticed until after a time that corresponds to traveling at c.*

as an optical precursor, and has been experimentally investigated e.g. in Ref. [65]. The duration of the optical precursor varies with the spectral width of the feature, getting shorter the broader the feature is.

7.2.3 Slow light

Slow light has many conceivable applications, especially in the quantum communication area. Photons interact very weakly with for example other photons, and schemes based on photon-photon interactions can benefit greatly from slow light effects, since it simply gives the light more time to interact [66]. Further, it has been suggested that some optical technologies, like parametric down conversion, can be much better characterized using slow light, as it can be used to bring the events down to time scales at which detectors can temporally resolve them. The creation of slow light effects however, is very similar to what has been discussed for fast light above, since just as fast light can be created through a medium with a negative dispersion, a large positive dispersion would give a velocity slower than normal light. In our crystals, slow light effects can be observed from an empty pit, simply from the fact that the absorption outside the pit can be as high as $\alpha L = 80$, while it is close to zero inside the pit, and this creates a strong dispersion profile. In the experiments connected to Paper **VI**, we measured a group velocity of the order of ~ 40000 m/s, but velocities down to only a few meters per second have been measured by others [67].

7.2.4 Rare-earth implementation

Rare-earth-ion-doped crystals are good solid state materials to be used also for more advanced fast and slow light implementations, and the system in Lund is good in particular because it has a very high degree of controllability of the atomic spectral features. A concrete example of an experiment for producing fast light with sechyp pulses of 2π pulse area, was recently suggested by Clader and Eberly [68]. The main idea in this article is to produce fast light in a simple, two-level, atomic system which has been prepared with a perfectly inverted population, a situation that can easily be obtained in our experimental setup. Using sechyp pulses with FWHM τ on such an inverted resonance line, gives, under the restriction that $T_2^* >> \tau$, a group velocity of [68]

$$v_g = \frac{c}{1 - \frac{g\tau^2}{2}}, \tag{7.7}$$

where, according to the article, $g = N\mu^2\omega/\epsilon_0\hbar$, with μ being the transition dipole moment and N the atom concentration. For such a group velocity the advancement time, τ_{adv} of the fast light pulse,

would be given by

$$\tau_{adv} \equiv \frac{L}{c} - \frac{L}{v_g} = \frac{Lg}{2c}\tau^2, \tag{7.8}$$

for a certain medium length, L.

In order to see whether this is observable in our material, we can consider a necessary absorption coefficient $\alpha = \sqrt{\pi/2}gT_2^*/c$. Expressing g above in terms of α, changes Equation (7.8) into

$$\tau_{adv} = \frac{\alpha L\tau}{\sqrt{2\pi}T_2^*}\tau. \tag{7.9}$$

Given the restriction that $T_2^* >> \tau$, and a desire to get as large a pulse advancement time as possible, the ratio τ/T_2^* is pretty much fixed at $\sim 1/10$. This leaves only the total effective absorption, αL, as a tweaking parameter, but we see that, in order to get a pulse advancement time of the order of 10% of the duration, which is easily detectable, we only need an αL of about $\sqrt{2\pi} \approx 2.5$, which has been demonstrated for a well controlled peak in our lab, e.g. in Paper **VI**.

As will be explained in more detail in Chapter 8, a fully excited peak will not remain very long in the excited state, due to collective radiation effects, such as superradiance. Because of this, it will be desirable to use as short a sechyp width as possible, in order to get the fast light effects to happen before the collective decay. Lower limits to the pulse width, τ, will come from pulse creation parameters, such as AOM rise times, but also from the fact that the cleanest fast light effects are obtained from pulses with a pulse area of 2π, and given a limited maximum Rabi frequency from the available laser source, a minimum pulse width is also given. For our particular situation, pulse widths of about 200 ns will work within the restrictions, and this choice also fixes the peak width at about $\Gamma_{inh} \sim 1/(\pi \cdot 10\tau) = 150$kHz.

7.3 Electromagnetically Induced Transparency

7.3.1 Basic theory

Electromagnetically induced transparency (EIT), is not caused by anomalous dispersion, but it does give rise to very steep dispersion curves, that can in turn be used for slow light. At first sight at least the explanation behind EIT is fairly simple. Consider a Λ-system, where the three levels could be one excited state $|e\rangle$, and two of the hyperfine ground states, $|g_1\rangle$ and $|g_2\rangle$, in the Pr^{3+}-ion. The transition dipole moments, μ_i, of the two transitions for this system are different, but let us assume that this can be compensated for by correspondingly different light amplitudes $\mathcal{E}_i$,

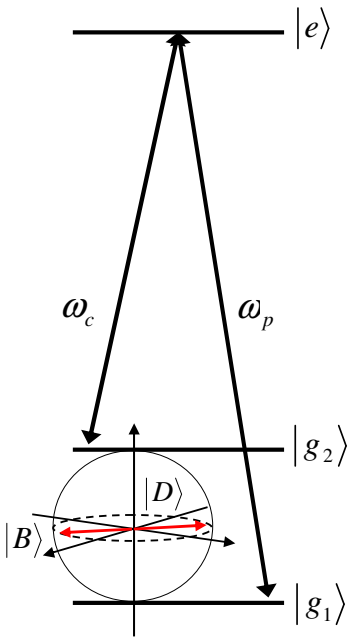

Figure 7.7. *The three relevant levels in a rare-earth EIT scheme. Coupling and probe pulses target the respective levels, and the created bright and dark states are illustrated through the inscribed ground state Bloch sphere.*

such that the product $p = \mu_i \cdot \mathcal{E}_i$, can be kept constant. The interaction Hamiltonian can then be written

$$H_{int} = -p\left(|e\rangle\langle g_1| + |e\rangle\langle g_2|\right) + h.c. \tag{7.10}$$

We can now define two different superposition states, $|B\rangle = |g_1\rangle + |g_2\rangle$ and $|D\rangle = |g_1\rangle - |g_2\rangle$. Letting the Hamiltonian couple these two ground state superpositions to the excited state, we see that $\langle e|H_{int}|B\rangle = -2p$ and $\langle e|H_{int}|D\rangle = 0$. The state $|B\rangle$ has a strong coupling to the excited state and is called the *bright state*, while the state $|D\rangle$ does not couple at all to the excited state, and so it is called the *dark state*. These two states are illustrated in a Bloch sphere in Figure 7.7. For a more detailed review of EIT theory, see e.g. Ref. [69].

For other systems, where the two transitions have the same resonance frequency, coherent population trapping can occur [70]. This happens if a laser is kept on at the two transitions. It will keep on exciting atoms from the bright state to the excited state, and once there they can decay to either the bright or the dark state. If they decay to the bright state they will just get excited again, but once they decay to the dark state they are trapped, since the light does not interact with that state.

7.3.2 EIT for rare-earth systems

For rare-earth ions, such Pr^{3+}, the two ground states do not have the same transition frequency. Therefore, in order to see EIT effects in a rare-earth system, two laser beams are needed. A strong coupling beam is tuned to one of the transitions, while the other transition is scanned by a weaker probe beam, at the levels shown in Figure 7.7. The probe beam will experience a sudden drop in absorption, within a certain width, δ_{EIT}, from the resonance. Assuming that the dephasing between the two ground states is very small, which it typically is for rare-earths, and that there is no detuning on the coupling field, the imaginary part of the susceptibility (the absorption coefficient) can be written [69]

$$\mathrm{Im}(\chi) = \frac{8|\mu_p|^2\rho}{\epsilon_0\hbar} \times \frac{\delta^2\Gamma_{inh}}{\left||\Omega_C|^2 + 2(i\Gamma_{inh} - 4\delta^2)\right|^2}, \tag{7.11}$$

where μ_p is the transition dipole moment for the probe transition, Ω_C is the Rabi frequency of the coupling field, and Γ_{inh} is the inhomogeneous peak width, which also gives the effective dephasing time for the excited state. This expression is plotted in Figure 7.8 as a function of probe detuning, δ, for two different values of Ω_C. As can be seen from the formula as well as in the figure, the width of the EIT shape is determined by the strength of the coupling field. For sufficiently large coupling Rabi frequencies, it looks as if the absorption peak splits into two parts, also

known as Autler-Townes doublets [71]. Figure 7.9 then shows an experimental version of the upper part of Figure 7.8, recorded by us in connection with Paper **V**.

Single beam detection

A useful technique for creating and detecting the EIT feature, and for looking at its temporal behavior, is as follows. First, an inhomogeneous peak inside a spectral pit is created, as described in Section 3.7. To create the EIT feature, two fields are required, as mentioned above, a stronger coupling field and a weaker probe field. Using a flexible pulse creation system however, such as AOMs, it is possible to create both fields using only a single beam, modulated with the two frequencies. First the AOM is modulated only with a component of the coupling frequency, ω_C, after which a weaker modulation on the probe frequency, ω_p is added to the AOM signal. Detecting this beam with both modulations on will yield a beating on the difference frequency, $\omega_p - \omega_C$, which in the Pr^{3+}:Y_2SiO_5 case is at 10.2 MHz. To see the EIT feature, the probe field can be detected after the crystal sample, by means of this beating, as is shown in the lower part of Figure 7.10.

The dashed line corresponds to detuning the probe field by an amount large enough to go outside the narrow EIT window, but small enough to still be absorbed by the inhomogeneous peak. The solid line is in the middle of the EIT transmission window, and the spectral width of this window can be obtained from the time constant of the transmission increase. For times shorter than the reciprocal EIT width, the Fourier width of the probe field is broader than the EIT width, which means parts of the probe field are absorbed outside the EIT window. As time goes on the Fourier width of the probe field narrows to eventually be completely inside the EIT window, at which point it levels out, as is also seen in Figure 7.10. The time constant can be determined from the figure to be about 5 µs, yielding an EIT width of about 60 kHz. This technique was also employed in Paper **V**, where a very good EIT window transmission of 96% was reached. In this paper it is also interesting to note that the EIT window had a width of about 60 kHz, even though the laser used to create and detect it, was an order of magnitude broader. The width of the EIT is not dependent on the laser coherence time, but rather is determined by the coherence time of the system alone, together with the coupling field Rabi frequency, as shown above in Figure 7.8.

Fano resonances

An interesting phenomenon which was observed in the experiments leading to Paper **V**, is Fano resonances. This was first described by Fano in 1961 [72]. He showed that auto-ionized states can inter-

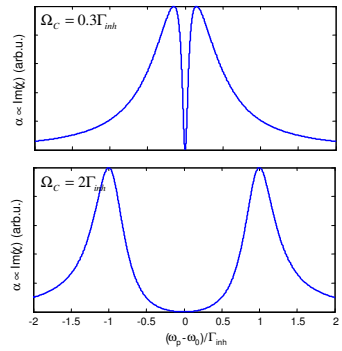

Figure 7.8. *The absorption profile of a prepared peak with the presence of a coupling field. The upper figure is for a weaker coupling field, and the lower figure is for a stronger coupling field, in relation to the inhomogeneous peak width.*

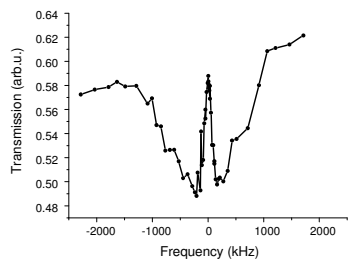

Figure 7.9. *Experimentally recorded EIT shape, as a part of the investigation in Paper* **V**. *Slightly asymmetric, but the transmission at the center was about 96%. Also note that it is transmission and not absorption as in Figure 7.8, so that it is inverted.*

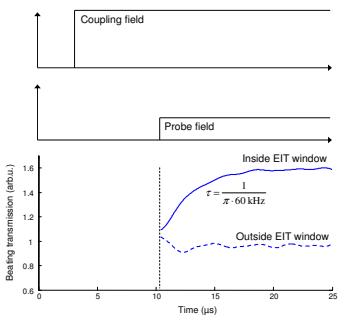

Figure 7.10. *As the probe field is switched on, a beating on the difference frequency is detected. The amplitude of the transmission of this beating is plotted in the lower part of the figure, as a function of time, both inside (solid line) and outside (dashed line) the EIT feature.*

fere with the continuum above the ionization limit. A similar interference can be achieved in the situation of the EIT experiments, where stimulated Raman photons on the coupling transition can interfere with the continuum of Rayleigh scattered photons. The effect is an asymmetrization of the EIT window, in close relation to the typical asymmetrical Fano profile.

Chapter 8

Collective coherent effects

The radiative decay from an ensemble of close lying atoms can, under certain conditions, exhibit far more complicated behavior than that of the atoms one by one. The effects to be discussed in this chapter include free induction decay (FID), superradiance, subradiance and superfluorescence. All of these effects are the results of the collective coherent properties of the atoms and there are many interesting applications that arise from them. For example, super- and subradiance can be used to speed up and slow down respectively, the decay rate of atoms, which is an important property in ,for instance, quantum memories. The chapter will begin with a theoretical focus, which turns into an effort to explain the superradiance effect with an intuitive interpretation, since I feel some of the existing literature is unclear on this point.

8.1 Radiation from an atom in a superposition

First, let us assure ourselves that any atom in a superposition of two states will radiate coherently. The quantum mechanical system that is the atom can be described by the Schrödinger equation

$$i\hbar\frac{\partial\Psi_n}{\partial t} = H\Psi_n, \tag{8.1}$$

where H is the Hamilton operator characterizing the system, and Ψ_n is the wave function of state n of the atom. For unperturbed systems the solution can be written in the form

$$\Psi_n(\mathbf{r},t) = u_n(\mathbf{r})e^{-i\omega_n t}, \tag{8.2}$$

where $u_n(\mathbf{r})$ is a function that takes care of all spatial dependence, and where all temporal dependence is in the complex phase factor. The wave function for an atom in a superposition of the ground and

excited state can be written $\Psi_{total} = (\Psi_g + \Psi_e)/\sqrt{2}$. Calculating the charge density, $\rho_c = e|\Psi|^2$, for such a superposition, gives

$$\begin{aligned}\rho_c &= \frac{e}{2}\left|u_g e^{-i\omega_g t} + u_e e^{-i\omega_e t}\right|^2 \\ &= \frac{e}{2}\left(|u_g|^2 + |u_e|^2 + u_g^* u_e e^{-i(\omega_g-\omega_e)t} + u_g u_e^* e^{-i(\omega_e-\omega_g)t}\right) \\ &= e\left(... + u_g u_e \cos(\omega_\Delta t)\right).\end{aligned} \tag{8.3}$$

where ... are the time independent terms. We see here that the charge density of an atom in a superposition oscillates at a frequency equal to the difference between the two levels, ω_Δ, and as we know, oscillating charges will create an oscillating field, i.e. radiate.

8.2 Collective radiation

To see what happens to the total radiation when multiple atoms are involved, we sum up the field from N atoms. The field, E, is proportional to the oscillating part in Equation (8.3) (last line), so it is essentially a problem of summing up cosine terms from every atom, each with a certain phase angle $\phi_{i=1...N} = \omega_{\Delta,i} t$. As given by the *law of large numbers* [73], the mean value of the total field will be the expectation value of each component

$$E \propto \langle \cos\phi_i \rangle = \frac{1}{2\pi}\int_0^{2\pi} \cos\phi_i d\phi_i. \tag{8.4}$$

If the atoms are just randomly excited, and thus completely incoherent, then this expectation value is zero. However, we are not really interested in whether the field, which at a certain time has a certain resulting phase, cancels out the field at a later time, when the phase is different, which is what the expectation value provides. We are more interested in the expectation value of the *size* of the amplitude, or the intensity even, i.e. we are interested in the quantity $\langle I \rangle = \langle |E|^2 \rangle$. To derive this, we assume that we have radiation from N atoms with random phases and its sum is a total field $|E|^2 = |\sum_{i=1}^{N} \cos\phi_i|^2$ at every point in time. For each time bin, t, we look at, the size of this total field might be different, but we can calculate the expectation value of this field after watching it for a long time, T, as

$$\langle |E|^2 \rangle = \frac{1}{T}\sum_{t=1}^{T} |E_t|^2 = \frac{1}{T}\sum_{t=1}^{T}\left|\sum_{i=1}^{N} \cos\phi_{i,t}\right|^2. \tag{8.5}$$

If we square the inner sum we get

$$\frac{1}{T}\sum_{t=1}^{T}\left|\sum_{i=1}^{N}\cos\phi_{i,t}\right|^2 = \frac{1}{T}\sum_{t=1}^{T}\left(\sum_{i=1}^{N}\cos^2\phi_{i,t} + \sum_{p<q}^{N}\cos\phi_{p,t}\cos\phi_{q,t}\right), \tag{8.6}$$

where the cross terms, $\sum_{p<q}^{N}\cos\phi_{p,t}\cos\phi_{q,t}$, are all zero for uncorrelated angles[1]. What is left is thus

$$\frac{1}{T}\sum_{t=1}^{T}\sum_{i=1}^{N}\cos^2\phi_{i,t} = \sum_{i=1}^{N}\frac{1}{T}\sum_{t=1}^{T}\cos^2\phi_{i,t}, \tag{8.7}$$

where the summation order has been switched, which is valid since they are independent variables. The inner sum can be calculated as

$$\sum_{t=1}^{T}\cos^2\phi_{i,t} = \sum_{t=1}^{T}\frac{1+\cos 2\phi_{i,t}}{2} = \frac{1}{2}T, \tag{8.8}$$

again the terms $\cos 2\phi_{i,t}$ sum up to zero, since they contain equally many positive and negative values. Inserting the value of the inner sum into Equation (8.7) finally yields

$$\left\langle |E|^2 \right\rangle = \sum_{i=1}^{N}\frac{1}{T}\left(\frac{T}{2}\right) = \frac{N}{2}. \tag{8.9}$$

So, in words, the expectation value for the intensity of N uncorrelated radiating atoms, scales directly with N. But if the atoms are not uncorrelated, but instead are coherent, what can we expect then? Well, for perfectly coherent atoms the absolute value of the total field, $\left|\sum_i^N \cos\phi_i\right|$ just corresponds to the sum of maximally aligned cosine terms, i.e. $\sum_i^N 1 = N$. If we again consider the expectation value for the intensity we get $\left\langle E^2_{coherent}\right\rangle = N^2$, which means light emitted from coherent atoms scales quadratically stronger than that from incoherent atoms.

As an example, in our systems, we often look at an ensemble of atoms in a peak, which typically consists of $\sim 10^{10}$ atoms. The difference in radiation intensity, depending on whether the sample is coherent or incoherent, is thus $N^2/N = N = 10^{10}$. So whenever these dipoles are in phase they are radiating ten orders of magnitude more strongly than otherwise, which is a huge effect. This is the basis of some phenomena which will be discussed in this chapter, such as free induction decay and superradiance. It should be noted that the total radiative energy from the atoms is of course

[1] Because the cross term sum can be written $\sum_{p<q}^{N}\left(\cos(\phi_{p,t}+\phi_{q,t})+\cos(\phi_{p,t}-\phi_{q,t})\right)/2$, and we see that it is a sum of simple cosine terms, which for uncorrelated variables have just as many positive values as negative, thus giving on average zero.

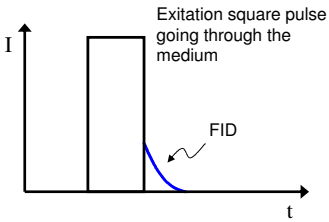

Figure 8.1. *A square-shaped excitation pulse as it is detected after the medium. The FID tail comes from atoms that are radiating coherently for a short time.*

the same for both the coherent and incoherent case. As the intensity of the light becomes stronger with increasing collective effect, the total duration before all atoms have been deexcited becomes correspondingly shorter, thus conserving the energy.

8.3 Free induction decay (FID)

In our systems, if we send in a light pulse to put the atoms in a peak into a superposition state, then there is a moment just after the excitation, at which they will all be in phase, and at this point they will for a brief time emit coherently, giving rise to a strong emission immediately after a pulse, as depicted in Figure 8.1. This tail of strong emission following the pulse is called *free induction decay*, or FID. The total duration of the FID is given by how long the atoms stay in phase. For a peak in our system, the typical inhomogeneous frequency width is 170 kHz, which gives an effective ensemble dephasing time of $T_2^* \approx 2$ µs, causing the observed intensity to decay with a time constant of 1 µs.

8.4 Superradiance

The discussion so far has illustrated very nicely how an increased radiation can occur. The advantage of regarding this increase simply as oscillators in phase, is that it has a very clear classical analogy. A set of purely classical antennas can be used to obtain exactly the same equations and results as in Section 8.2. It is, however, not the only effect in a quantum mechanical system that can cause increased radiation. In this section two terms will be discussed, superradiance and superfluorescence. There is a difference between the two that will be discussed later in the section, but initially, as well as in many other places in the thesis, I will just use the term superradiance to describe both effects. Let us start off by introducing the second mechanism increasing the radiation by considering a simple two-atom case.

8.4.1 Simple case

Superradiance was first predicted by R. H. Dicke in a paper in 1954 [74], in which he starts by giving a very simple argument as to why the picture of atoms emitting radiation independently of each other, is wrong. The argument goes something like this: imagine that we have a single two-level atom, with states $|g\rangle$ and $|e\rangle$, and that it is originally in the excited state. In general, the transition rate is proportional to the overlap of the initial and the final state, coupled by a Hamiltonian, which in the case of radiation is the dipole operator

$$W \sim |\langle g| \mathbf{d} |e\rangle|^2 . \tag{8.10}$$

We now consider a system in which two such atoms exist close to each other, for simplicity, spatially separated by less than one wavelength. If we are watching only the emitted radiation from the system, then the atoms are indistinguishable, and we need to treat the two atoms as one quantum mechanical system, and not as two separate systems. Two-level atoms such as these, are very similar to spin 1/2-systems, so we can use the theory for such systems, describing it by four basis states that are shown in Figure 8.2. These states are the three symmetric triplet states, $|gg\rangle$, $|ee\rangle$ and $(|eg\rangle+|ge\rangle)/\sqrt{2}$, as well as the antisymmetric singlet state $(|eg\rangle-|ge\rangle)/\sqrt{2}$. If we can state with certainty that only one photon has been absorbed, we are limited to either $(|eg\rangle+|ge\rangle)/\sqrt{2}$ or $(|eg\rangle-|ge\rangle)/\sqrt{2}$.

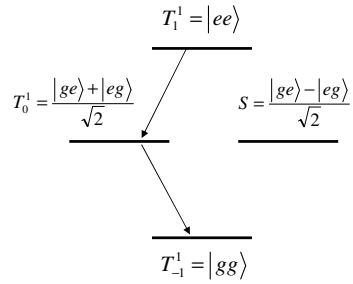

Figure 8.2. *Level diagram of a system of two two-level atoms. the arrows indicate the relaxation path, and the state labels are analogous to the spin-1/2 formalism.*

The radiation rate, due to the emission from either of these two cases, is different from what it would be if the two atoms were independent, in which case it would still remain W. To analyze the two-atom system we examine the decay rate, which is given by the two-atom dipole operator, i.e. $\mathbf{d_{12}} = d_1 I_2 + I_1 d_2$. Considering first the triplet case, we calculate the decay rate according to Equation (8.10)

$$\begin{aligned} W_{triplet} &\sim \left| \langle gg| \mathbf{d} \left(\frac{|eg\rangle + |ge\rangle}{\sqrt{2}} \right) \right|^2 = \frac{1}{2} \left| \langle gg| \mathbf{d} |eg\rangle + \langle gg| \mathbf{d} |ge\rangle \right|^2 \\ &\sim \frac{1}{2} \left| \sqrt{W} + \sqrt{W} \right|^2 = 2W. \end{aligned} \tag{8.11}$$

As can be seen, the decay rate from this triplet system is twice that of two independent atoms. Similarly, if the atoms were in the singlet state, the transition rate would be

$$W_{singlet} \sim \frac{1}{2} \left| \langle gg| \mathbf{d} |eg\rangle - \langle gg| \mathbf{d} |ge\rangle \right|^2 \sim \frac{1}{2} \left| \sqrt{W} - \sqrt{W} \right|^2 = 0, \tag{8.12}$$

i.e. atoms in the singlet state do not decay. This can also be seen using symmetry arguments, because the antisymmetric singlet state cannot decay to the symmetric ground state, because the dipole operator cannot change the symmetry properties. In the triplet case we have the superradiant state, and in the singlet case we say that the system is subradiant, i.e. the decay is completely inhibited.

8.4.2 Superradiance vs. Superfluorescence

It is very interesting to consider the increased radiation from the triplet state in Equation (8.11), in comparison to the radiation that would be given by two atoms, both in the 50/50 superposition state $|+\rangle = (|g\rangle + |e\rangle)/\sqrt{2}$. Two atoms in the $|+\rangle$ state would be equivalent to the classical case of oscillators radiating completely

in phase, as was discussed in Section 8.2. The two atoms would then have the total state

$$|++\rangle = \frac{|g\rangle + |e\rangle}{\sqrt{2}} \frac{|g\rangle + |e\rangle}{\sqrt{2}} = \frac{1}{2}\left(|gg\rangle + |eg\rangle + |ge\rangle + |ee\rangle\right). \quad (8.13)$$

On average, the total excitation of this state is one photon, just as for the triplet state, but note that the photon number here is not known exactly, and could just as well be zero as one or even two units of excitation. Nevertheless, we can look at the decay rate for this state, similarly to what was done above

$$\begin{aligned} W_{+,1} &= |\langle gg|\,\mathbf{d}\,|++\rangle|^2 = \frac{1}{4}\left|\langle gg|\,\mathbf{d}\,(|gg\rangle + |eg\rangle + |ge\rangle + |ee\rangle)\right|^2 \\ &= \frac{1}{4}\left|0 + \sqrt{W} + \sqrt{W} + 0\right|^2 = W. \end{aligned} \quad (8.14)$$

Note here especially that the term $|ee\rangle$ seems to give no contribution to the decay because

$$\langle gg|\,\mathbf{d}\,|ee\rangle = \langle gg|\,d_1 I_2\,|ee\rangle + \langle gg|\,I_1 d_2\,|ee\rangle = \langle gg|ge\rangle + \langle gg|eg\rangle = 0, \quad (8.15)$$

due to orthogonality. This is not the whole story of course, as the $|ee\rangle$ state can also decay to the triplet state

$$W_{+,2} = \left|\frac{\langle ge| + \langle eg|}{\sqrt{2}}\mathbf{d}\,|++\rangle\right|^2 = \frac{W}{2}. \quad (8.16)$$

The total decay from the $|++\rangle$ state is thus

$$W_+ = \frac{3W}{2}. \quad (8.17)$$

This is an interesting result since it is higher than for independent atoms, but lower than for the triplet state.

In exactly the same way we can also compare the totally subradiant state, $(|ge\rangle - |eg\rangle)/\sqrt{2}$, with the product state of two atoms both in a 50/50 superposition but 180° out of phase. The latter case would again correspond to the intuitive classical model of oscillators out of phase. The out-of-phase product state can be written

$$|+-\rangle = \frac{|g\rangle + |e\rangle}{\sqrt{2}} \frac{|g\rangle - |e\rangle}{\sqrt{2}} = \frac{1}{2}\left(|gg\rangle + |eg\rangle - |ge\rangle - |ee\rangle\right). \quad (8.18)$$

In the same way as for the $|++\rangle$ state, we calculate the total decay rate to be

$$W_- = \frac{W}{2}, \quad (8.19)$$

which is lower than for independent atoms but still not completely zero as for the singlet state. There are also some other differences

between these product states and the triplet and singlet Dicke states, apart from the decay rate. For example, the Dicke states are entangled, and, as explained in Section 2.4, it is not possible to write entangled states in the form of a product between two individual states. As mentioned above, the decay rate of the product states could be conveniently explained in terms of classical oscillators being in or out of phase, but there is no classical analog for entangled states, so the intuitive interpretation of the Dicke states is actually a more difficult question.

If we increase the number of atoms that are contributing to the collective effect (but still keep the system spatially small), the differences in decay rate become smaller. In the treatment presented in Ref. [54], it is found that for a system of N atoms, the decay from the symmetric Dicke state is proportional to

$$W_{Dicke} \sim \frac{N(N+2)}{4}, \tag{8.20}$$

while for the symmetric product state, the decay is given by

$$W_{Product} \sim \frac{N(N+1)}{4}. \tag{8.21}$$

The formulas can be easily verified to agree with the simple cases of $N = 2$ that we have discussed here, and we can indeed note that for very large N the difference in decay rate is completely negligible. In fact, for large N both decay rates become proportional to N^2, just as we would expect from the discussion in Section 8.2. A similar treatment of the subradiant states results in the same conclusion, that for large N, the decay rate, even for the antisymmetric product state, approaches zero. From an experimental point of view this is a relief, because Dicke states of large N are in most cases difficult to create. The reason is that the Dicke states are based on knowing the exact number of absorbed photons, whereas for the product states only the average probability of excitation must be known, which is easily obtained from the light intensity and the atomic oscillator strength.

We can also note that when the atoms are in a superposition such as for the product states, there is an induced dipole moment, as explained in the first section of this chapter. The Dicke states however, do not have such a dipole moment. The distinction between the two types of states based on dipole moment was made in 1975 by Bonifacio [75], whereby he denoted the decay from the zero dipole moment, Dicke states as *superfluorescence* and the decay from product states with a dipole moment as *superradiance*. Many authors do not distinguish these cases however, and denote everything with an enhanced decay rate superradiance, as Dicke himself did. But from the viewpoint of intuitive understanding it is still important to remember that there are two types of mechanisms at work here.

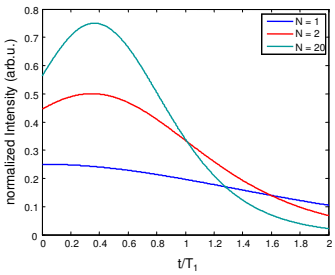

Figure 8.3. *The intensity of a superradiant system of atoms as a function of time and number of atoms. Note that it has been normalized as intensity* per atom *for easier comparison.*

8.4.3 Extended media

For larger systems we can generalize the states described in the simple, two-atom system above. Extending the spin analogy we made for the Dicke states to a system of N atoms, we can call $J = N/2$, the total "momentum" and M would be the corresponding projection of that momentum, which in this case signifies the degree of excitation. $M = J = N/2$ means all atoms are in the excited state and $M = -J = -N/2$ means all are in the ground state. The state of a general system of M excited atoms can then be written (see e.g. [76])

$$|J, M\rangle = \mathbf{S}\Big(|\underbrace{g, g, \ldots, g}_{J+M}, \underbrace{e, e, \ldots, e}_{J-M}\rangle\Big), \tag{8.22}$$

where $\mathbf{S}$ is some "symmetrization operator" if we are talking about the symmetric superradiant case. A similar "anti-symmetrization operator" $\mathbf{A}$ could be used for a subradiant discussion. With this notation the maximum transition rate occurs when half of the atoms are excited, i.e. $M = 0$, and is given by Equation (8.20). Regarding the evolution of a system with such a decay rate, the emitted intensity as a function of time can be calculated as [76]

$$I(t) = \frac{I_0 N^2}{4} \operatorname{sech}\left(\frac{t - \tau_d}{2\tau_w}\right)^2. \tag{8.23}$$

The sech shape of this function shows that the spontaneous decay from a correlated collective system of atoms will have a distinct peak rather than simply following a decreasing exponential as independent atoms would. In Equation (8.23), $\tau_w = T_1/N$ is the temporal width of this peak and $\tau_d = T_1 \ln(N)/N$ is the delay time before the peak. This delay originates from the fact that the coherent process is started by a normal, spontaneous decay, just as for the inverted medium of a laser. This function is plotted for some different N in Figure 8.3.

The key to maintaining super- and subradiance in large media, is to make sure that the atoms are still indistinguishable. For the simple cases we have discussed so far, when the atom separation is much smaller than the wavelength, this is taken care of automatically, since any exciting photons cannot tell the atoms apart, but for a medium that is large compared to the wavelength there are additional requirements. For a medium which is extended along one dimension, e.g. $L_z >> \lambda$, superradiance can only be observed along this exact direction up to the solid divergence angle of the light Ω_D. To account for this we add a compensation factor of $\mu = \Omega_D/4\pi$. For an extended system the width of the superradiance pulse instead becomes [77]

$$\tau_w = \frac{T_1}{N\mu}, \tag{8.24}$$

and the delay before the pulse becomes

$$\tau_d = \frac{T_1 \ln^2 \sqrt{2\pi N}}{4N\mu}. \tag{8.25}$$

That the delay time is affected by the divergence angle can also be understood intuitively, based on the idea that the process is started from a spontaneous decay. Any single atom can decay in any direction, but only when it decays into the direction of the other atoms in the extended system, will it give rise to any correlated effects. The probability that a decay happens in this specific direction is $\Omega_D/4\pi$, and so the delay becomes correspondingly longer. Furthermore, for extended systems, one often sees multiple outgoing superradiance pulses, not just a single one. This can be explained in most cases by pulse propagation effects [78]. Another effect appears if the ensemble of atoms is long enough, such that the length, L_z, is longer than $\sim c\tau_d$. The atoms from different parts of the sample can then independently decay into the superradiant direction, creating several independent superradiance peaks [79, 80].

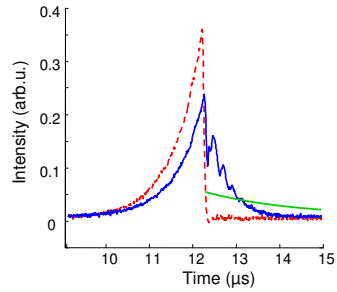

Figure 8.4. *Red dashed curve shows the input pulse (on a detector before the sample), the blue solid line shows the same pulse after passing though the crystal, where the immediate superradiant decay is clearly visible. The green line represents the $1/T_2^*$ decay as it would have been in the FID regime.*

8.5 Rare-earth crystal implementation

Spontaneous emission can occur in any direction and at any time (given by the decay curve), which makes it very undesirable as the recall process in quantum memories. The collective emission effect is therefore a necessary mechanism for realizing quantum memories, as the discussion regarding the fidelity preservation in the CRIB protocol in Section 6.3.2 is a very good example of. However, there are different regimes of the collective effects as well. A collective enhancement can be obtained even for very few atoms, and in an inhomogeneously broadened structure, such as the population peaks in our schemes, the decay immediately following an excitation is usually close to the free induction decay (FID). The FID occurs on a timescale inversely proportional to the spectral width of the peak, since after this time, the ions are no longer in phase, as mentioned in Section 8.3. As long as the number of photons emitted during the FID is small compared to the total number of excited ions, we are still in the FID regime. However, once the number of emitted photons becomes comparable to the number of excited ions, we move into what can be called the superradiant regime, where the duration of the decay becomes inversely proportional to αL. This effect is illustrated in Figure 8.4.

This behavior was studied in detail in Paper **VI**, and it was found that the superradiant decay time can be described by

$$T_{dec} = \frac{T_2^*}{2 + \frac{\alpha L}{2} x}, \tag{8.26}$$

where x is a numerical parameter that depends on the shape of the excitation pulse and weakly on αL. It can be shown that the most

efficient pulse shape, when it comes to creating the excitation, is a time-reversed replica of the exponential decay curve [81, 82]. This fact can be understood intuitively by noting that, at the start of the pulse, the corresponding Fourier width is very large, and when the Fourier width is larger than the ensemble peak width, a large part of the pulse will go through the sample without interacting with the ions. Therefore, the pulse should start with very little energy, and increase its energy at the same rate as it takes for the Fourier width to approach the peak width, which is $1/T_2^*$. For such input pulses, the parameter, x, can be approximated by $x \approx 0.99 + 0.1\alpha L - 0.0037(\alpha L)^2\big|_{\alpha L \approx 4} \approx 1.3$.

In addition to shorter duration, the decay is also stronger for higher αL, as would be expected. If we define the efficiency, η_{SR}, as the total energy found in the superradiant decay part divided by the total energy of the incoming pulse, then the efficiency can be approximated as

$$\eta_{SR} \approx \frac{2}{T}\frac{T_2^*}{2+\frac{\alpha L}{2}x}\left(1-e^{-\frac{\alpha L}{2T_2^*(1/T+1/T_2^*)}}\right)^2, \tag{8.27}$$

where T is the pulse duration. The above expression is valid in the regime of $\alpha L \lesssim 10$. This effect was also verified in Paper **VI**, and it was found that the superradiant decay, immediately following the excitation, could pose problems in future implementations of quantum memories in high αL structures. This is however, still not fully investigated, and in similarity with many other topics discussed in this thesis, there is certainly not a lack of interesting work for the future.

Comments on the Papers

I **Understanding laser stabilization using spectral hole burning**

In this paper, theory for laser stabilization, when locking to spectral holes, was derived. Optimum parameter regimes were found, and a laser was constructed and verified to comply with the theoretical results.

I contributed to investigations on the parameters and I helped to construct the system, specifically the digital components.

II **Experimental quantum state tomography of a solid state qubit**

Arbitrary single qubit rotations, on a qubit based on the long-lived hyperfine states, was demonstrated and verified by performing a quantum state tomography sequence. Fidelities above 90% for single gate operations were achieved.

I took part in planning the experiment and wrote the pulse sequences. I also carried out the experimental work together with Lars Rippe, I analyzed the data and finalized the manuscript.

III **Spectral hole-burning spectroscopy in Nd^{3+}:YVO_4**

A neodymium doped yttrium vanadate material was characterized, using hole-burning techniques. Magnetic fields were applied to split the Zeeman levels and preliminary spectral tailoring showed that these levels have potential in terms of quantum memories.

I participated in some of the planning and helped during the experiments.

IV **Hyperfine structure and hyperfine coherent properties of Praseodymium in single-crystalline $La_2(WO_4)_3$ by hole-burning and photon-echo techniques**

This paper is a spectroscopic characterization of a crystal using a new Pr^{3+} host material, $La_2(WO_4)_3$. In similarity with other Pr^{3+} materials it is shown to be well suitable as a quantum information Λ-system, despite having a high magnetic moment density. All relevant transition levels and linewidths are mapped out.

I participated in the planning and during the experimental work.

V **Long coherence lifetime and electromagnetically induced transparency in a highly spin concentrated solid**

Using the $La_2(WO_4)_3$ host material, we demonstrated electromagnetically induced transparency. We also measured a hyperfine coherence time of 250 µs, which is very long for a material with such high magnetic moment density, and the implications of this is that a wide range of materials could be suitable for similar quantum information processes.

I took part in the preparations and during the experiments.

VI **Experimental superradiance and slow light effects for quantum memories**

In this paper, superradiant effects that can occur in the high optical depth regime of quantum memories, was investigated. It was verified that for sufficiently high αL, the duration of the collectively emitted light decreases as a function of αL, at the same time as the total energy of the emitted light is increased. In addition, it was found that strong slow light effects are present, simply from the dispersion created by an empty spectral region.

I took part in preparing the experiments as well as carry them out. I also took part in analyzing the results and I wrote most of the manuscript.

Acknowledgements

I would first and foremost like to thank my supervisor, Stefan Kröll, for his open-mindedness and for always having time for discussions, and for creating a good atmosphere in the group.

I would also like to thank my co-supervisor Anders Persson for finding the time to put his great technical knowledge to use for our benefit.

I am very grateful to Lars Rippe, for having very interesting ideas about everything from physics to politics, and for always having the time to help out or simply talk. I am also grateful to Brian Julsgaard for inspiration to better combine theory with experiment.

I would like to thank the current research group members, especially Yan Ying and my roommate Atia Amari, for a good team effort, in particular this last hectic year, but also the newer members Mahmood Sabooni and Huang Maomao, as well as the older members, including my former roommate Mattias Nilsson for a good introduction to the work.

For more specific things, I acknowledge Leif in Cryolab for an excellently provided liquid helium service, Henrik Steen and Minna Ramkull for administrative help, and Björn Lundberg and Bertil Hermansson for help with electronics and the like. I also acknowledge Alexey Kalachev for helpful discussions regarding superradiance and Mikael Afzelius for the same on quantum memories.

My appreciation in general goes to the multitude of people that make up the great division of atomic physics, for help with everything from LaTeX issues to Matlab programming, and for maintaining a very friendly atmosphere, and in particular to Sune Svanberg for providing the possibilities for the good environment and for giving everyone the motivation to keep the working experiment running.

I send my thanks also to all my online friends for making sure I'm not working too late in the evening, and to all my RL friends for making sure I'm not playing too much either.

And finally, I would like to thank my family for their patience and support during all the years.

References

1. R. P. Feynman. *Simulating Physics with Computers.* International Journal Of Theoretical Physics **21**, 467–488 (1982).

2. P. W. Shor. *Algorithms for quantum computation: discrete logarithms and factoting.* Proceedings of the IEEE 35 th Annual Symposium on Foundations of Computer Science pages 124–134 (1994).

3. L. K. Grover. *A fast quantum mechanical algorithm for database search.* Proceedings of the Twenty-Eighth Annual ACM Symposium on Theory of Computing pages 211–219 (1996).

4. Pierre Meystre and Murray Sargent. *Elements of Quantum Optics.* Springer-Verlag (1989).

5. M. A. Nielsen and I. L. Chuang. *Quantum computation and quantum information.* Cambridge university press (2000).

6. D. Allen and J. H. Eberly. *Optical resonace and two-level atoms.* Wiley New York (1975).

7. P. W. Milonni and J. H. Eberly. *Lasers.* John Wiley & Sons New York (1988).

8. A. Einstein, B. Podolsky and N. Rosen. *Can quantum-mechanical description of physical reality be considered complete?* Phys. Rev. **47**, 0777–0780 (1935).

9. M. S. Silver, R. I. Joseph, C.N. Chen, V. J. Sank and D. I. Hoult. *Selective-population inversion in NMR.* Nature **310**, 681–683 (1984).

10. M. S. Silver, R. I. Joseph and D. I. Hoult. *Selective spin inversion in nuclear-magnetic resonance and coherent optics through an exact solution of the Bloch Riccati equation.* Phys. Rev. A **31**, R2753–R2755 (1985).

11. I. Roos and K. Mølmer. *Quantum computing with an inhomogeneously broadened ensemble of ions: Suppression of errors from detuning variations by specially adapted pulses and coherent population trapping.* Phys. Rev. A **69**, 022321 (2004).

12. T. Chang, M. Z. Tian, R. K. Mohan, C. Renner, K. D. Merkel and W. R. Babbitt. *Recovery of spectral features readout with frequency-chirped laser fields.* Opt. Lett. **30**, 1129–1131 (2005).

13. R. M. Macfarlane and R. M. Shelby. *Coherent transient and holeburning spectroscopy of rare earth ions in solids.* In A.A. Kaplyanskii and R.M. Macfarlane, editors, *Modern problems in condensed matter sciences.* North-Holland Amsterdam (1987).

14. G. H. Dieke and H. M. Crosswhite. *The spectra of the doubly and triply ionized rare earths.* Appl.Opt. **2**, 675–686 (1963).

15. W. M. Yen, Selzer P. M., G. F. Imbush, Kopelman R., Holstein T., Lyo S. K., R. Orbach, Kuber D. L., Weber M. J. and Francis A. H. *Laser spectroscopy of solids.* Springer-Verlag Berlin (1981).

16. F. R. Graf. *Investigation of spectral dynamics in rare earth ion doped crystals using high resolution laser techniques.* PhD thesis (1998).

17. R. W. Equall, R. L. Cone and R. M. Macfarlane. *Homogeneous broadening and hyperfine structure of optical transitions in Pr/sup 3+/:Y/sub 2/SiO/sub 5/.* Phys. Rev. B **52**, 3963–3969 (1995). URL http://axiom.iop.org/P/GUEST287/fmtprt?VdkVgwKey=5055823&fmt=H&emailed=1.

18. Y. Sun, C. W. Thiel, R. L. Cone, R. W. Equall and R. L. Hutcheson. *Recent progress in developing new rare earth materials for hole burning and coherent transient applications.* J.Lumin. **98**, 281–287 (2002).

19. E. Fraval, M. J. Sellars and J. J. Longdell. *Method of extending hyperfine coherence times in* $Pr^{3+} : Y_2SiO_5$. Phys. Rev. Lett. **92**, 077601 (2004).

20. E. Fraval, M. J. Sellars and J. J. Longdell. *Dynamic decoherence control of a solid-state nuclear-quadrupole qubit.* Phys. Rev. Lett. **95**, 030506 (2005).

21. Mattias Nilsson. *Coherent interactions in rare-earth-ion-doped crystals for applications in quantum information science.* PhD thesis Division of Atomic Physics, LTH (2004).

22. L. Rippe. *Quantum Computing with Naturally Tapped Sub-Nanometre-Spaced Ions.* PhD thesis Division of Atomic Physics, LTH (2006).

23. M. Zhu and J. L. Hall. *Stabilization of optical-phase frequency of a laser system - application to a commercial dye-laser with an external stabilizer.* J. Opt. Soc. Am. B **10**, 802–816 (1993).

24. B. C. Young, F. C. Cruz, W. M. Itano and J. C. Bergquist. *Visible lasers with subhertz linewidths.* Phys. Rev. Lett. **82**, 3799–3802 (1999).

25. K. J. Åström and R. J. Murray. *Feedback Systems: An Introduction for Scientists and Engineers* (). URL http://www.cds.caltech.edu/~murray/amwiki/.

26. E. D. Black. *An introduction to Pound-Drever-Hall laser frequency stabilization.* Am. J. Phys. **69**, 79–87 (2001).

27. wikipedia. Pulse-width modulation (2008). URL http://en.wikipedia.org/wiki/Pulse-width_modulation.

28. D. P. DiVincenzo. *The physical implementation of quantum computation.* Fortschr. Phys. **48**, 771 (2000).

29. M. O. Scully and M. S. Zubairy. *Quantum Optics.* Cambridge University Press (1997).

30. N. Timoney, V. Elman, S. Glaser, C. Weiss, M. Johanning, W. Neuhauser and C. Wunderlich. *Error-resistant single-qubit gates with trapped ions.* Phys. Rev. A **77**, 052334 (2008).

31. G. C. Björklund. *Frequency-modulation spectroscopynew method for measuring weak absorptions and dispersions.* Opt.Lett. **5**, 15–17 (1980).

32. Z. Guan, M. Lewander and S. Svanberg. *Quasi zero-background tunable diode laser absorption spectroscopy employing a balanced Michelson interferometer.* Opt. Ex. **16**, 21714 (2008).

33. M. A. Nielsen and I. L. Chuang. *Quantum computation and quantum information.* Cambridge University Press United Kingdom (2000). Eq. 8.148, Chapter 8.4.2.

34. L. Rippe, M. Nilsson, R. Klieber, D. Suter and S. Kröll. *Experimental demonstration of efficient and selective population transfer and qubit distillation in a rare-earth-metal-ion-doped crystal.* Phys. Rev. A **71**, 062328 (2005).

35. M. J. Sellars, E. Fraval and J. J. Longdell. *Investigation of static electric dipole-dipole coupling induced optical inhomogeneous broadening in Eu3+ : Y2SiO5.* J.Lumin. **107**, 150–154 (2004).

36. J. H. Wesenberg, K. Molmer, L. Rippe and S. Kroll. *Scalable designs for quantum computing with rare-earth-ion-doped crystals.* Physical Review A **75**, 012304 (2007).

37. R. M. Shelby and R. M. Macfarlane. *Frequency-dependent optical dephasing in the stoichiometric material EuP5O14.* Phys. Rev. Lett. **45**, 1098–1101 (1980).

38. L.-M. Duan and H. J. Kimble. *Efficienct engineering of multiatom entanglement through single-photon detections.* Phys. Rev. Lett. **90**, 253601 (2003).

39. E. Knill, R. Laflamme and W. H. Zurek. *Resilient quantum computation.* Science **279**, 342 (1998).

40. H.-J. Briegel, W. Dür, J. I. Cirac and P. Zoller. *Quantum Repeaters: The Role of Imperfect Local Operations in Quantum Communication.* Phys. Rev. Lett. **81**, 5932 (1998).

41. L. M. Duan, M. D. Lukin, J. I. Cirac and P. Zoller. *Long-distance quantum communication with atomic ensembles and linear optics.* Nature **414**, 413–418 (2001).

42. G. Brassard, N. Lütkenhaus, T. Mor and B. C. Sanders. *Limitations on practicle quantum cryptography.* Phys. Rev. Lett. **85**, 1330 (2000).

43. A. Muller, H. Zbinden and N. Gisin. *Underwater quantum coding.* Nature **378**, 449 (1995).

44. D. C. Burnham and D. L. Weinberg. *Observation of simultaneity in parametric production of optical photon pairs.* Phys. Rev. Lett. **25**, 84 (1970).

45. A. K. Ekert. *Quantum cryptography based on Bell's theorem.* Phys. Rev. Lett. **67**, 661 (1991).

46. C. H. Bennett, G. Brassard, S. Popescu, B. Schumacher, J. A. Smolin and W. K. Wootters. *Prufication of noisy entanglement and faithful teleportation via noisy channels.* Phys. Rev. Lett. **76**, 722 (1996).

47. D. Deutsch, A. Ekert, R. Jozsa, C. Macchiavello, S. Popescu and A. Sanpera. *Quantum Privacy Amplification and the Security of Quantum Cryptography over Noisy Channels.* Phys. Rev. Lett. **77**, 2818 (1996).

48. M. Fleischhauer and M. D. Lukin. *Quantum memory for photons: Dark-state polaritons.* Phys. Rev. A **65**, 022314– (2002).

49. S. A. Moiseev and S. Kröll. *Complete reconstruction of the quantum state of a single-photon wave packet absorbed by a Doppler-broadened transition.* Phys. Rev. Lett. **87**, 173601– (2001).

50. M. Nilsson and S. Kröll. *Solid state quantum memory using complete absorption and re-emission of photons by tailored and externally controlled inhomogeneous absorption profiles.* Opt. Comm. **247**, 393 (2005).

51. B. Kraus, W. Tittel, N. Gisin, M. Nilsson, S. Kröll and J. I. Cirac. *Quantum memory for nonstationary light fields based on controlled reversible inhomogeneous broadening.* Phys. Rev. A **73**, 020302(R) (2006).

52. M. Afzelius, C. Simon, H. Riedmatten and N. Gisin. *Multi-mode quantum memory based on atomic frequency combs.* arXiv:0805.4164v2 [quant-ph] (2008).

53. H. Riedmatten, M. Afzelius, M. U. Staudt, C. Simon and N. Gisin. *A solid-state light-matter interface at the single-photon level.* Nature **456**, 773 (2008).

54. L. Mandel and E. Wolf. *Optical Coherence and Quantum Optics.* Cambridge University Press New York (1995).

55. H. Lin, T. Wang, T. W. Mossberg and OPTICS LETTERS Alternate Journal: Opt. Lett. Label: PEM 0016. *Demonstration of 8-Gbit/in^2 areal storage density based on swept-carrier frequency-selective optical memory.* Opt. Lett. **20**, 1658–1660 (1995).

56. W. Tittel, M. Afzelius, R. L. Cone, T. Chanelire, S. Kröll, S. A. Moiseev and M. Sellars. *Photon-echo quantum memory.* arXiv:0810.0172v1 [quant-ph] (2008). URL http://arxiv.org/abs/0810.0172.

57. M. U. Staudt, M. Afzelius, H. de. Riedmatten, S. R. Hastings-Simon, C. Simon, R. Ricken, H. Suche, W. Sohler and N. Gisin. *Interference of Multimode Photon Echoes Generated in Spatially Separated Solid-State Atomic Ensembles.* Phys. Rev. Lett. **99**, 173602 (2007).

58. Peter W. Milonni. *Controlling the speed of light pulses.* J. Phys. B; Mol. Opt. Phys. **35**, R31–R56 (2002).

59. John S. Toll. *Causality and the Dispersion Relation: Logical Foundations.* Phys. Rev **104**, 1760 (1956).

60. Robert W. Boyd. *Nonlinear Optics.* Academic Press second edition (2003).

61. L. J. Wang, A. Kuzmich and A. Dogariu. *Gain-assisted superluminal light propagation.* Nature **406**, 277 (2000).

62. L. Brillouin and A. Sommerfeld. *Wave propagation and group velocity.* Academic press (1960).

63. mathworld.wolfram. Analytic continuation (2008). URL http://mathworld.wolfram.com/AnalyticContinuation.html.

64. G. Diener. *Superluminal group velocities and information transfer.* Phys. Lett. A **223**, 327 (1996).

65. H. Jeong, A. M. C. Dawes and D. J. Gauthier. *Direct observation of optical precursors in a region of anomalous dispersion.* Phys. Rev. Lett. **96**, 143901 (2006).

66. M. D. Lukin and A. Imamoglu. *Nonlinear optics and quantum entanglement of ultraslow single photons.* Phys. Rev. Lett. **84**, 1419–1422 (2000).

67. L. V. Hau, S. E. Harris, Z. Dutton and C. H. Behroozi. *Light speed reduction to 17 metres per second in an ultracold atomic gas.* Nature **397**, 594–598 (1999).

68. B. D. Clader and J. H. Eberly. *Theoretical study of fast light with short sech pulses in coherent gain media.* J. Opt. Soc. Am. B **24**, 916 (2007).

69. M. Fleischhauer, A. Imamoglu and J. P. Marangos. *Electromagnetically induced transparency: Optics in coherent media.* Reviews of Modern Physics **77**, 633 (2004).

70. P. L. Knight, M. A. Lauder and B. J. Dalton. *Laser-induced continuum structure.* Phys. Rep. **190**, 1 (1990).

71. S. H. Autler and C. H. Townes. *Stark effect in rapidly varying fields.* Phys. Rev. **100**, 703 (1955).

72. U. Fano. *Effects of configuration interaction on intensities and phase shifts.* Phys. Rev. **124**, 1866 (1961).

73. wikipedia. Law of Large Numbers (2008). URL http://en.wikipedia.org/wiki/Law_of_large_numbers.

74. R. H. Dicke. *Coherence in spontaneous radiation processes.* Phys. Rev. **93**, 99–110 (1954).

75. R. Bonifacio and L. A. Lugiato. *Cooperative radiation processes in two-level systems: Superfluorescence.* Phys. Rev. A **11**, 1507 (1975).

76. M. Gross and S. Haroche. *Superradiance: An essay on the theory of collective spontaneous emission.* Physical Reports **93**, 301–396 (1982).

77. J. C. MacGillivray and M. S. Feld. *Theory of superradiance in an extended, optically thick medium.* Phys. Rev. A **14**, 1169 (1976).

78. M. D. Crisp. *Propagation of small-area pulses of coherent light through a resonant medium.* Phys. Rev. A **1**, 1604 (1970).

79. F. T. Arrecchi and E. Courtens. *Cooperative phenomena in resonant electromagnetic propagation.* Phys. Rev. A **2**, 1730 (1970).

80. N. Skribanowitz, I. P. Herman, J. C. MacGillivray and M. S. Feld. *Observation of Dicke superradiance in optically pumped HF gas.* Phys. Rev. L. **30**, 309 (1973).

81. A. V. Gorshkov, A. Andre, M. Fleischhauer, A. S. Sørensen and M. D. Lukin. *Universal approach to optimal photon storage in atomic media.* Phys. Rev. Lett. **98**, 123601 (2007).

82. A. Kalachev. *Quantum storage on subradiant states in an extended atomic ensemble.* Phys. Rev. A **76**, 043812 (2007).